QUANTUM LIMITED DETECTION AND NOISE IN SUPERCONDUCTING TUNNEL JUNCTION MIXERS

A Dissertation
Presented to the Faculty of the Graduate School
of
Yale University
in Candidacy for the Degree of
Doctor of Philosophy

by
Dean Willett Face
May 1987

ABSTRACT

QUANTUM LIMITED DETECTION AND NOISE IN SUPERCONDUCTING TUNNEL JUNCTION MIXERS

Dean Willett Face
Yale University
1987

High quality Superconductor-Insulator-Superconductor (SIS) tunnel junctions with small subgap leakage currents and a "sharp" current rise at the sum-gap voltage have been produced for studying strong quantum mixing effects at 36 GHz. These junctions employ a Ta or Nb base electrode and a $Pb_{0.9}Bi_{0.1}$ counter electrode. The novel step-defined process used to fabricate these junctions yields junctions with small areas (1-6 μm^2), high critical current densities (10^2 - 10^4 A/cm^2), low subgap leakage currents (< 1%), and a "sharp" current rise of width $\Delta V \sim 30$ μV at the sum-gap voltage. These junction properties are required for the experimental observation of strong quantum mixing effects at 36 GHz which are discussed in this thesis.

The relatively new technique of ion beam sputter deposition is also described in this work. This technique was used for preparing high quality Nb and Ta refractory superconducting films on room temperature substrates. These films were used in the fabrication of SIS mixers discussed above. The transport and electrical properties of these films were characterized and found to approach those of the bulk material. In addition, it was

found that the crystallographic structure of Ta films could be easily controlled by the deposition of a thin Nb underlayer. Ta films deposited without a Nb underlayer grew in the well known β-phase (tetragonal) which was not superconducting, while Ta films deposited on a thin ($\geq$ 3Å) Nb underlayer grew in the desired bcc (superconducting) phase with a T_C of ~ 4.3K.

Accurate mixer measurements at 34.5 GHz with a 1.5 GHz intermediate frequency (IF) gave single sideband mixer gains up to G = 1.1 ± 0.1 and mixer noise temperatures as low as T_M = 3.8 ± 1.0K. This value of T_M is close to the quantum limit of $T_Q = \hbar\omega/k\ln 2 \simeq 2.5$K. The lowest receiver noise temperature measured at the 1.3K input to the mixer block, T_R = 24 ± 1K, is the lowest reported for any heterodyne receiver. The quantitative dependence of the gain and noise on subgap leakage current and I-V sharpness for different tunnel junctions was also characterized and compared with the three port quantum mixer theory. This comparison shows that the three port theory underestimates the experimental noise power by a factor of 1.5 to 2 for all of the junctions measured. For junctions with I-V curves that are <u>not</u> "sharp" compared to $\hbar\omega$/e, the experimentally measured gain is ~ 2 dB below the theoretical prediction. For junctions that are "sharp" compared to $\hbar\omega$/e, the theory predicts large or infinite available gain for a significant range of experimental parameters where large gain was not observed. These discrepancies are likely due to the failure of the three port approximation for junctions that show strong quantum effects.

ACKNOWLEDGEMENTS

It is a pleasure to acknowledge the many people who played an important part in making this thesis possible. I am grateful to my advisor, Dan Prober, for his enthusiasm and support during my years at Yale. His clear scientific insights are well matched by a genuine and well-appreciated concern for his students. I am also grateful to Professor Paul Richards, and Rob McGrath at UC Berkeley for their invaluable contributions to this work and for making my stays at Berkeley very enjoyable. Steve Ruggiero was also an inspirational collaborator in the initial phases of developing the ion-beam deposition system.

P. Santhanam will always have a special place in the Prober lab group. His insights and curiosity generated many an interesting discussion on topics from electron scattering to the philosophy of life. He has also been a close friend. Bruce Dalrymple instructed me in the fine art of optimal cryostat construction. His dry wit and keen sense of humor warmed even the coldest nights in Becton. Shalom Wind has often helped to clear up even the most clumsy expression of ideas. His tennis skills (which are pretty decent I must say) have also provided welcome relief from the frustrations of experimental physics. Michael Rooks has been a great help in quickly slicing through even the most cleverly concealed computer system bugs and quirks. His two week tussle with the new laser printer and all of its fonts allowed the printing of this thesis. Elie Track has been a great help with instrumentation and wrote the computer program to calculate BCS I-V curves. His direct and apparently simple questions often penetrate to the depths of our ignorance. V. Chandrasekhar and Tom Kopley have been welcome officemates during the late nights of thesis writing and junk food eating. I am deeply in debt to Clifford Sneider for making widgets and gadgets of all description based on uncertain and changing designs. I also

thank Philippe Male for expert electron microscopy and Sal Datillo for photographic work. Jayne Miller and Linda Schwartz frequently brought a sense of humor to life on the fourth floor and tolerated our absent-minded concern for liquid helium orders.

Outside of Yale, I have profited from numerous discussions with Mike Wengler, Antti Raisanen, Stan Raider, Jim Griener, and Alan Kleinsasser. I also thank John Rowell for his initial input in suggesting the investigation of tantalum tunnel junctions. I appreciate the help of Jim Harper in numerous discussions of ion source operation and for the loan of the small ion source used in this work. Andy Smith has also provided helpful advice as well as the initial versions of the mixer analysis programs. I am also indebted to Marc Feldman for many helpful discussions of the quantum mixer theory and for accepting my request to act as a thesis reader.

The financial support of Yale through a Becton Fellowship during my first year and a half at Yale is gratefully acknowledged. I would also like to thank Jim Harper and IBM Research for the loan of the small ion source used in this work. The financial support of the NSF through grants ECS-7927165 and ECS-83-05000 and the ONR through grant N00014-80-C-0855 has made this thesis work possible.

I would like to thank Professors V.E. Henrich, R.G. Wheeler, D.E. Prober, J.W. Serene, and P.L. Richards for serving on my thesis committee. I am grateful to J.W. Serene for finding the time in his busy schedule at the NSF to attend my thesis defense.

Finally, I would like to dedicate this thesis to my parents and my sister Sally whose love and support have been a constant source of strength and encouragement.

TABLE OF CONTENTS

LIST OF SYMBOLS AND ABBREVIATIONS

α	Electron Phonon coupling constant
α	Argument of the Bessel function $J_n(\alpha)$ - $\alpha = eV_\omega/\hbar\omega$
B	Bandwidth in Hertz
BCS	Bardeen-Cooper-Schrieffer
C_J	Junction capacitance
Δ	Superconducting energy gap
e	Electron charge (= 1.6022×10^{-19} Coulomb)
$F(\Omega)$	Phonon density of states
G	Same as G_A
G_A	Available conversion gain of a mixer (defined in chapter II)
G_C	Coupled conversion gain of a mixer (defined in chapter II)
$G_{m,m'}$	Real part of the Y matrix element $Y_{m,m'}$
G_S	Real part of Y_S
h	Planck's constant (= 6.6262×10^{-34})
$\hbar$	Planck's constant divided by 2π ($\hbar$ = 1.0546×10^{-34} J-s)
$H_{m,m'}$	H matrix element for calculating the mixer noise
IF	Intermediate Frequency
I-V	Current (I) vs. Voltage (V)
I_{KK}	Kramers Kronig transform of the DC I-V
I_{IF}	Magnitude of the current source at the IF output of the mixer
I_{LO}	Magnitude of the LO current source
I_{sig}	Magnitude of the current source at the signal frequency
J_n	n^{th} order Bessel function of the first kind
k	Boltzmann's constant (= 1.38×10^{-23} J/K)
K	Degrees Kelvin
LO	Local Oscillator
N(0)	Density of states at the Fermi level

$N_n(0)$	Density of states at the Fermi level for a normal metal
$N_S(E)$	Superconducting density of states as function of energy
η	Non-linearity parameter in mixer theory
ω	Frequency in radians per second
ω_D	Debye frequency
ω_{IF}	IF frequency
ω_{LO}	Local Oscillator frequency
ω_m	Frequency m of the mixer $\omega_m = \omega_o + m\omega_{LO}$ (m = 0, ±1, ±2, ...)
ω_o	Output frequency of the mixer (same as ω_{IF})
P_{IF}^A	Available IF output power of the mixer
P_{IF}^C	Coupled IF output power of the mixer
P_{IF}^N	Input noise power of the IF amplifier
P_{SIG}^A	Available input power at the signal frequency
P_M	Mixer noise power referred to the mixer input
P_R	Receiver noise power referred to the input of the mixer
$\|\rho\|^2$	Power reflection coefficient
R_D	Dynamic resistance of the tunnel junction at the bias voltage
R_N	Normal state tunnel junction resistance
RRR	Residual Resistance Ratio
SIN	Superconductor-Insulator-Normal metal
SIS	Superconductor-Insulator-Superconductor
θ_D	Debye temperature
T_C	Superconducting critical temperature or transition temperature
T_M	Mixer noise temperature (defined in chapter II)
T_Q	Quantum noise temperature limit = $\hbar\omega/k\ln 2$
T_R	Receiver noise temperature
T_{kq}	Tunneling matrix element
τ_s	Quasiparticle scattering time
τ_r	Quasiparticle recombination lifetime

V_{LO}	Amplitude of the local oscillator voltage
V_0	DC bias voltage on the tunnel junction
V_ω	Amplitude of the voltage at the frequency ω (usually the LO)
Y_{IF}	Output admittance of the mixer at the IF
Y_m	Admittance seen by the mixer at the frequency ω_m
Y_L	Load admittance seen by the mixer at the IF frequency (= Y_0)
$Y_{m,m'}$	Element of the Y matrix for mixer conversion
Y_S	Admittance of the signal source seen by the mixer
Z_i	Image impedance seen by the mixer
Z_{IF}	IF output impedance of the mixer
Z_L	Load impedance at the IF port of the mixer - the IF amplifier input Z
$Z_{m,m'}$	Matrix element of the augmented Z matrix (see chapter II)
Z_S	Signal impedance seen by the mixer

LIST OF FIGURES

LIST OF TABLES

I. INTRODUCTION

1.1 SIS Mixers and Quantum Limited Detection

A classical resistive mixer is a non-linear device that combines a local oscillator frequency (ω_{LO}) and a signal frequency (ω_S) to produce an intermediate frequency ($\omega_{IF} = \omega_S - \omega_{LO}$) as shown in Fig. 1-1. The conversion gain (G) of such a device is generally improved for sharper I-V characteristics, but is always limited to values of $G < 1$ in the classical mixer theory [Torrey and Whitmer, 1948]. An ideal Superconductor-Insulator-Superconductor (SIS) tunnel junction has an extremely non-linear current vs. voltage (I-V) characteristic due to the rapid onset of quasi-particle (single-electron) tunneling at the sum of the energy gaps of the two superconductors. This "sharp" non-linearity naturally suggests the application of SIS tunnel junctions as efficient resistive mixers. In recent years, the SIS quasiparticle mixer has, in fact, surpassed all other mixer technologies (such as Schottky and super-Schottky diode mixers) for use in low noise millimeter wave heterodyne receivers and is even comparable with maser amplifiers at some frequencies. It is now fair to say that most future advances in radio astronomy (in the 30 GHz to 500 GHz band) will likely be made with receivers based on SIS mixers. These advances would not have been possible without the combined efforts of advanced microfabrication, tunnel junction materials science, and good microwave design. It is hoped that this thesis conveys the excitement and interdisciplinary nature of this field.

If the non-linearity of the I-V characteristic is "sharp" on the voltage scale of $\hbar\omega/e$, an SIS mixer can show remarkable quantum effects such as conversion gain ($G > 1$) and a noise power approaching the quantum limit of one photon per hertz ($P_Q = \hbar\omega\Delta\nu$). $P_Q = \hbar\omega\Delta\nu$ corresponds to a noise temperature of $T_Q = \hbar\omega/k\ln 2 \simeq 2.5$K at 36 GHz. The SIS mixer is a very

Block Diagram of a Heterodyne Receiver

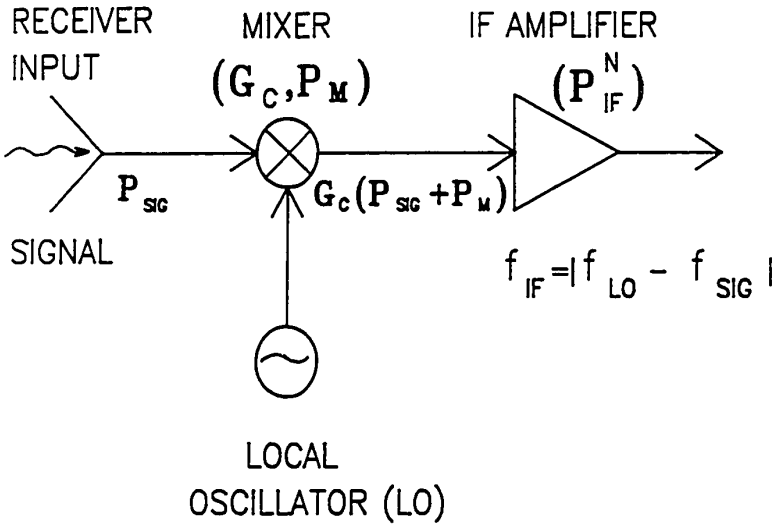

$$P_R = \frac{P_{IF}^N}{G_C} + P_M$$

Fig. 1-1 Block diagram of a heterodyne receiver. G_C is the coupled power gain of the mixer (coupled output power at the IF / available input power at the signal frequency). P_M is the noise power of the mixer referred to the input of the mixer. P_{IF}^N is the noise power of the IF amplifier referred to its input. P_R is the receiver noise power referred to the input of the mixer. The receiver noise power P_R is minimized by the use of large gain and low noise mixers.

interesting type of device in that it simultaneously displays important effects that are due to the "particle-like" character of the input radiation (photon assisted tunneling) as well as the "wavelike" character (mixing). These distinctly quantum mechanical effects are predicted by the quantum theory of mixing [Tucker, 1979] and have been experimentally observed by several groups [McGrath et al., 1981; Kerr et al. 1981; D'Addario, 1985]. For a recent review of progress in this field see Tucker and Feldman, 1985. These previous experiments, however, were limited by relatively poor junction quality in terms of I-V "sharpness" (except for McGrath et al., 1981) and a large noise measurement uncertainty that was comparable to the magnitude of the noise itself. These experimental limitations precluded accurate comparisons with the Tucker theory in the regime of strong quantum effects (large gain and low noise) especially where noise properties near the quantum limit were concerned. The exact dependence of mixer gain and noise on junction quality also had not been investigated. These issues thus provided the major motivation for this thesis work.

1.2 Materials and Fabrication

The fabrication of small area (~ 1 μm^2) high-current-density (~ 1000 A/cm^2) tunnel junctions with nearly ideal BCS I-V characteristics is essential to the study of strong quantum effects in SIS mixers. The small area is required to keep the junction capacitance small while the high current density is required to produce a junction this small with a resistance of ~ 50 Ω. Chapter III discusses some of the trade offs in the choice of materials and deposition technique in order to achieve nearly ideal I-V characteristics. In short, Ta was chosen as the most promising base electrode material because it forms a high quality oxide tunnel barrier, is thermally cyclable to 4.2K , and has a reasonable T_C (~ 4.4K). Alternative tunnel barriers are also discussed in chapters III, IV, and V. The new

technique of ion beam sputter deposition is described in chapter III along with its unique advantages. The ion beam sputter deposition technique turned out to be very useful in that it allowed us to control the nucleation of different crystallographic phases of Ta by simply depositing (or not depositing) a Nb underlayer before Ta deposition. Chapter IV describes a novel step-defined fabrication technique which eliminates photoresist processing between critical junction formation steps. Combined with a dc glow discharge oxidation process and gentle surface cleaning, the step-defined technique produced nearly ideal SIS tunnel junctions.

1.3 Microwave Mixer Measurements

With high quality junctions in hand (after considerable hard work) we have collaborated with W.R. McGrath and P.L. Richards at the University of California at Berkeley to make accurate measurements of mixer gain and noise. These measurements and the test apparatus are described in chapter VI. The novel test apparatus designed and constructed by the Berkeley group was essential to characterization of the mixing properties of high quality Ta and Nb junctions that were made at Yale. The careful experimental work required to fully understand and characterize the noise sources in the apparatus is an achievement in itself. This level of sophistication is essential, however, when trying to measure noise near the quantum limit at 36 GHz because even the thermal (blackbody) radiation noise from a 2.5K source will be comparable to the noise from a high quality SIS mixer. In fact, the test apparatus employs just such blackbody noise sources as calibrated noise standards for comparing with the mixer noise.

By measuring junctions with different subgap current levels, we were able to determine the relatively weak dependence of mixer noise on these currents. By measuring junctions with both broad and sharp current rises at the sum gap we were able to quantify the relative benefit of increasing

the sharpness of the current rise at the sum gap. One of the lowest leakage Ta junctions gave a mixer noise temperature of 3.8±1K which should be compared to the quantum limit of 2.5K at 36 GHz. These results are compared with the 3-port approximation of the quantum mixer theory in chapter VII.

A significant dependence of the mixer gain on the image impedance was also observed. (If the signal frequency is given by $\omega_S = \omega_{LO} + \omega_{IF}$ then the image frequency is given by $\omega_{IMAGE} = \omega_{LO} - \omega_{IF}$.) The impedance at the image frequency is theoretically expected to have a significant effect on the conversion gain of the mixer as discussed in chapter VII. We found that the narrow rf bandwidth of our mixer block provided significantly different signal and image impedances with a large IF of 1.5 GHz. This results in a relatively low gain (G = 1.1). A smaller IF of 25 MHz, however, gave approximately equal signal and image impedances and large gain G >> 1. The explanation of this effect was not obvious at first and required some careful analysis.

1.4 Comparison with the Quantum Mixer Theory

The experimental results of chapter VI have been compared with the three port (i.e., three frequency) approximation of the full Tucker theory as discussed in chapter VII. Higher order calculations are considerably more complex and require additional information on embedding impedances at higher frequencies which is difficult to obtain. For this reason, our calculations and almost all others in the literature are made in the three port approximation. This approximation should be valid for junctions with large enough capacitance that the harmonic frequencies are effectively shorted as discussed in chapter II. The results of these model calculations demonstrate that the three port theory overestimates the measured gain by ~ 2 dB in the low gain regime with rounded I-V curves. When the I-V

curve becomes sharp compared to $\hbar\omega/e$, however, we find that the theory predicts large and infinite available gains which were not measured. The detailed dependence of the gain and noise on the dc bias voltage, the LO voltage amplitude, signal impedance, and image impedance have all been investigated in the modeling. The purpose of this modeling is to characterize the range of experimental conditions over which large gain should have been observed. The theory also underestimates the measured noise power by a factor of 1.5 to 2 for both high gain and low gain mixers. The relative increase of mixer noise power with increased subgap current is, however, found to be in reasonable agreement with the theory.

"Experience does not ever err, it is only your judgement that errs in promising itself results which are not caused by your experiments."

- Leonardo Da Vinci (c. 1510)

II THEORETICAL OVERVIEW

This chapter provides the basic theoretical framework for understanding the results on superconducting materials, tunnel junctions, and quasiparticle mixers in the quantum limit that are presented in the following chapters. The chapter is divided into three major sections,

1.) Theory of superconducting materials
2.) Tunneling in superconductors
3.) Quantum mixer theory and quantum limited detection.

The section on superconducting materials reviews the basic properties of superconductivity in BCS (weak-coupled) and strong-coupled superconductors with an emphasis on the consequences for SIS tunnel junctions. We refer to superconductors with a large electron phonon coupling as being strong-coupled. The basic phenomenon of tunneling in superconductors is discussed with an emphasis on the quasiparticle tunneling effects which are most important for the operation of quasiparticle mixers. Josephson pair tunneling is not directly relevant for SIS mixers and is only briefly discussed. Finally, the quantum theory of mixing and its remarkable predictions for large gain ($G >> 1$) and low noise (approaching the Heisenberg uncertainty principle limit) are presented. A simplified picture of the gain mechanism which removes the complexity of the full theory is also presented. This simple picture illustrates why quantum mixers can achieve $G >> 1$ while classical mixers are restricted to $G < 1$.

2.1 Theory of Superconductivity and Superconducting Materials

2.1.1 BCS Theory

Excellent treatments of the BCS theory of superconductivity exist in a

number of books [Wolf, 1985; Tinkham, 1975; Rickayzen, 1969] as well as the original paper by Bardeen, Cooper and Schrieffer, (1957), so only the essential results will be presented. The basic physical idea behind the BCS theory is that the exchange of a virtual phonon by two electrons can cause an attractive electron-electron interaction. The BCS theory takes the attractive interaction V to be a constant up to a cut off frequency ω_c which is on the order of the Debye frequency ω_D. This attractive interaction is found to be largest for two electrons of equal and opposite momenta k, one with spin up and the other with spin down. If the attractive interaction is larger than the repulsive screened Coulomb interaction, a new ground state (the superconducting state) becomes energetically favorable. This ground state consists of pairs of electrons +k and -k with opposite spins called Cooper pairs. The elementary excitations from this ground state are called quasiparticles and are of primary importance for this thesis. The density states for these elementary excitations $N_S(E)$ in the BCS theory is given by,

$$N_s(E) = N_n(0)E/(E^2 - \Delta^2)^{1/2} \qquad |E| \geq \Delta \qquad 2\text{-}1$$

$$= 0 \qquad |E| < \Delta$$

where $N_n(0)$ is the density of states for the normal metal at the Fermi energy and E is the excitation energy for the quasiparticle which must be greater than the gap energy Δ. This is the density of states that is measured by an ideal SIS tunnel junction (see section 2.2) and is responsible for the extremely sharp current-voltage non-linearity required to observe strong quantum mixing effects (see section 2.3). It is conventional and convenient to think of these excitations (quasiholes or quasielectrons) in a semiconductor-like picture as shown in Fig. 2-1 for tunnel junctions. The BCS theory also predicts a zero temperature energy gap $\Delta(0)$ which is

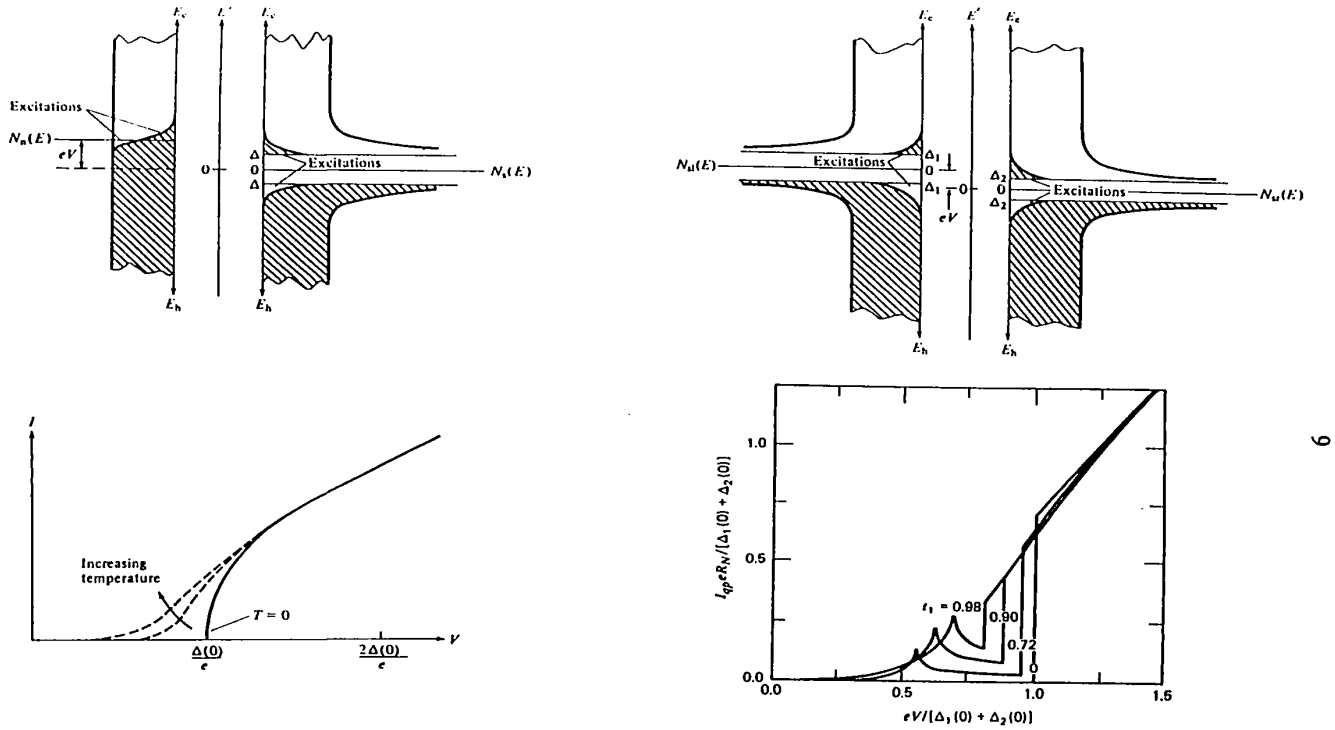

Fig. 2-1 a) Tunneling density of states for an SIN tunnel junction. b) I-V curve of an SIN tunnel junction for increasing temperature. c) Density of states diagram for an SIS′ tunnel junction showing the thermally excited quasiparticles. d) SIS′ tunnel junction I-V curve at several values of t = T/T_c. Note that the current rise at the sum gap is abrupt for all temperatures below T_c. (a,b,c are from Van Duzer and Turner, (1981); d) is from Harris, (1974).

given by,

$$\Delta(0) = \hbar\omega_c/\cosh[1/N(0)V] \qquad 2\text{-}2$$
$$\simeq 2\hbar\omega_c e^{-1/N(0)V} \qquad (N(0)V \ll 1)$$

and a finite temperature energy gap $\Delta(T)$ which is given by the implicit solution of,

$$\frac{1}{N(0)V} = \int_{-\hbar\omega_c}^{\hbar\omega_c} \frac{\tanh\,[(\epsilon^2 + \Delta^2(T))^{1/2} / 2kT]}{2[\epsilon^2 + \Delta^2(T)]^{1/2}}\, d\epsilon \qquad 2\text{-}3$$

The solution of this equation for Ta ($\Delta(0)$ = 0.69 meV) is plotted in Fig. 3-8 along with a useful approximate form $\Delta(T) \simeq 1.74\Delta(0)[1\text{-}T/T_c]^{1/2}$ which is valid near T_c. The superconducting transition temperature T_c is found when $\Delta(T)$ goes to zero and is related to the zero temperature gap $\Delta(0)$ by,

$$kT_c = 2\Delta(0)/3.53 \qquad 2\text{-}4$$

In the BCS theory, no attempt is made to calculate the value of V from material specific data such as the strength of the electron-phonon interaction (although it can be estimated). This type of calculation is left to the Eliashberg theory described in the next section. In this sense, the BCS theory does not predict the transition temperature of a superconductor, rather the actual T_c is used to infer V.

One of the more remarkable and important aspects of the superconducting state is its insensitivity to impurities and scattering. Although impurities can change the T_c and Δ of a superconductor (through $N_n(0)$ and V), the basic superconducting properties such as the existence of an energy

gap, the sharp peak in the density of states at Δ, and macroscopic phase coherence of the pair ground state (which leads to zero resistance and the Josephson effect) are unchanged. Naively one might expect that impurities, which destroy the ideal plane wave states used to construct the BCS ground state (with k+ and k- pairing), would modify the BCS predictions. Anderson, however, has shown [Anderson, 1959] that any external perturbation that does not break time reversal symmetry (such as a non-magnetic impurity) will leave the thermodynamic properties of the superconductor unchanged. This important theorem says that many disordered and even amorphous materials can be perfectly well behaved BCS superconductors provided they have pairs of time reversed states and a favorable electron-phonon interaction.

2.1.2 Eliashberg Theory for Strong-Coupled Superconductors

The strong-coupling theory of superconductivity as originally proposed by Eliashberg (1960) goes beyond the BCS theory and is fundamental to any theory that attempts to relate the gap to the basic interactions in the metal. The required mathematics is far more complex than that involved in the BCS theory and has been discussed in many excellent reviews [McMillan and Rowell, 1969; Scalapino, 1969; Wolf, 1985]. The essential physical difference between the BCS theory and the strong-coupling theory lies in the assumed nature of the phonon mediated electron-electron interaction. The electron-electron interaction provided by the final Eliashberg (1960) electron-phonon function,

$$V_{k,k+q} \propto \frac{E_{k+q} + \hbar\omega_q}{(E_{k+q} + \hbar\omega_q)^2 - E_k^2} \qquad 2\text{-}5$$

is local in space and retarded in time. This result is in contrast to the BCS model interaction which is nonlocal in space and instantaneous in time for any pair of electrons within $\hbar\omega_D$ of the Fermi surface. The origin of the retarded interaction is easy to understand. An electron moving through the lattice will deform the lattice and leave behind a polarization. A second electron moving through the same part of the lattice can then feel this polarization and scatter off of it. Clearly, the Eliashberg formulation more accurately describes the real nature of the electron-phonon interaction in metals. Details of the required calculations for the electron-phonon interaction can be found in several standard texts [Rickayzen, 1980; Fetter and Walecka, 1971].

At T=0K, the coupled Eliashberg equations for the energy dependent gap $\Delta(\omega)$ and renormalization function $Z(\omega)$ in an isotropic superconductor are [Wolf, 1985],

$$\Delta(\omega) = [Z(\omega)]^{-1} \int_0^{\omega_c} d\omega' P(\omega')[K_+(\omega,\omega') - \mu^*] \qquad 2\text{-}6$$

$$[1 - Z(\omega)]\omega = \int_0^{\infty} d\omega' N(\omega') K_-(\omega,\omega') \qquad 2\text{-}7$$

where

$$P(\omega) = \mathrm{Re}\left| \frac{\Delta(\omega)}{[\omega^2 - \Delta^2(\omega)]^{1/2}} \right| \qquad 2\text{-}9$$

$$N(\omega) = \mathrm{Re}\left| \frac{|\omega|}{[\omega^2 - \Delta^2(\omega)]^{1/2}} \right| \qquad 2\text{-}10$$

and

$$K_{\pm}(\omega,\omega') = \int_0^{\infty} d\Omega \alpha^2(\Omega)F(\Omega)\left|\frac{1}{\omega' + \omega + \Omega + i\delta} \pm \frac{1}{\omega' - \omega + \Omega - i\delta}\right| \qquad 2\text{-}11$$

In these equations, ω_c is a cutoff frequency typically taken as five times the maximum phonon frequency. $\Delta(\Delta_0)$ is the experimental energy gap measured in a tunnel junction and $N(\omega)$ is the tunneling density of states. The only material-dependent quantities here are μ^* and $\alpha^2(\Omega)F(\Omega)$. μ^* is the coulomb pseudopotential ($N(0)U_c$) which approximately characterizes the screened coulomb repulsion between electrons. $\alpha^2(\Omega)F(\Omega)$ for an isotropic superconductor is given by,

$$\alpha^2(\Omega)F(\Omega) = \frac{\int \frac{dS_k}{|v_k|}\ \alpha_k^2(\Omega)F_k(\Omega)}{\int \frac{dS_k}{|v_k|}} \qquad 2\text{-}12$$

where

$$\alpha_k^2(\Omega)F_k(\Omega) = \int \frac{dS_{k'}}{|vk'|}\ \frac{1}{(2\pi)^3\hbar}\sum_{\lambda} |g_{k',k,\lambda}|^2\ \delta[\Omega - \omega_{\lambda,k'-k}] \qquad 2\text{-}13$$

where v_k is the group velocity of state k on the Fermi surface, dS_k is an element of Fermi surface area, and $g_{k',k,\lambda}$ describes electron scattering from k to k′ on the Fermi surface with creation of a phonon of energy $\hbar\omega_{\lambda,k-k'}$ and polarization λ. $F(\Omega)$ is the phonon density of states which can be directly obtained from neutron scattering. It is possible to obtain the full function $\alpha^2(\Omega)F(\Omega)$ from tunneling measurements which measure $N(\omega)$ and $\Delta(\Delta_0)$ as discussed by McMillan and Rowell, (1969). Since α is not a strong

function of Ω, $\alpha^2F(\Omega)$ can also be successfully compared with neutron diffraction experiments [Wolf, 1985]. By using the finite temperature form of these equations [Rainer, 1974; Vidberg and Serene, 1977], one can also solve for the transition temperature, T_c, where $\Delta(T)$ goes to zero.

A useful measure of the electron-phonon coupling strength is given by the McMillan parameter λ_{ep},

$$\lambda_{ep} = 2 \int_0^\infty \alpha^2(\omega)F(\omega)\omega^{-1} \, d\omega \qquad 2\text{-}14$$

Superconductors with values of $\lambda_{ep} < 1$ are generally considered to be "weak-coupled" and those with $\lambda_{ep} > 1$ are "strong-coupled". This integral gives the strongest weight to the low frequency phonons and is useful to keep in mind when considering the phonon spectrum of a superconductor. In fact, most strong-coupled high T_c superconductors (such as Pb, PbBi, and many A-15 compounds (e.g. Nb_3Sn)) have a large density of low frequency phonon modes. Most materials have a maximum density of low frequency phonon modes that can be supported before the material becomes structurally unstable. This is thought to be one of the fundamental limitations in creating materials with very high T_c's ($T_c > 30K$) [Varma, 1982].

The main experimental consequences of the strong-coupling calculations for tunnel junctions are some small corrections ($\propto (T_c/\theta_D)^2$) to the BCS tunneling density of states due to the energy dependence of $\Delta(\omega)$ and a change in the form of $\Delta(T)$. Our experimental measurement of $\Delta(T)$ for Ta films (see Fig. 3-8) agrees with these predictions ($(T_c/\theta_D)^2 \simeq 3\text{x}10^{-4}$ for Ta) and the findings of other experimenters [Wolf, 1985]. Additional strong-coupling effects such as gap anisotropy and quasiparticle lifetime effects are discussed below and in chapter V.

2.1.3 Anisotropy of the Superconducting Energy Gap

By considering the k dependence of $\alpha_k^2(\Omega)F_k(\Omega)$ in Eq. 2-13 before Fermi surface averaging in Eq. 2-12 it is easy to see that Δ can depend on k. The anisotropy in the distributions $\alpha_k^2(\Omega)F_k(\Omega)$ can be usefully discussed in terms of anisotropy in

1) the Fermi surface

2) the phonon spectrum

3) the form of the electron-phonon interaction.

Since these anisotropies are well known to exist in most metals, we may well expect that Δ depends on k. As discussed by Ohtsuka (1977), the experiments to date (based on upper critical field measurements) are in general agreement with respect to the presence of these effects and the influence of impurities. Impurities are found to introduce scattering which reduces anisotropy effects by averaging over the Fermi surface. A recent collection of articles [Weber, 1977] reviews a number of the experimental and theoretical issues involved in studying anisotropic superconductors.

It is reasonable to expect that tunneling measurements of the gap in single crystals would show a dependence on the tunneling direction of the electrons (to the extent that barrier tunneling is regarded as a directional process with most of the electrons injected in a cone of angle $\approx 10°$ about the barrier normal direction (see Wolf, [1985]). Surprisingly, however, there seems to be no consensus among the different tunneling experiments on the same material [Bostock, 1977]. Different tunneling experiments by different groups certainly show effects that appear to be due to anisotropy (i.e. multiple energy gaps), but the magnitude of these effects and their energy does not appear to be consistent from one experiment to the next. Recent work on MBE grown single crystal niobium films [Durbin, 1983] provides clear evidence for a k dependent $\alpha^2F(\Omega)$. Unfortunately, these authors were not able to obtain convergence with the McMillan [1965] inversion program

(to obtain $\alpha^2(\Omega)F(\Omega)$) for tunneling in the (111) direction. The 110 direction produced convergence in the normal fashion . This indicates a fundamental problem with the tunneling measurement or the model. The non-ideal nature of many tunnel barriers (as discussed in chapter V) may partially explain the present difficulties with these measurements. Clearly, further work and improved tunneling measurements are required to clear up the quantitative discrepancies in these experiments. Nonetheless, the experimental evidence clearly indicates the presence of anisotropy effects in pure materials and the destruction (Fermi surface averaging) of these effects by the addition of impurity scattering.

2.1.4 Quasiparticle and Phonon Lifetimes

The lifetime of low energy quasiparticle excitations and phonons are important in a variety of phenomena occurring in superconductors. As discussed in detail by Kaplan et al. (1976), the dominant quasiparticle relaxation processes are inelastic scattering with phonons and recombination with other quasiparticles to form a bound Cooper pair with the emission of a phonon of energy 2Δ in the process. These lifetimes can be related to the low-frequency part of the phonon density of states $F(\Omega)$ weighted by the square of the electron-phonon matrix element $\alpha^2(\Omega)$. Kaplan et al. (1976) have calculated the lifetime of a quasiparticle based on experimentally available information about $\alpha^2(\Omega)F(\Omega)$ for a number of materials. The rate can be separated into scattering and recombination rates which define the scattering and recombination lifetimes (τ_S and τ_r) respectively. These authors find good agreement between their calculations and the available experiments.

For the tunnel junction experiments discussed in chapter V, we are interested in the lifetime of a quasiparticle at the gap edge and at low temperatures ($T < 1/2\ T_c$). As discussed further in chapter V (see section

5.5.6), short quasiparticle lifetimes can lead to a broadened current rise at the sum gap in a tunnel junction and reduced mixer performance. For example, a lifetime τ of 10^{-11} seconds corresponds to an voltage broadening of $\Delta V \simeq \hbar/e\tau \simeq 100\ \mu V$ which is significant for SIS mixers at 36 GHz.

Without going into the details of the calculation, Kaplan et al. (1976) find that the low temperature quasiparticle lifetime at the gap edge is dominated by the quasiparticle recombination lifetime τ_r. The phonon scattering lifetime τ_s under these conditions ($T < 1/2\ T_c$), is long because there are relatively few states for a quasiparticle at the gap edge to decay into by spontaneous phonon emission. The recombination lifetime τ_r under these conditions ($T < 1/2\ T_c$ and $E \simeq \Delta$) is strongly temperature dependent due to the thermal population of quasiparticles available for recombination, but is always less than the phonon scattering lifetime for quasiparticles at the gap edge. The temperature dependent recombination lifetime found by Kaplan et al. (1976) is approximately given by

$$\frac{1}{\tau_r} \simeq (\pi)^{1/2}\left[\frac{2\Delta(0)}{kT_c}\right]^{5/2}\left[\frac{T}{T_c}\right]^{1/2}\frac{1}{\tau_o}\, e^{-\Delta/kT} \qquad 2\text{-}15$$

with typical values of τ_o for many materials in the range of 1×10^{-9} to 1×10^{-10} sec. τ_o can be estimated from the approximate functional form,

$$\tau_o \simeq \frac{\hbar}{kT_c}\ \frac{1}{2\pi\lambda_{ep}}\ (\theta_D/T_c)^2 \qquad 2\text{-}16$$

which shows that τ_o will be shortest for strong-coupled materials ($\lambda_{ep} > 1$) with large values of T_c/θ_D. The strong temperature dependence of τ_r is clear from Eq. 2-15 and reflects the exponential decrease in the quasiparticle population at low temperatures.

2.2 Superconducting Tunnel Junctions

Since the original discovery of tunneling in superconductors by Giaever (1960), tunnel junctions have been studied intensively by many groups. Superconductor-Insulator-Superconductor (SIS) and Superconductor-Insulator-Normal metal (SIN) tunnel junctions are interesting not only in their own right, but also serve as the most sensitive probe of the microscopic properties of superconducting state itself. As mentioned above and more thoroughly discussed by McMillan and Rowell, (1969) and Wolf, (1985) SIN tunnel junctions can be used to extract $\alpha^2(\Omega)F(\Omega)$ which is the product of the electron-phonon coupling $\alpha^2(\Omega)$ and the phonon density of states $F(\Omega)$. SIS tunnel junctions can also exhibit superconducting pair tunneling [Josephson, (1962); Barone and Paterno, (1982)]. This macroscopic quantum effect is the basis of the SQUID (Superconducting QUantum Interference Device) which has been extensively developed in the last 10-15 years for ultra-sensitive voltmeters and magnetic field measurement [Barone, 1982; Van Duzer, 1981]. Our primary interest in this thesis, however, is in the extremely non-linear quasiparticle I-V characteristic of an SIS junction caused by the singularity in the superconducting density of states in Eq. 2-1.

Cohen, Falicov, and Phillips (1962) formulated a Hamiltonian theory that describes the quasiparticle tunneling through a potential barrier in an SIS junction as illustrated in Fig. 2-1. This formalism can also describe the superconducting pair tunneling [Josephson, 1962; Barone, 1982], but we will concentrate on the quasiparticle results. The proposed Hamiltonian is

$$H = H_L + H_R + H_T + eV(t)N_L \qquad 2\text{-}18$$

where H_L and H_R are the Hamiltonians for the left and right electrodes respectively (i.e. the Hamiltonians that describe the superconducting state

discussed in section 2.1), V(t) is the applied voltage, and N_L is the number operator for the left electrode. H_T is given by,

$$H_T = \sum_{k,q} (T_{kq} c_k c_q^{+} + T_{kq}^{*} c_q c_k^{+}) \qquad 2\text{-}18$$

and N_L is given by,

$$N_L = c_k^{+} c_k \quad . \qquad 2\text{-}19$$

Here c_k and c_q are the second-quantized operators for particle creation or annihilation on the left and right respectively. The tunneling matrix elements $T_{kq} = T^{*}_{kq}$ are taken to be sufficiently small that the transfer of electrons across the barrier may be treated to lowest order in the coupling. A microscopic calculation of the tunneling current using Green's functions and standard linear response theory [Ambegaokar and Baratoff, 1963; Werthhamer, 1966; Rogovin and Scalapino, 1974] gives the dc quasiparticle current as,

$$I_{dc}(V) = \frac{2\pi e}{\hbar^2} \sum_{kq\sigma} \int_{-\infty}^{\infty} d\omega_1 \, d\omega_2 \, |T_{kq}|^2 \, A_L(k,\omega_1) \, A_R(q,\omega_2)$$

$$\times \, [f(\hbar\omega_1) - f(\hbar\omega_2)] \, \delta(eV/\hbar + \omega_1 - \omega_2) \qquad 2\text{-}20$$

where $f(\hbar\omega)$ is the Fermi distribution function ($f(\hbar\omega) = (e^{\hbar\omega/kT} + 1)^{-1}$) and $A_{L,R}$ are the single-particle distribution functions for the left- and right-side electrodes. For a normal metal tunnel junction, this equation reduces to

$$I_{NIN}(V) = V/R_N \qquad 2\text{-}21$$

where,

$$R_N = \frac{\hbar^3}{4\pi e^2 N_R(0) N_L(0) \langle|T^2|\rangle} \quad . \qquad 2\text{-}22$$

This is just the equation for a resistor and is commonly observed for non-superconducting tunnel junctions at low voltage (< 100 mV). If one of the electrodes is superconducting, then the equation for the current is given by

$$I_{SIN}(V) = \frac{1}{eR_N} \int_{-\infty}^{+\infty} \frac{E'}{(E'^2 - \Delta^2)^{1/2}} [f(E' - eV) - f(E')] \, dE' \qquad 2\text{-}23$$

The density of states diagram and resulting I-V curve for this situation are shown in Fig. 2-1. The SIS′ case for two different superconductors has a quasiparticle I-V which is given by

$$I_{SIS'}(V) = \frac{1}{eR_N} \int_{-\infty}^{+\infty} \frac{|E'|}{(E'^2 - \Delta_1^2)^{1/2}} \frac{|E' - eV|}{[(eV - E')^2 - \Delta_2^2]^{1/2}} \qquad 2\text{-}24$$

$$\times [f(E' - eV) - f(E')] \, dE'$$

and shown in Fig. 2-1c and 2-1d for a series of reduced temperatures ($t = T/T_c$). Notice that at all temperatures below T_c the I-V curve has a discontinuity at the sum-gap voltage $\Delta_1 + \Delta_2$. This results from the overlap of the singularity in the density of states in Eq. 2-24 which exist at all temperatures below T_c. There is also a difference gap structure which is due to thermally excited quasiparticles and is strongly temperature dependent ($\propto e^{-\Delta/kT}$).

As indicated above and also discussed in chapter V, gap anisotropy and

short quasiparticle lifetimes generally lead to a width of the current rise at the sum-gap and I-V curves that differ from the ideal case in Fig. 2-1. Additional mechanisms for non-ideal junction characteristics, particularly the mechanisms that explain "leakage" currents below the sum-gap, are discussed in chapter V.

2.3 Mixer Theory

2.3.1 Mixer Terminology

Any non-linear resistive device can act as a mixer to combine two input frequencies (a signal, ω_{sig}, and a local oscillator, ω_{LO}) and produce an intermediate frequency $\omega_{IF} = \omega_{sig} - \omega_{LO}$. Mixers are characterized by a coupled conversion gain G_C and an input noise power P_M. More precisely, the coupled gain of a mixer G_C is defined to be the ratio of the power coupled out of the mixer at the IF P^C_{IF} to the available power at the signal frequency P^A_{SIG},

$$G_C = P^C_{IF}/P^A_{SIG} . \qquad 2-25$$

The term "available power" refers to the power that would be coupled into a matched load (i.e., when the reflected power is zero) while the term "coupled power" refers to the power that is coupled into the actual load of interest. The available gain G_A is also important and is defined as the coupled gain G_C divided by an IF impedance mismatch factor $(1-|\rho|^2)$,

$$G_A = G_C/(1 - |\rho|^2) \qquad 2-26$$

where $|\rho|^2$ is the power reflection coefficient at the IF output of the mixer. ρ is the amplitude reflection coefficient. This form is only valid for $|\rho|^2 < 1$. If $|\rho|^2 > 1$ (as is the case for output impedances with a

negative real component), the available gain is infinite. The coupled gain and the power reflection coefficient are what one actually measures in a mixer experiment. These issues are discussed in more detail in chapter VI. If the output impedance of the mixer is Z_{IF} and the input impedance of the IF amplifier is Z_L, then

$$1 - |\rho|^2 = \frac{4\ \mathrm{Re}(Z_L)\ \mathrm{Re}(Z_{IF})}{|Z_{IF} + Z_L|^2} \quad . \qquad 2\text{-}27$$

If $Z_L = [|\mathrm{Re}(Z_{IF})| - i\ \mathrm{Im}(Z_{IF})]$, the load impedance (i.e., the IF amplifier input impedance) is matched to the IF output impedance of the mixer. For $\mathrm{Re}(Z_{IF}) > 0$ this corresponds to $|\rho|^2 = 0$, while for $\mathrm{Re}(Z_{IF}) < 0$ this corresponds to $|\rho|^2 = \infty$. As discussed below in section 2.3.2, these relations are only possible because G_A is independent of the IF load impedance Z_L [Torrey and Whitmer, 1948]. There is also an impedance mismatch at the signal port of the mixer but, this can not be included as a simple impedance mismatch correction because G_A is dependent on the signal impedance.

The noise power of a mixer P_M is defined[1] as the input signal power required to give a signal to noise ratio of one at the output. If this power is converted to a temperature with the Planck blackbody formula,

$$P_M = \frac{\hbar\omega\ B}{\exp(\hbar\omega/kT_M) - 1} \qquad 2\text{-}28$$

where B is the bandwidth in hertz, one can also define[1] a mixer noise temperature (see section 2.3.7 for a discussion of other definitions). This is

---

[1] IEEE Standard Dictionary of Electrical and Electronics Terms, Frank Jay, Editor, Wiley, New York (1977).

the physical temperature to which a matched termination at the signal port must be raised to double the output noise of the mixer. For a resistor R at low frequencies ($\omega << kT/\hbar$), this formula simply reduces to the well known Johnson noise formula ($P = kTB \Rightarrow \langle V^2 \rangle = 4kTRB$).

The importance of large gain and low noise in a mixer can be appreciated by considering the receiver noise power $P_R = P_{IF}^N/G_C + P_M$ referred to the mixer input. A mixer with large gain minimizes the contribution of the IF amplifier input noise power P_{IF}^N. A low mixer noise power is also important when the gain is large and the IF amplifier noise power is small.

2.3.2 Classical Mixer Theory

The classical theory of mixers has been well discussed by a number of authors [Torrey and Whitmer, 1948; Saleh, 1971; Held and Kerr, 1978]. The classical mixer theory, as well as the quantum mixer theory discussed in sections 2.3.3 to 2.3.5, describe the small signal mixing properties of a mixer in terms of a Y matrix

$$i_m = \sum_{m'} Y_{mm'} v_{m'} \qquad 2\text{-}29$$

where,

$$v_{sig}(t) = \mathrm{Re} \sum_{m=-\infty}^{\infty} v_m e^{i\omega_m t} , \qquad 2\text{-}30$$

$$i_{sig}(t) = \mathrm{Re} \sum_{m=-\infty}^{\infty} i_m e^{i\omega_m t} , \qquad 2\text{-}31$$

and

$$\omega_m = m\omega + \omega_o \qquad m = 0, \pm 1, \pm 2, \ldots . \qquad 2\text{-}32$$

The Y matrix (also called the admittance matrix) then describes how the strong pumping at the LO frequency ω (= ω_{LO}) mixes the output frequency ω_0 (= ω_{IF}) with all of the sidebands. The sideband frequencies (ω_m for m ≠ 0) and ω_0 are often referred to as the ports of the mixer. Throughout this thesis we will refer to a "three port" model which means that we are only considering the three frequencies ω_m with m = -1, 0 and 1. The LO frequency is always assumed to be present. The validity of the three port model is discussed in section 2.3.6.

In the classical mixer theory, the Y matrix elements are determined from the time dependent modulation of the dc I-V curve which produces a time dependent conductance

$$G^{cl}(t) = \frac{d}{dV_o} I_{dc}(V_o + V_{LO}\cos\omega t) = \sum_{m=-\infty}^{\infty} G^{cl}(m\omega)e^{im\omega t} \qquad 2\text{-}33$$

and yields,

$$Y^{cl}_{mm'} = G^{cl}[(m - m')\omega] \qquad 2\text{-}34$$

where,

$$G^{cl}(m\omega) = \frac{1}{2\pi}\int_{-\pi/\omega}^{\pi/\omega} G^{cl}(t)\, e^{-im\omega t}\, dt \qquad 2\text{-}35$$

$G^{cl}(m\omega)$ is simply the Fourier transform coefficient of $G^{cl}(t)$ in Eq. 2-33. This classical calculation assumes that the high frequency response of a non-linear device will be given simply by the form in Eq. 2-33. The quantum mixer theory [Tucker, 1979], discussed in sections 2.3.4 and 2.3.5, shows that this is not a valid assumption for I-V curves that are "sharp" on

the voltage scale $\hbar\omega/e$ (the exact meaning of "sharp" is discussed in section 2.3.4). Naturally, the quantum calculation of Y (see Eqs. 2-55 and 2-56) reduces to the classical form for rounded I-V's.

Once the Y matrix is determined, the mixer analysis is relatively straightforward. One simply places current generators I_m with output admittances Y_m at each port of the mixer and calculates the response. The equation to be solved then becomes

$$\begin{aligned} I_m &= i_m + Y_m v_m \\ &= \sum_{m'} (Y_{mm'} + Y_m \delta_{m,m'}) v_m \end{aligned} \qquad 2\text{-}36$$

which can be inverted to yield,

$$v_m = \sum_{m'} Z_{mm'} I_{m'} \qquad 2\text{-}37$$

where, in matrix notation,

$$||Z_{mm'}|| = ||Y_{mm'} + Y_m \delta_{m,m'}||^{-1} \; . \qquad 2\text{-}38$$

If a signal source I_s is placed at the m = 1 port (signal port) and the output is taken at the m = 0 port (IF port) as shown schematically in Fig. 2-2, the output voltage of the mixer may be written as

$$v_0 = Z_{00} \lambda_{01} I_s \qquad 2\text{-}39$$

where,

$$\lambda_{01} = Z_{01}/Z_{00} \; . \qquad 2\text{-}40$$

This is a particularly useful form for the output voltage because it can be

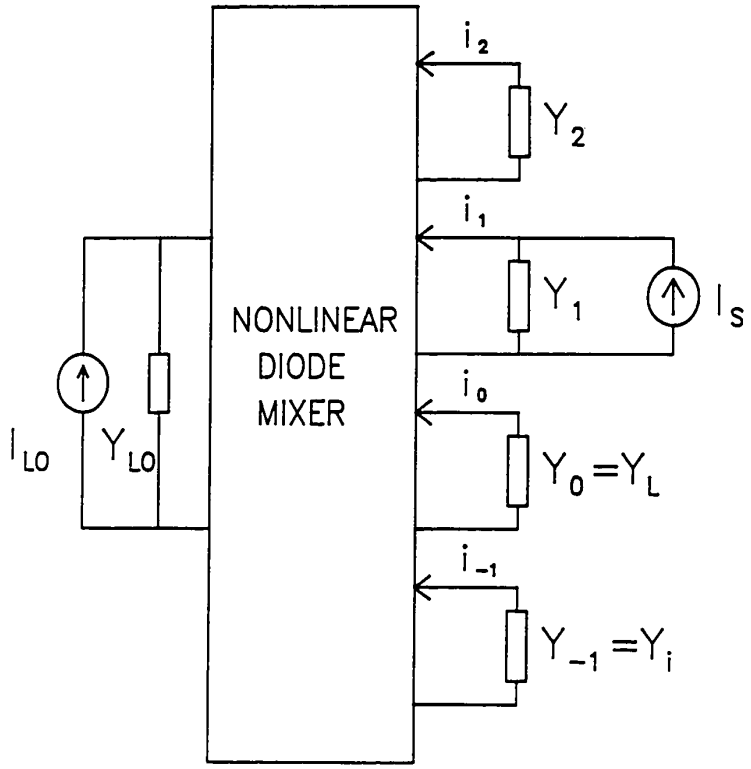

Fig. 2-2 Schematic diagram of a general nonlinear diode mixer with the signal ports labeled for $\omega_m = m\omega + \omega_0$. The signal frequency is ω_1, the IF output is ω_0, and the image port is ω_{-1}.

easily shown that λ_{01} is independent of Y_0 (= Y_L). This conclusion is obtained by explicitly performing the matrix inversion in Eq. 2-38. This implies that the mixer output can be viewed as a current source of magnitude $I_S\lambda_{01}$ with an output impedance of $Z_{IF} = (1/Z_{00} - Y_L)^{-1}$. This output impedance Z_{IF} is also independent of Y_L. The coupled and available gain of the mixer are then given by

$$G_C = 4G_SG_L|Z_{01}|^2$$

$$= \frac{4G_SG_L}{|Y_{IF} + Y_L|^2}\,|\lambda_{01}|^2 \qquad 2\text{-}41$$

and

$$G_A = G_S|\lambda_{01}|^2/G_{IF} \qquad (\text{for } G_{IF} > 0) \qquad 2\text{-}42$$

$$= \infty \qquad (\text{for } G_{IF} < 0).$$

In these expressions, G_S, G_L, and G_{IF} represent the real part of the respective admittance. These expressions show the explicit dependence of the coupled gain G_C on the small signal admittance matrix $Y_{mm'}$ and the embedding admittances Y_m.

The shot noise properties of the mixer can be described in terms of an H matrix where the noise current at the output of the mixer is given by

$$\langle[I_o]^2\rangle_{LO} = B\sum_{m,m'} \lambda_{0m}\lambda^*_{0m'}\,H_{mm'} \qquad 2\text{-}43$$

and

$$H_{mm'} = 2eI_{LO}[(m-m')\omega] \; . \qquad 2\text{-}44$$

$I_{LO}[(m-m')\omega]$ is the m-m′ Fourier component of the LO current and is given by

$$I_{LO}(m\omega) = \frac{1}{2\pi}\int_{-\pi/\omega}^{\pi/\omega} I_{LO}(t)\, e^{-im\omega t}\, dt \qquad 2\text{-}45$$

The shot noise in the quantum theory has the same form but, with a different definition of the H matrix (see Eq. 2-67). The current fluctuations (Johnson noise) in the image terminations ($m \neq 0$ or 1) also contribute to the output current noise as

$$\langle [I_o]^2 \rangle_{IM} = B \sum_{m \neq 0,1} |\lambda_{0m}|^2\, 4kT_m G_m \qquad 2\text{-}46$$

where G_m is the real part of the embedding admittance at ω_m and T_m is the temperature of that admittance. The quantum generalization of this term to include zero point fluctuations is discussed in section 2.3.6 and 2.3.7. By equating the sum of these output noise currents to that produced by an available signal power at the input one obtains the minimum detectable signal power P_{det} (for a signal to noise ratio of one) to be

$$P_{det} = \frac{\langle |I_o|^2 \rangle_{LO} + \langle [I_o]^2 \rangle_{IM}}{4G_S |\lambda_{01}|^2} \qquad 2\text{-}47$$

The classical theory predicts that the available power gain G_A of a mixer should always be less than one while the noise power can approach zero (for an ideal device at T = 0K). A zero noise heterodyne mixer is clearly inconsistent with the general quantum noise limits discussed in section 2.3.7.

2.3.3 Photon Assisted Tunneling

Before trying to understand the quantum mixer theory, it is very helpful to have a clear picture of the photon assisted tunneling process in SIS tunnel junctions. Photon assisted tunneling in SIS tunnel junctions, as first observed by Dayem and Martin (1962) and explained by Tien and Gordon (1962), is a process by which incident radiation can provide the extra energy required for quasiparticle tunneling at dc bias voltages less than the sum-gap. This process is illustrated in Fig. 2-3 for two unequal superconductors A and B.

The theory proposed by Tien and Gordon assumes that the junction is driven by a time dependent potential $V(t) = V_\omega \cos(\omega t)$ in Eq. 2-18. This assumption implies that all higher harmonics of the ac waveform are shorted. This is often the case for real tunnel junctions because the junction capacitance acts as a low impedance shunt for the higher harmonics. The dc current under these conditions is found to be

$$I_o(V_o, V_\omega) = \sum_{n=-\infty}^{\infty} J_n^2(eV_\omega/\hbar\omega)\, I_{dc}(V_o + n\hbar\omega/e) \qquad 2\text{-}48$$

This series is a Bessel function weighted sum of dc currents at voltages separated from the bias voltage V_o by $\hbar\omega/e$. This form describes the photon assisted tunneling steps illustrated in Fig. 2-3 which were first observed by Dayem and Martin and are an important part of the operation of SIS mixers. For an SIS mixer, the strong local oscillator pump power produces a pumped I-V curve such as that in Fig. 2-4. Mixing occurs when a weak signal (perturbation) is added to the strong LO pump to produce a modulation of the pumped I-V at ω_{IF} (the IF output). We note that the classical way of calculating the pumped I-V is to apply the time dependent

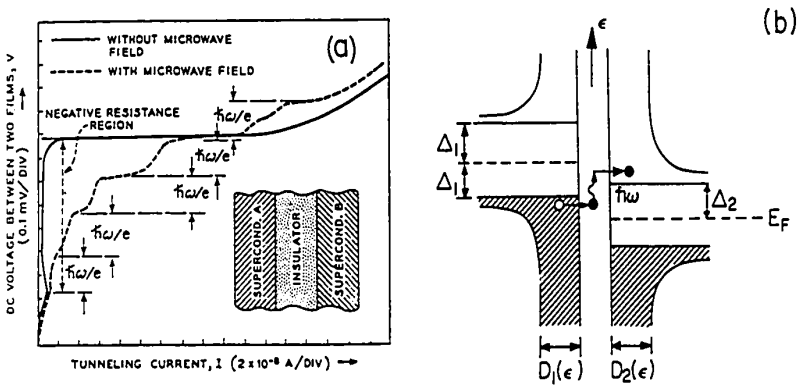

Fig. 2-3 a) Photon assisted tunneling steps on an SIS ($Al/Al_2O_3/In$) tunnel junction as first observed by Dayem and Martin (1962)[Figure is from Tien and Gordon (1963)] b) Density of states representation of the photon assisted tunneling process for a single particle event.

voltage to the dc I-V and compute the time average dc current. If one applies this simple technique to the dc I-V characteristic of an SIS' tunnel junction in Eq. 2-24, it is not possible to generate the photon assisted tunneling steps which are discussed above. Of course, the low frequency limit of Eq. 2-48 reduces to the classical result [Tucker, 1979]. This limit of Eq. 2-48 is shown explicitly below for $eV_\omega << \hbar\omega$ and $\hbar\omega/e$ much less than the voltage scale of the non-linearity. The classical result is simply a Taylor series expansion of the non-linear I-V to second order in V_ω.

$$I_o(V_o,V_\omega) \simeq I_o(V_o,0) + \frac{1}{2} V_\omega^2 \left[\frac{I_o(V_o + \hbar\omega/e) - 2I_o(V_o) + I_o(V_o - \hbar\omega/e)}{2(\hbar\omega/e)^2} \right] \qquad 2\text{-}49a$$

$$\simeq I_o(V_o,0) + \frac{1}{2} V_\omega^2 \left. \frac{d^2 I_o}{d V_\omega^2} \right|_{V_\omega=0} \qquad \text{(Classical Result)} \qquad 2\text{-}49b$$

These equations also give a useful working definition of when an I-V curve should produce strong quantum effects (i.e. what is a "sharp" I-V). Namely, strong quantum effects should be seen when the dc I-V curve changes rapidly enough on the voltage scale of $\hbar\omega/e$ that the finite difference forms of the derivatives in 2-49a do not approximately equal the exact derivatives in 2-49b from the dc I-V curve.

The calculation of a pumped I-V curve for a large capacitance junction ($\omega R_N C_J >> 1$) is relatively straightforward because one can assume that V_ω is independent of the dc bias voltage V_O. The more interesting case, however, occurs when the junction capacitance is small or is approximately resonated out by external tuning elements (microwave matching). In this case one must consider the finite impedance of the current source (or

Thevenin equivalent voltage source) that is driving the junction. The equivalent circuit in this case is shown in Fig. 7-2 and discussed more fully in section 7.1. Essentially, the input admittance of the junction at ω_{LO} is a function of the dc bias voltage V_0. This dependence on V_0 implies that the LO voltage amplitude V_ω can depend on the bias voltage V_0. This variation of V_ω is largest when Y_{LO} (the output admittance of the LO current source) is small compared to the tunnel junction admittance. If V_ω decreases as V_0 increases, it is possible to produce flat (large dynamic resistance R_D) or even negative resistance photon steps on the pumped I-V curve. The experimental observation of this effect [McGrath et al., (1981); Smith et al., (1981); and Kerr et al., (1981)] confirms the basic ideas discussed above and is intimately linked to the observation of large gain in SIS mixers (see sections 2.3.4 and 2.3.5). We have also observed this effect in sharp tantalum junctions as discussed in chapter VI.

A simple model of this effect proposed by Smith et al., (1981), shows that certain criteria must be met in order to observe negative resistance. Essentially, the dc dynamic resistance R_D of the pumped junction is given by differentiating Eq. 2-48 to obtain

$$\frac{dI(V_o,P_{LO})}{dV_o} = \sum_{n=-\infty}^{\infty} \left[J_n^2(\alpha) \frac{dI_n}{dV_o} + \frac{d\alpha}{dV_o} \frac{\partial(J_n^2(\alpha))}{\partial\alpha} I_n \right] = R_D \qquad 2\text{-}50$$

with the constraint of constant available LO power,

$$P_{LO} = |I_\omega + V_\omega Y_{LO}|^2/8G_{LO} \quad , \qquad 2\text{-}51$$

where I_ω is given by,

$$I_\omega(V_o,V_\omega) = A\cos\omega t + B\sin\omega t \qquad 2\text{-}52$$

with the coefficients A and B given by,

$$A = \sum_{n=-\infty}^{\infty} J_n(\alpha)[J_{n+1}(\alpha) + J_{n-1}(\alpha)]I_{dc}(V_o + n\hbar\omega/e) \qquad 2\text{-}53$$

$$B = \sum_{n=-\infty}^{\infty} J_n(\alpha)[J_{n+1}(\alpha) - J_{n-1}(\alpha)]I_{KK}(V_o + n\hbar\omega/e) \qquad 2\text{-}54$$

where $\alpha = eV_\omega/\hbar\omega$ and I_{KK} is the Kramers Kronig transform of the unpumped dc I-V (see section 2.3.5). For voltage driven junctions, $d\alpha/dV_o$ is zero which implies that the sum in Eq. 2-50 is always positive and that negative resistance will not be observed. The exact conditions for observing negative resistance with an arbitrary I-V curve will depend on the value of Y_{LO}, the subgap leakage current and the I-V sharpness. I-V curves with a large subgap conductance or a broad (compared to $\hbar\omega/e$) current rise at the sum gap do not show negative resistance. In addition, we note that a classical calculation of the pumped I-V can not produce flat or negative resistance steps [Tucker and Feldman, 1985]. The next section shows how these flat or negative resistance steps are intimately linked to the observation of large gain in SIS mixers.

2.3.4 Simple SIS Mixer Model

This section describes a simple picture of SIS mixers which illustrates the physical origin of the large available gain ($G_A >> 1$) predicted by the full quantum mixer theory. This model is a combination of ideas presented by Tucker and Feldman, (1985) as well as work by McGrath et al. (1981) and Smith et al. (1981). As discussed in the previous section, pumped I-V curves can have photon steps with a large or negative dynamic resistance R_D (see Fig. 2-4). The equivalent circuit for this discussion is also shown

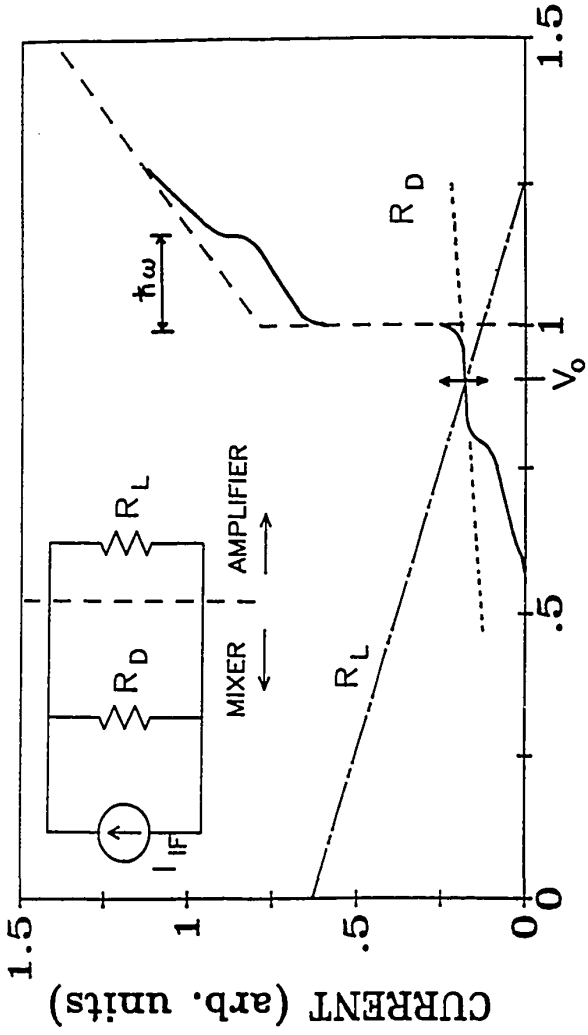

Fig.2-4 Hypothetical pumped I-V and equivalent circuit for the IF output in the simple SIS mixer model discussed in section 2.3.4.

Fig. 2-4. If an external signal is applied with $\omega_S \simeq \omega_{LO}$, beating of the two frequencies can result in an amplitude modulation (AM) of the LO pump power at $\omega_{IF} = \omega_{LO} - \omega_S$. This causes the photon step in Fig. 2-4 to oscillate up and down at the beat frequency (IF) and produce a voltage on the load conductance $G_L = 1/R_L$ at ω_{IF} (this is the IF output voltage). As discussed in section 2.3.2 (see Eq. 2-39) and illustrated in Fig. 2-4, the IF output of a mixer is equivalent to a current source of magnitude I_{IF} (= $\lambda_{01}I_S$) with an output impedance of R_D. For low IF's ($\omega_{IF} \simeq 0$), R_D is equal to the dynamic resistance of the pumped I-V at the bias voltage V_0 (see McGrath et al., 1981; and Feldman, 1982). The quantum mixer theory allows R_D to approach infinity and become negative while still maintaining a finite value for the IF output current source. Since the available output power is given by $|I_{IF}|^2R_D/8$, this situation corresponds to infinite available gain G_A. If the load resistance R_L is matched to the IF output impedance R_D, large coupled gain G_C (approaching infinite) can also be produced. A practical limit to the infinite gain mechanism occurs when the magnitude of IF output voltage approaches a significant fraction γ_0 of the photon step width $\hbar\omega/e$. This output saturation corresponds to a maximum input signal power (saturation power) of $P_{sat} \simeq (\gamma_0\hbar\omega/e)^2/2G_CR_L$ [Tucker and Feldman, 1985; Smith and Richards, 1982] and limits the dynamic range of large gain SIS mixers. For a 1 dB gain compression $\gamma_0 \simeq 0.2$.

2.3.5 Quantum Mixer Theory

The quantum theory of mixing developed by Tucker, (1979) and recently reviewed by Tucker and Feldman (1985), describes the performance of non-linear resistive mixers where the voltage scale of the non-linearity is small compared to the photon voltage $\hbar\omega/e$. This theory builds on the original work on photon assisted tunneling in superconductors by Tien and Gordon, (1963) which is discussed in section 2.3.3. The quantum mixer

theory makes the remarkable prediction that a mixer with a non-linearity that is sharp on the voltage scale $\hbar\omega/e$ ($\simeq$ 150 μV at 36 GHz) can achieve conversion gain $G_A >> 1$ and an input noise power that approaches the quantum limit of $\hbar\omega B$ (one photon per hertz). This corresponds to a noise temperature of $\hbar\omega/k\ln 2 \simeq$ 2.5K at 36 GHz. As discussed in chapter I and VI, these effects have been experimentally observed by several groups [McGrath et al.,(1985 and 1981); D'Addario, (1984); Kerr et al., (1981)]. Chapter VII describes a computer implementation of the Tucker theory in the three port approximation. The measurements of Ta junctions in this thesis represent an accurate test of a number of the theoretical predictions for sharp SIS junctions that show strong quantum mixing effects.

The starting point for the quantum mixer theory is to self-consistently determine the large signal local oscillator waveform impressed on the tunnel junction. This is, in general, an extremely complicated non-linear problem that requires the knowledge of embedding impedances at all harmonics of the LO frequency [see Tucker and Feldman, (1985); Hicks, (1985); and Kerr (1975)]. Tucker's original calculation [Tucker, 1979] allows for the treatment of this general case; but, since this is rarely feasible in practice, we will only discuss the case of a sinusoidal LO drive where all of the higher harmonics are shunted by the junction capacitance. This also means that we are only considering the 3 port approximation of the full theory (i.e. the only frequencies that enter the Y matrix calculation are the signal ω_S, the image ω_I, and the IF ω_{IF}). The validity of the 3 port approximation is discussed in section 2.3.6.

Once the amplitude of the LO waveform $V_{LO} = V_\omega \cos\omega t$ is known (see also section 7.1), the elements of the small signal admittance matrix $Y_{m,m}{}'$ can be determined. The form derived by Tucker is

$$Y_{m,m'} = G_{m,m'} + iB_{m,m'}$$

where,

$$G_{m,m'} = \frac{e}{2\hbar\omega_{m'}} \sum_{n,n'=-\infty}^{\infty} J_n(eV_\omega/\hbar\omega)J_{n'}(eV_\omega/\hbar\omega)\delta_{m-m',n'-n} \qquad 2\text{-}55$$

$$\times \left[\{I_{dc}(V_o + n'\hbar\omega/e + \hbar\omega_{m'}/e) - I_{dc}(V_o + n'\hbar\omega/e)\}\right.$$

$$\left. + \{I_{dc}(V_o + n\hbar\omega/e) - I_{dc}(V_o + n\hbar\omega/e - \hbar\omega_{m'}/e)\}\right]$$

$$B_{m,m'} = \frac{e}{2\hbar\omega_{m'}} \sum_{n,n'=-\infty}^{\infty} J_n(eV_\omega/\hbar\omega)J_{n'}(eV_\omega/\hbar\omega)\delta_{m-m',n'-n} \qquad 2\text{-}56$$

$$\times \left[\{I_{KK}(V_o + n'\hbar\omega/e + \hbar\omega_{m'}/e) - I_{KK}(V_o + n'\hbar\omega/e)\}\right.$$

$$\left. - \{I_{KK}(V_o + n\hbar\omega/e) - I_{KK}(V_o + n\hbar\omega/e - \hbar\omega_{m'}/e)\}\right] .$$

In these expressions, I_{KK} is the Kramers Kronig transform of the dc I-V characteristic and is given by,

$$I_{KK}(V) = P\int_{-\infty}^{\infty} \frac{dV'}{\pi} \frac{I_{dc}(V') - V'/R_N}{V' - V} \qquad 2\text{-}57$$

If these Y matrix elements are used in the Y mixer model in Eq. 2-38, the mixer gain and output impedance can be calculated in the same way as the classical analysis. For low IF ($\omega_{IF} << \omega_{LO}$), the following important symmetry properties of the Y matrix can be shown,

$$Y_{0,1} = Y^*_{0,-1} \qquad Y_{1,0} = Y^*_{-1,0} \qquad Y_{1,1} = Y^*_{-1,-1}$$

$$Y_{1,-1} = Y^*_{-1,1} \qquad B_{00} \simeq B_{01} \simeq B_{10} \simeq 0 \qquad 2\text{-}58$$

The fact that these Y matrix elements allow large and infinite available gain is by no means obvious. In fact, this important point was not initially recognized when the theory was first developed [Tucker, 1979 and 1980].

Some physical insight into the quantum mixer theory is provided by examining the case where the following approximations can be made;

a) $\omega_{IF} << \omega_{LO}$

b) only the real components of Y are important (i.e. $B_{m,m}{}' = 0$)

c) $Y_{-1} = Y_1 = Y_{LO} = G_S$ (i.e. the embedding admittances at the signal, image and LO frequencies are equal to the signal conductance G_S. We refer to mixers with equal signal and image terminations as double sideband (DSB) mixers.)

Under these conditions, Tucker and Feldman, (1985) have shown that the important G values (G = Re (Y)) are given by the simplified forms

$$G_{00} = \sum_{n=-\infty}^{\infty} J_n^2(\alpha) \frac{dI_{dc}(V_o + n\hbar\omega/e)}{dV_o} = \frac{\partial I_o}{\partial V_o} \qquad 2\text{-}59$$

$$G_{10} = G_{-10} = \frac{1}{2} \sum_{n=-\infty}^{\infty} J_n(\alpha)[J_{n+1}(\alpha) + J_{n-1}(\alpha)] \frac{dI_{dc}(V_o + n\hbar\omega/e)}{dV_o} = \frac{\partial I_\omega}{2\,\partial V_o} \qquad 2\text{-}60$$

$$G_{01} = G_{0-1} = \frac{e}{\hbar\omega} \sum_{n=-\infty}^{\infty} J_n(\alpha)J_{n+1}(\alpha)\{I_{dc}[V_o + (n+1)\hbar\omega/e] - I_{dc}[V_o + n\hbar\omega/e]\}$$

$$= -\frac{\partial I_o}{\partial V_\omega} \qquad 2\text{-}61$$

$$G_{11} + G_{1-1} = \frac{e}{2\hbar\omega} \sum_{n=-\infty}^{\infty} [J_n^2(\alpha) + J_{n-1}(\alpha)J_{n+1}(\alpha)]$$

$$\times \{I_{dc}[V_o + (n+1)\hbar\omega/e] - I_{dc}[V_o + (n-1)\hbar\omega/e]\} \qquad 2\text{-}62$$

$$= -\frac{\partial I_\omega}{\partial V_\omega}$$

By explicitly performing the matrix inversion in Eq. 2-38

$$\begin{vmatrix} Z_{11} & Z_{10} & Z_{1-1} \\ Z_{01} & Z_{00} & Z_{0-1} \\ Z_{-11} & Z_{-10} & Z_{-1-1} \end{vmatrix} = \begin{vmatrix} (G_{11} + G_s) & G_{10} & G_{1-1} \\ G_{01} & (G_{00} + G_L) & G_{0-1} \\ G_{-11} & G_{-10} & (G_{-1-1} + G_s) \end{vmatrix}^{-1} \qquad 2\text{-}63$$

we obtain the IF output conductance of the mixer to be,

$$G_{IF} = 1/R_D = 1/Z_{00} - G_L = G_{00} - \frac{2\, G_{01}G_{10}}{G_s + G_{11} + G_{1-1}} \qquad 2\text{-}64$$

$$= G_{00}\left[1 - \frac{\eta}{1 + G_s/(G_{11} + G_{1-1})}\right]$$

where η is defined in Eq. 2-66. The IF output current source $I_{IF} = \lambda_{01}I_{sig} = (Z_{01}/Z_{00})I_{sig}$ is given by,

$$I_{IF} = \lambda_{01}I_{sig} = \frac{-G_{01}}{G_s + G_{11} + G_{1-1}} I_{sig} \qquad 2\text{-}65$$

As pointed out in section 2.3.2, both λ_{01} and G_{IF} are clearly independent of the load conductance G_L. From Eq. 2-65, it is clear that we want to maximize G_{01} to obtain a large output current source for the widest range of signal conductances G_S. This makes physical sense in that maximizing G_{01} maximizes the change of I_0 for a given change in V_ω (see Eq. 2-61). In the simple mixer model of section 2.3.4 (see Fig. 2-4), this maximizes the vertical motion of the photon step and produces the largest output signal.

Model calculations for the Ta mixer experiments using the full Y matrix expressions in Eqs. 2-55 and 2-56 (see chapter VII) show that the gain does indeed maximize near the point where G_{01} is a maximum. This confirms the fact that the simple ideas discussed here are capturing the essential elements necessary to explain the (initially surprising) large gain and negative resistance in SIS mixers.

By differentiating the available gain G_A with respect to the signal conductance G_S, it can be shown (Tucker and Feldman, 1985; Torrey and Whitmer, 1948) that the maximum gain of a mixer is obtained when $G_S = (G_{11} + G_{1\text{-}1})(1 - \eta)^{1/2}$ (only for $\eta \leq 1$!), where η is given by

$$\eta = \frac{2G_{01}G_{10}}{G_{00}(G_{11} + G_{1\text{-}1})} \quad . \qquad 2\text{-}66$$

The maximum gain in this case is $G_{max} = \eta/(1 + (1 - \eta)^{1/2})^2$. It can also be shown that η never exceeds unity in the classical mixer theory which implies a maximum conversion gain of unity. The quantum mixer theory allows $\eta > 1$ which implies large (and infinite) available gain for the right rf embedding impedances as discussed above. $\eta > 1$ also allows G_{IF} in Eq. 2-64 to become zero and negative for small G_S (i.e. current driven junctions). The point where G_{IF} approaches zero corresponds to infinite available gain in the quantum mixer theory.

The quantum theory also predicts the shot noise contribution to the mixer noise by calculating an H matrix as discussed in section 2.3.2. The H matrix obtained by Tucker after considerable manipulation is

$$H_{m,m'} = e \sum_{n,n'=-\infty}^{\infty} J_n(eV_\omega/\hbar\omega) J_{n'}(eV_\omega/\hbar\omega) \delta_{m-m',n'-n} \qquad 2\text{-}67$$

$$\left[\coth[\beta(eV_o + n'\hbar\omega + \hbar\omega_{m'})/2] I_{dc}(V_o + n'\hbar\omega/e + \hbar\omega_{m'}/e)\right.$$

$$\left. + \coth[\beta(eV_o + n\hbar\omega - \hbar\omega_{m'})/2] I_{dc}(V_o + n\hbar\omega/e - \hbar\omega_{m'}/e)\right] .$$

When this complicated expression is used in Eq. 2-43 and the limiting form for $m=m'=0$ and $V_\omega \simeq 0$ ($\lambda_{00} = 1$) is examined, one obtains the well known expression for the quasiparticle noise current of an SIS tunnel junction at a bias voltage V_0 [Rogovin and Scalapino, (1974)]

$$\langle [I_o]^2 \rangle \simeq B\, \lambda_{00}\, \lambda_{00}^{*}\, H_{00} \qquad 2\text{-}68$$

$$= Be \left[\coth[\beta(eV_o+\hbar\omega)/2] I_{dc}(V_o+\hbar\omega/e) + \coth[\beta(eV_o-\hbar\omega)/2] I_{dc}(V_o-\hbar\omega/e)\right]$$

In the limit of $eV_0 >> \hbar\omega$ and $eV_0 >> kT$ this formula reduces to ordinary shot noise

$$\langle [I_o]^2 \rangle = B\, 2eI_{dc}(V_o) \qquad 2\text{-}69$$

while in the limit of $kT >> eV_0 >> \hbar\omega$ the formula reduces to

$$\langle [I_o]^2 \rangle = B\, 4kT\, [I_{dc}(V_o)/V_o]] \qquad 2\text{-}70$$

which is simply the Johnson noise for a linear I(V) characteristic. These results and the dependence of the shot noise on the dc current $I_{dc}(V_O)$ emphasize the need for junctions with low leakage currents below the sum gap for low noise SIS mixers. It is important to note, however, that the noise of an operating SIS mixer will involve the evaluation of the full H matrix for the actual mixing conditions. Fortunately, the result of this calculation is that shot noise power can be quite low (for ideal SIS junctions) and even approach zero under the right conditions (see section 2.3.7). This means that the noise of an SIS mixer is not directly related to the pumped dc current as one would naively expect for simple shot noise from a dc I-V characteristic.

2.3.6 Validity of the Three Port Mixer Approximation

As discussed above, calculations involving more than three ports are much more complicated because of the need to accurately know the embedding impedances at higher sideband frequencies and to self-consistently solve for the LO waveform at harmonic frequencies. Hicks et al. (1985) have attempted to solve this problem by treating the large signal response of the tunnel junction in the time domain rather than the frequency domain as was done in section 2.3.5. Unfortunately, the results of this analysis are not yet extensive enough to draw general conclusions. Despite these difficulties, it is useful to have a rough idea of the range of validity for the three port model. Qualitatively, the three port model should be valid when the higher harmonics are effectively "shorted" by the junction capacitance. Feldman and Rudner (1983) observed depressed performance (compared to three port model calculations) on the first photon step for junctions with $\omega R_N C < 4$ and suggest this criteria as a rough guide for the validity of the three port model. Good agreement with the theory was obtained by these authors for mixing on the second step (even if $\omega R_N C$

< 4). We note, however, that the junctions in those experiments were not particularly sharp compared to $\hbar\omega/e$ and only displayed weak quantum effects (the highest observed gain was only -2dB). The required $\omega R_N C$ may in fact be larger for sharper junctions which show stronger quantum mixing effects. This possibility is supported by our measurements with sharp Ta junctions discussed in chapters VI and VII. These junctions have an $\omega R_N C$ product of $\simeq$ 4 and show depressed performance (compared to the three port model) on all four photon steps measured. The disagreement with the three port model increases for photon steps that are closer to the gap.

The only five port calculation that has been performed for an SIS mixer is contained in the work of Richards and Shen (1980). These authors simply assumed that the higher harmonics were terminated in the junction capacitance and solved for the LO waveform. The results of the five port model demonstrate that the theoretical performance on photon steps near the gap is reduced from the three port predictions. More extensive calculations would clearly be desirable. Recent measurements and extensive calculations by Siegel and Kerr (1984) for Schottky diode mixers (using classical mixer theory) show that the inclusion of the second harmonic sidebands gives corrections for that case which are ≤ 2dB. These corrections give improved agreement between theory and experiment for these classical Schottky diode mixers.

2.3.7 Quantum Noise in SIS Mixers

The quantum limit for noise in SIS mixers has been recently discussed by a number of authors [Tucker and Feldman, (1985); Devyatov et. al., (1986); Caves (1982); Wengler and Woody (1986); and Feidman (1986)] and is briefly summarized in this section. The general theoretical work of Caves (1982) shows that any high-gain linear amplifier which is phase preserving (Caves refers to this as a "phase insensitive" amplifier) must add a noise

power referred to the input of at least,

$$P^{A}_{min} = A\hbar\omega B \geq |1-(1/G)|\hbar\omega B/2 \qquad 2\text{-}71$$

where G is the photon number gain, A is the minimum noise power added by the amplifier in units of $\hbar\omega$, and B is the bandwidth of the amplifier. An SIS mixer acts as a "high-gain linear amplifier" in that it is linear, preserves phase information and almost always operates with a large photon number gain. The minimum of this expression for G >> 1 produces an added noise power of $\hbar\omega/2$ per unit bandwidth. This minimum noise is a direct consequence of the Heisenberg uncertainty principle. Assuming that the input signal to this quantum limited amplifier (an SIS mixer in our case) is accompanied by blackbody radiation at a physical temperature T the total noise power referred to the input is given by,

$$P_N = [1/2 + 1/2\coth\{\hbar\omega/2kT\}]\hbar\omega B \qquad 2\text{-}72$$

as in Eq. 3.33 of Caves (1982) paper. The second term on the right is essentially the Planck radiation law with the addition of zero point fluctuations. At T=0K this expression reduces to a noise power of $\hbar\omega$ per unit bandwidth which is the irreducible noise at the input to the amplifier. A possible exception to this case, which is not directly relevant to the experiments discussed here, can occur if the input radiation is prepared in a "squeezed" state as discussed by Caves (1982) and Devyatov et. al. (1986). In this case, the zero point fluctuations are reduced below $\hbar\omega/2$ in one of the two quadratures of the input signal (either the "cos ωt" or "sin ωt" component) and a lower input noise can result for that quadrature.

The quantum theory of mixing predicts the shot noise contribution to the noise power of SIS mixers due to fluctuations in the LO driven

quasiparticle currents. As discussed by Feldman (1986) and Wengler and Woody (1986), this shot noise power can approach zero for a DSB (equal signal and image termination) mixer and $\hbar\omega/2$ for a SSB (shorted image) mixer. In the DSB mixer case, the apparent violation of Caves's general argument for the minimum noise added by a high-gain linear amplifier is resolved by including the zero point noise $\hbar\omega/2$ of the image termination and referring it to the input signal port. Experimental evidence for the coupling of zero point fluctuations from the dissipative parts of the RF terminations in tunnel junctions has recently been seen in measurements by Koch et. al. (1982) with tunnel junction SQUIDS. Zorin (1985) argues that the zero point fluctuations in the terminating conductance G_i at the image frequency port of an SIS mixer can be included by using a current generator of mean-square amplitude

$$\langle i^2\rangle = 2G_i\hbar\omega B\coth(\hbar\omega_i/2kT). \qquad 2\text{-}73$$

Zorin (1985) and Devyatov et. al. (1986) also argue that this lumped circuit approach is equivalent to a complete quantum-mechanical treatment including zero point fluctuations. Recent work by Wengler and Woody (1986) has shown that these results are rigorously correct when all of the currents and voltages in Tucker's theory are treated as quantum mechanical operators in the second quantized formalism. These authors also show that the minimum noise added by an SIS mixer is $\hbar\omega B/2$ for an arbitrary image termination. This is a remarkable conclusion in that two different physical mechanisms are adding together to produce a minimum noise that is always greater than $\hbar\omega B/2$. When the noise from one mechanism is small the other appears to compensate in such a fashion that the minimum noise is always $\hbar\omega B/2$.

In order to make meaningful comparisons with our experimental

measurements, we need a theoretical minimum input noise power. Since our measurement technique, discussed in chapter VI, measures the irreducible (T=0K) noise power at the mixer input it is appropriate to compare these measurements with the zero temperature limit of P_N which is $\hbar\omega B$ (see Eq. 2-72). For the purpose of comparison with other work on low noise mixers, we also calculate a mixer noise temperature T_M by equating the minimum input noise power to the power radiated by a blackbody using the Planck blackbody radiation formula in Eq. 2-28 and solving for the temperature. If the irreducible noise power at the mixer input is $\hbar\omega B$ the corresponding noise temperature is $T_M = \hbar\omega/k\ln 2$ which we take as the quantum limit for the mixer noise temperature. It should be noted, however, that there is no universally accepted definition of noise temperature and other authors may use different definitions such as $P_N = kTB$. Although these different definitions reduce to the same high temperature limit of $P_N = kTB$, their quantum limits are not the same and these different limits are shown in Table II-1. This is a consequence of the fact that noise temperature is not a very useful concept for devices that are operating near the quantum noise limit with $\hbar\omega >> kT$. Because of these difficulties with the definition of noise temperature, we also give the experimentally measured input noise power in units of $\hbar\omega B$ along with our calculated noise temperatures.

TABLE II-1 Table of different values for the quantum noise temperature depending the definition of quantum noise power and quantum noise temperature. The Planck definition in the right hand column is used in this thesis.

	DEFINITION OF NOISE TEMPERATURE	
NOISE POWER	$P_N = kTB$	$P_N = \frac{\hbar\omega\ B}{\exp(\hbar\omega/kT) - 1}$
$\hbar\omega B$	$T_M = \hbar\omega/k$	$T_M = \hbar\omega/k\ln 2$
$\hbar\omega B/2$	$T_M = \hbar\omega/2k$	$T_M = \hbar\omega/k\ln 3$

III. MATERIAL PROPERTIES

In this chapter, we review the important thin film materials issues involved in tunnel junction fabrication and the choices that have been made for the optimization of SIS mixers. The relatively new technique of ion-beam sputter deposition is also discussed with an emphasis on the improvements that have been made over previous work. One of the most significant of our improvements is the ability to deposit high quality Nb and Ta refractory superconducting films on room temperature substrates with properties approaching those of the bulk material. This had not been achieved prior to this study. The use of room temperature substrates is important for photoresist lift-off patterning as discussed in chapter IV. We have also discovered that a thin (>3Å) Nb underlayer is required for the nucleation and growth of Ta films in the bulk bcc crystal structure. The transport and structural properties of the ion-beam deposited Nb and Ta films are also discussed.

A number of important factors have been considered in the choice of materials and deposition techniques for tunnel junction fabrication. Some of the most important criteria are the following:

1. Materials and tunnel junctions must survive repeated thermal cycling from room temperature to cryogenic temperatures of 1-10K.
2. Materials must have a single well defined superconducting energy gap without excessive broadening due to material inhomogeneities, energy gap anisotropy, or short quasiparticle lifetimes as discussed in chapters II and V.
3. Base electrode materials must form a high quality native oxide tunnel barrier or be compatible with artificial tunnel barrier techniques at high Josephson critical current densities.

4. Counter-electrode material must not react with the tunnel barrier to produce shorts or a damaged interface region.
5. The deposition technique should produce high purity films with a high T_c on room temperature substrates. This makes the technique compatible with photoresist liftoff processing for junction pattern definition.
6. The deposition technique should allow clean and controlled deposition of thin overlayers for artificial tunnel barriers and thin underlayers for controlling the crystallographic phase of thick overlayers.

3.1 Base Electrode Material

For superconducting devices and quasiparticle mixers in particular, the proper choice of a base electrode material is crucial. As discussed in detail by Beasley, (1980), the soft superconducting elements such as Pb, Sn, and In do not survive repeated thermal cycling because of stress induced hillock formation. These hillocks (micron size protrusions from the film surface) rupture the thin tunnel oxide and short the junction. Soft alloys such as Pb-In-Au and Pb-Bi are an improvement over the single elements and have been developed extensively at IBM for Josephson computer technology [Huang, 1980]. These materials show improved thermal cyclability but still have stress induced failures after many cycles. Pb-In-Au tunnel junctions also show a considerable amount of leakage current below the sum gap and a broad current rise at the sum gap. As discussed by Lahiri (1980), this is due to the presence of low T_c second-phase particles near the barrier. The refractory high T_c A-15 alloys such as Nb_3Sn also have a broad current rise at the sum gap and require a heated ($\approx$1100K) substrate for high quality material growth. Although a broad current rise is acceptable for many digital applications it must be kept to a minimum for SIS mixer

applications. In addition, the A-15 alloys have a very short superconducting coherence length, $\xi \approx 50$Å, which makes their tunnel junction characteristics very susceptible to surface damage and non-stoichiometry at the interface. Furthermore, when the base electrode is a compound or an alloy, thermal oxidation of its top surface to form a tunnel barrier may result in preferential oxidation of one of the elements. This process produces an altered composition in the layer just beneath the oxide and poor tunnel junction characteristics.

The refractory superconducting elements such as Nb and Ta, even with a Pb or Pb-alloy counter electrode, are very attractive materials because of their mechanical ruggedness and relatively high T_c (T_c=9.2K for Nb and 4.4K for Ta). Because these superconductors are single elements, inhomogeneity and spatial variation of the energy gap and T_c with composition are not a problem. It should therefore be possible to make junctions with very "sharp" current increases at the sum gap using these base electrode materials. As discussed below and in chapter V, however, it is not easy to make high quality Nb based junctions. This is because Nb reacts strongly with oxygen to produce conducting suboxides at the interface. These suboxides can locally perturb the superconductivity and degrade the tunneling characteristics [Raider, 1985]. This problem can be partially overcome by the use of artificial barriers of Al_2O_3, Ta_2O_5, and amorphous Si which reduce the formation of Nb suboxides and form good tunnel barriers [see chapter V]. Despite this difficulty, Nb junctions have been studied extensively by many groups [Raider, 1985] which provides a large base of technical information for our studies.

Ta is similar to Nb in many respects except that it produces a very high quality native oxide, Ta_2O_5, tunnel barrier and nearly ideal tunneling characteristics [Shen, 1972]. Because of its lower T_c, there have been relatively few studies of Ta junctions compared to those of Nb junctions.

For mixer operation below 2K, however, the T_c of Ta is certainly acceptable. Most previous studies of Ta have been directed towards understanding the microscopic material properties such as the electron phonon coupling [Shen, 1972; Keith and Leslie, 1978]. Because large area, low-current-density junctions are the best for those scientific studies, high current density Ta junctions have not been previously investigated. The work described in this thesis was motivated by these initial studies and extends the high quality tunneling results into the high current density (J_C > 1000 A/cm^2) regime, as required for electronic applications.

3.2 Tunnel Barrier Materials

The formation of a good tunnel barrier is probably the single most important and least well understood step in making a high quality tunnel junction. The problem is difficult because the barrier is usually so thin (<20Å) that its properties are largely dominated by the defect and interface properties. The mechanisms of subgap leakage and 1/f noise that originate in the barrier itself are presently under intense investigation and are not yet fully understood [Rogers, 1985; Halbritter, 1985; Bending, 1985]. A number of the most important techniques for barrier formation are discussed below along with their relative advantages. At least one example of each technique has been tried in making the junctions described in this thesis.

3.2.1 Thermally Oxidized Tunnel Barriers

Thermally oxidized tunnel barriers for low current density junctions are the most common and generally are the easiest to fabricate. This is because a number of metals of interest such as Al, Sn, Pb, In and Ta form insulating oxides on their surface by simple exposure to air. This was the type of barrier used by Giaever in the original discovery of superconducting tunneling [Giaever, 1960]. Several models for the growth of oxide films

exist and have been recently reviewed by Atkinson, (1985). These models mostly treat the kinetics of ion and electron transport during the growth process and have very little to say about barrier heights or defects in the oxide or at the oxide interface except that these defects exist. Since the barrier height and defects have a large effect on the barrier transport properties, these theories are of limited quantitative use for tunnel junctions. In addition, the details of the oxidation environment such as the presence of humidity, impurities and grain boundaries can have a large effect on the tunnel oxide growth and electrical transport properties. These effects can also be different from one material to another. Clearly, more research in this area is required before these systems can be understood quantitatively. Because of the complicated nature of the problem, most oxide tunnel barrier formation is performed based on experimental knowledge and experience.

The main advantage of thermal oxidation is that it is quite simple to perform and generally gives reproducible results for low current density junctions if such environmental factors as the humidity can be controlled. Unfortunately, it is not applicable to a wide range of materials (i.e. metals that do not oxidize well) and, as we shall see in chapter V, is not easily extended to high current density junctions which have thin oxides.

3.2.2 Plasma Oxidized Tunnel Barriers

Plasma oxidation is defined here to be any ion assisted oxidation process where energetic ions are important. This definition includes ion beam oxidation [Kleinsasser, 1980], rf plasma oxidation [Greiner, 1971], and dc glow discharge oxidation (see chapter IV). The general operating principles of these processes have been discussed by Chapman [1980]. This type of oxidation is widely used by many groups making high current density tunnel junctions for superconducting device applications [Huang,

1980; Broom, 1980; Kleinsasser, 1981] and was developed extensively at IBM for Josephson Computer Technology. It is generally found that these plasma processes are better suited to the formation of uniform high current density oxides. This result is believed to be due to the reduced influence of impurities and surface defects on oxide growth in the presence of energetic (> 10 eV) ion bombardment. In the case of the Ta junctions described in chapter IV and V, we find a similar benefit for plasma oxidation. One possible shortcoming of the plasma oxidation technique is the generally unknown effect of sputtering and oxidation of nearby materials such as photoresist and SiO insulation layers.

3.2.3 Artificial Barriers - Oxidized Metal Overlayers

Artificial barriers are generally defined to be barriers other than the native oxide of the metal of interest. One very useful technique in this regard is the use of oxidized metal overlayer (OMO) barriers. These techniques have been recently well reviewed by Gurvitch and Kwo (1984). The basic idea is to deposit a thin layer of a metal such as aluminum which forms a good native oxide on a material which has a poor native oxide barrier such as niobium. This technique is now widely used for making high quality junctions with niobium base and counter electrodes [Huggins, 1985; Morohashi, 1985]. This technique has only proven itself in the last few years and was not developed earlier because it was widely believed that thin (<100Å) metal overlayers would not be continuous and pin hole free. It turns out, however, that Al "wets" Nb very well which is one reason why this technique works so well (see Fig. 5-21).

3.2.4 Artificial Barriers - Directly Deposited

Deposited artificial barriers such as amorphous silicon [Smith, 1983; and Rudman, 1980], MgO [Shoji, 1987], and Al_2O_3 [Moodera, 1982; Barner,

1987] have recently demonstrated the ability to produce very good tunnel junctions although not as good as the best OMO junctions. The junction resistance was shown to be exponentially dependent on the deposited barrier thickness (as expected for tunneling) by Smith, (1983) and Shoji, (1987). This demonstrates the reproducibility of these processes. A possible disadvantage of deposited barriers is that for high current density applications the average deposited thickness must be very accurately controlled to less than one Å.

3.3 Counter Electrode Materials

The Pb alloys such as PbBi and PbAuIn are desirable counter electrode materials because they do not react with the tunnel barrier when they are deposited. In addition, they generally have a long coherence length (ξ > 500 Å) so that any damage or disorder that exists at the surface does not strongly perturb the energy gap measured by tunneling. Pure Pb counter electrodes are not used because they suffer from a variation of the energy gap due to anisotropy effects (see section 5.5.5) which causes a width to the current rise at the sum gap. The thermal cycling problems observed for Pb alloy base electrodes are not a problem for Pb alloy counter electrodes on refractory base electrodes as demonstrated by the IBM group [Broom, 1980]. These authors found a failure probability of less than $2x10^{-8}$ failures/junction/thermal cycle with PbAuIn counter electrodes on Nb base electrodes.

For SIS mixers, PbBi is preferred over PbAuIn because it is a single phase material for a wide range of compositions and has a sharp gap at low temperatures (see section 5.5.6). There are two compositions of PbBi that are commonly used for tunnel junctions (10% Bi (fcc, α phase) or 29% Bi (hcp, ϵ phase)) as shown in the phase diagram in Fig. 3-1. Since Pb and Bi have nearly the same atomic number, weight % and atomic % are approxi-

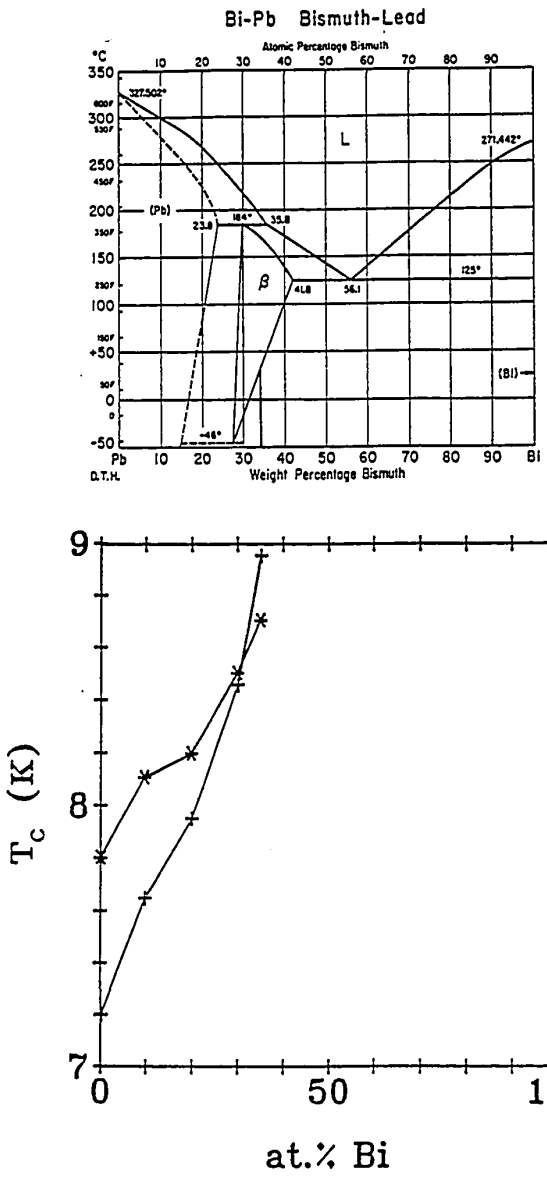

Fig. 3-1: (a) Phase diagram [Metals Handbook, 1982] of PbBi modified to include the recent work of Murakami, 1983, (b) Variation of the superconducting energy gap Δ and transition temperature T_c for the PbBi system [from Dynes and Rowell, 1975].

mately equivalent. The 29% Bi (hcp) ϵ phase has the advantage that the hcp crystal structure can support more elastic strain without dislocation glide than the 10% (fcc) α structure [Murakami, 1983]. The disadvantage of the 29% (hcp) phase is that it exists as a single phase material only for a narrow range of compositions (27.5% to 31.5% Bi [Murakami, 1983]). Murakami, (1983), also found that the composition of the PbBi film could differ significantly from that of the source if the evaporation rate (i.e. source temperature) was not accurately controlled. In addition, we found that a cold ($\approx$77K) substrate was required to get smooth continuous films. The 10% (fcc) phase, however, exists as a single phase material over a wider composition range (0 to 17%) and also forms continuous films on room temperature substrates. All of the PbBi films for the high quality small Ta/PbBi junctions in chapter V used the 10% Bi phase and showed no thermal cycling problems. In the long run, a refractory counter electrode is probably desireable and a great deal of progress has been made in this regard by other groups [Raider, 1985].

3.4 Ion Beam Sputter Deposition Technique

The use of ion beams in thin film technology has recently received a great deal of attention and has been reviewed by Harper, (1982). Some of the major new developments include the application of ion beams for oxidation, for improved thin film step coverage, and for modification of Nb film stress [Cuomo, 1982]. Controlled ion bombardment during thin film growth may also assist in the formation of metastable phases in some materials. Ion-beam sputter deposition, as shown in Fig. 3-2, is a relatively recent development in thin film deposition and has been explored by several workers [Kane 1979, Bouchier 1978, Schmidt 1973 and 1972]. The work described in this section represents a significant advance in the use of this technique for the deposition of high quality refractory metal films.

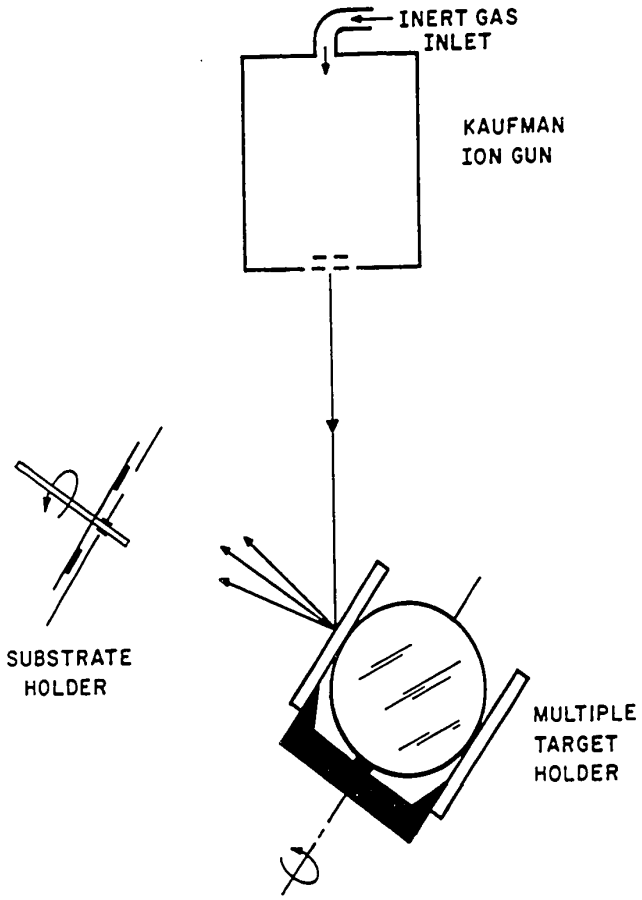

Fig. 3-2: Schematic of the ion beam deposition system (dimensions given in the text). A shutter (not shown) is located between the target and the substrate holder.

Our progress has been facilitated by the recent development of high current density broad-beam ion sources. The most important of these sources, the Kaufman ion source, was originally invented by H.R. Kaufman as an ion thruster for space propulsion. Since the detailed operation of these sources has been reviewed by Kaufman [1982], only the basics of the operation are outlined in this section. The ion source used in this work for deposition was manufactured by Ion Tech, Inc.[1] and is shown schematically in Fig. 3-3. The operation of the source involves the input of a sputtering gas such as Xe or Ar into the discharge chamber where plasma is maintained by a discharge voltage (20-50 volts) and source of electrons provided by the cathode filament. The ions are extracted by the voltage between the screen and accelerator grid and directed at the target. The accelerator grid is always kept at a negative voltage (relative to ground) to prevent the backstreaming of electrons into the source which is at a large positive potential. In our source, the grids are made of graphite (which has a very low sputter yield) in order to minimize the erosion of the grids due to sputtering.

We have used the ion-beam sputtering technique because it offers a number of unique advantages for the deposition of high melting point materials such as Nb and Ta. These advantages include the relative absence of radiant heat and the physical separation of the deposition substrate from the plasma and high energy particles of the sputtering process. These characteristics are also favorable for photoresist lift-off processing which has been used in SIS tunnel junction fabrication described in chapter IV.

The deposition of high quality superconducting films of Nb and Ta has also been explored by other workers using the techniques of e-beam evaporation [Broom 1980, Alessandrini 1981, Neal 1977, Westwood 1975],

---

[1] Ion Tech, Inc., Fort Collins, CO 80522

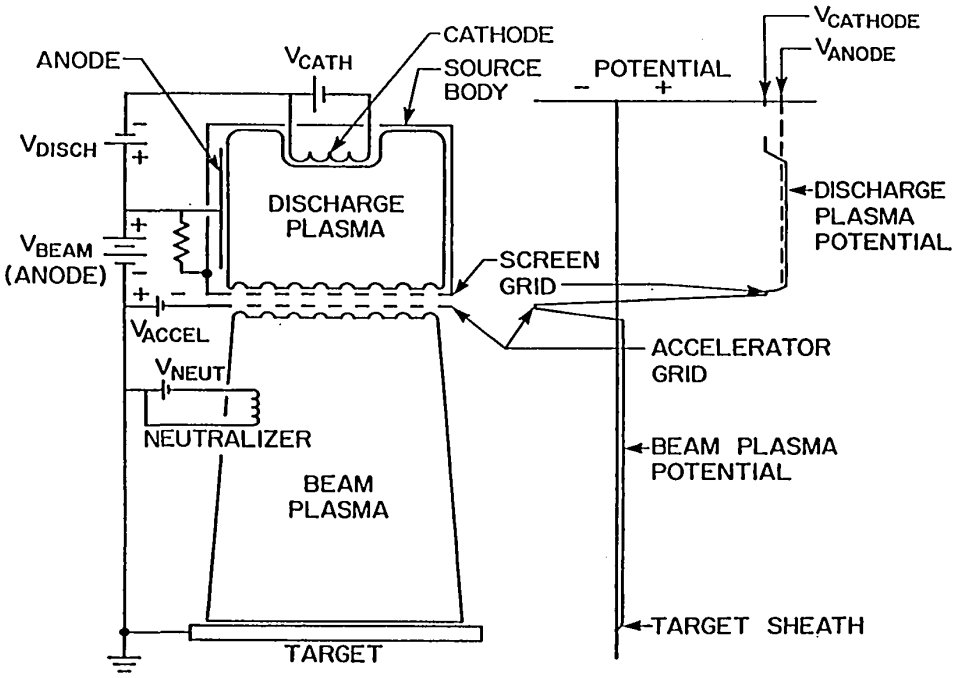

Fig. 3-3: Diagram of the operation of the Kaufmann ion source showing the bias voltages and the potential distribution along the path of the ion beam (from Kleinsasser, 1982).

planar sputtering [Westwood 1975, Wolf 1976, Heim 1975], and magnetron sputtering [Wu 1979, Huggins 1983]. Typically, very high quality vacuum systems ($P<10^{-7}$ Torr) and high deposition rates ($R>10$ Å/sec) are required. A heated substrate is also often required to achieve high quality films. These rather stringent requirements are due to the tendency of Nb and Ta to react strongly with residual vacuum system impurities such as water vapor and oxygen. As discussed below, we have found that these requirements are relaxed to some extent for ion-beam deposition.

3.4.1 Ion Beam Deposition System

The ion beam sputtering system used in this work is shown schematically in Fig. 3-2. Typical operating conditions with xenon (≥99.99% pure) or argon (≥99.999% pure) gas ranged from 900 to 1500 eV beam energy and from 25 to 100 mA beam current. The items shown in Fig. 3-2 are mechanically mounted on 1.9 cm thick metal top and bottom plates for a 46 cm diameter x 53 cm high Pyrex glass cylinder. This system is pumped by a standard 15 cm diffusion pump with a liquid nitrogen cold trap[2]. In addition, we have constructed a liquid nitrogen cooled copper liner which fits just inside the Pyrex glass cylinder and provides additional trapping for water vapor and other impurities. This cold shield reduces the ultimate chamber pressure from 6×10^{-7} to 3×10^{-7} torr, the main contaminant being water vapor.

The target holder shown in Fig. 3-2 can be used to rotate any one of four different water-cooled targets (Nb, Ta, Al, Si, etc.) under the beam. We use 10 cm diameter Nb and Ta (99.9+% purity) targets, the centers of which are ≈15 cm from the ion source when sputtering. The water cooling

---

[2]Varian Model 3118 - Varian, Palo Alto Vacuum Division, Palo Alto, California 94303

keeps the temperature rise of the target to less than 20 °C during sputtering.

The substrate holder is capable of separately exposing eight sets of substrates for optimization of the deposition conditions. During a typical deposition, the substrate temperature remains below 70 °C. We have employed 6.35 x 6.35 mm Si(100), Si(111), and microscope cover glass substrates with no distinguishable difference in deposited film properties. Substrates were cleaned ultrasonically in solvents and blown dry with nitrogen gas. The stability of the ion beam characteristics during a deposition was always quite good (variations ≤ 3%). An initial predeposition sputter period of typically 60 min was always performed to allow the source to equilibrate and to provide a layer of freshly sputtered Nb or Ta on the LN_2 cold shield. This sputtered layer acts as a good getter for impurities in the vacuum system and should reduce our effective base pressure below that measured before deposition. This is difficult to determine exactly with our residual gas analyzer because of the large background of Xe gas in the system during sputtering.

3.4.2 Ion Beam Parameters

The initial studies of ion beam deposition were made with argon gas. However, the subsequent use of xenon gas, suggested by the work of Schmidt, (1973), was found to produce our highest quality films. Using Nb as a test material, the optimum beam conditions for each gas were obtained. The ion beam was run without a neutralizer since an initial study of its use showed no beneficial effects. Grounding or applying an electrical bias of up to ± 100 V to the substrates also produced no noticeable improvements. As a result, most substrates were electrically floating with a positive self-bias of about 10 V.

The optimum beam parameters were judged to be those that produced the highest T_c Nb films. For Ar gas, the optimum beam conditions were 1300 V beam voltage and 57 mA beam current at a chamber pressure of $\simeq 1.0 \times 10^{-4}$ Torr (as measured with an ion gauge in the base plate). These conditions produced a deposition rate of 2.2 Å/sec and a T_c of 8.3K. For Xe gas, the optimum beam conditions were 1500 eV and 35 mA at a chamber pressure of $\simeq 1.7 \times 10^{-4}$ Torr, producing a deposition rate of 2.4 Å/sec and a T_c of 9.1K. Deposition rates in these optimization studies for Nb films ranged from 1 to 5 Å/sec and were directly proportional to ion beam power (current x voltage). The sputtering yield for Xe gas was found to be $\simeq$ 50% higher than for Ar gas. The T_c values for various deposited Nb films revealed a fairly broad maximum with respect to variations in ion beam power. In general, a 25% change from the optimum values of ion beam current or voltage given above produced a $\simeq$0.3K drop in T_c. In addition, fine tuning of the internal ion source voltages and inert gas pressure has shown that a minimization of the accelerator grid current to $\leq$ 3mA and the plasma discharge voltage to $\leq$ 30 V produced the highest T_c niobium films at a given beam power. Xe was found to allow the lowest values of discharge voltages (<20 V) due to its large ionization cross section. This minimization suggests that excessive internal currents or voltages may give rise to beam contamination due to sputtering of the internal ion source structures and explains the lower T_c of films deposited with Ar.

For a given sputter gas, the observed decrease in T_c with respect to decrease in beam power (deposition rate) from the optimum value is probably due to an increased incorporation of adsorbed vacuum system impurities in the growing film. The decrease in T_c at higher rates is probably due either to increased sputtering inside of the ion source, or to

increased particle bombardment of the growing film, which could cause film damage [Cuomo, 1982; Heim and Kay, 1975].

3.5 Properties of Ion Beam Deposited Films - Transport and Structure

The properties of a large number (n>100) of ion beam deposited Nb and Ta films have been measured in the process of optimizing the new ion beam deposition technique. As a result, a number of universal trends have been observed as a function of the sample resistivity. These trends have been compared to Nb films and bulk Nb prepared by other techniques and are discussed below.

3.5.1 Measurement Techniques

The low temperature cryostat and electronics are described in detail in chapter V. Resistivity measurements were made using the four-point technique due to van der Pauw, (1957). Results for ρ should be independent of sample shape with this technique. The accuracy of the van der Pauw technique was verified experimentally (± 1%) with a large piece of aluminum foil and various probe placements. These measurements also revealed that exact placement of the probes at the edge of the film is not critical. In fact, moving all of the probes in from the edge by 20% of the width of a square sample only caused a 5% error. Temperature measurement was made with a germanium resistance thermometer or a calibrated Allen-Bradley 220 Ω carbon resistor. The transition temperatures of high purity bulk Pb and Nb samples have been measured to be within 0.1K of their published values [Kerchner, 1981]. Detection of the superconducting transition was made both resistively and inductively by an ac susceptibility measurement at ≈2 MHz [see B.J. Dalrymple, 1983]. Film thickness was

measured (± 100Å) by an optical interference technique[3]. Most films whose properties are reported on below were thick (d ≥ 1500 Å) to avoid the depression of T_c found in very thin films [Wolf, 1976].

Electron diffraction, transmission electron microscopy (TEM), and scanning transmission electron microscopy (STEM) were all performed on a JEOL 100CX TEMSCAN. Samples were prepared by depositing 300 to 400 Å of Nb or Ta onto a 300 Å carbon film which was suspended on a standard 200 mesh copper TEM grid. Energy dispersive x-ray analysis was also used to look for incorporated xenon or argon. X-ray diffraction measurements were made using a standard x-ray diffractometer with a Cu K_α x-ray source. Positions of the Nb and Ta peaks on the diffractometer traces were referenced to the silicon substrate peaks or a silicon powder standard, allowing an absolute accuracy of ±0.05°.

3.5.2 Niobium Films

The measurements of Nb films are more extensive than those of Ta films. We have studied over 100 Nb films. The films were always observed to adhere very well to clean Si or glass substrates. The wrinkled appearance of the few films deposited on dirty substrates indicates that our films are under compressive stress, in agreement with work on low pressure magnetron-sputtered Nb films [Wu, 1979] and the model of compressive stress discussed below. The electrical measurements of representative Nb films are presented in Fig. 3-4 and Table 3-1. The data in these figures represent the properties of films deposited under a wide variety of beam conditions during the optimization procedure discussed above. The important feature to notice in Fig. 3-4 is the consistent behavior of the ion-beam deposited films with respect to changes in deposition conditions. The

---

[3] Model M-100 - Sloan Instruments Corp., Santa Barbara, CA

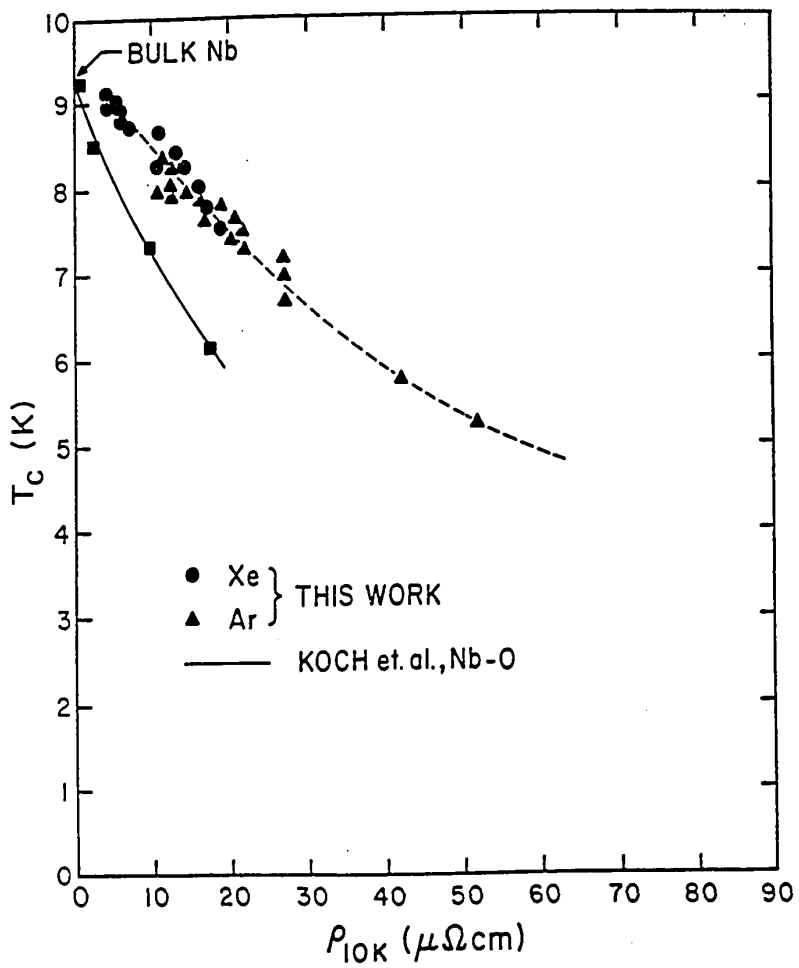

Fig. 3-4: Superconducting transition temperature T_c of ion beam deposited Nb films vs low temperature (10K) resistivity. Film thickness ranged from 1000 to 3000 Å. Other data is from Koch, 1974.

TABLE 3-1 Representative Nb and Ta film properties.

Film #	Sputtering gas	Film thickness[a] Nb (Å)	Ta (Å)	bcc lattice constant (Å)	ρ_{10K} ($\mu\Omega$-cm)	RRR[c]	T_c (K)
Bulk Nb				3.301	___	___	9.3
25-2	Xe	2500	0	3.335	4.0	3.86	9.1[b]
28-3	Xe	2000	0	3.335	5.2	3.56	8.9
26-1	Xe	2500	0	3.343	7.3	2.88	8.7
24-7	Xe	2700	0	3.367	13.5	2.00	8.4
24-4	Xe	2300	0	3.367	18.8	1.63	7.5
112-6	Ar	1900	0	3.353	11.5	2.00	8.3[b]
18-6	Ar	1900	0	3.362	21.4	1.64	7.6
19-1	Ar	2200	0	3.380	27.3	1.43	6.7
18-3	Ar	1800	0	3.405	43.8	1.28	5.8
15-1	Ar	1600	0	_____	53.4	1.24	5.3
Bulk Ta				3.303	___	___	4.4
210-8	Xe	600	2400	_____	5.2	5.32	7.9
28-1	Xe	300	2400	_____	6.2	3.35	6.6
210-5	Xe	70	2400	3.328	5.6	3.25	4.5
210-4	Xe	30	2400	3.324	6.1	3.23	4.3
210-2	Xe	10	2400	3.324	5.5	3.75	4.3
210-1	Xe	3	2400	3.324	7.2	3.45	4.2
28-8	Xe	0	2400	β-Ta	151	0.95	___

(a) Ta films were deposited on Nb to nucleate bcc Ta (see Text).
(b) Optimum values for the sputtering gas used.
(c) RRR is the residual resistance ratio - the ratio of the room temperature resistivity to the low (10K) resistivity.

decrease in T_c from ≈9.1K at a rate of ≈0.1K/$\mu\Omega$-cm appears to be universal for our films and represents a rate that is less than that for bulk niobium-oxygen solid solutions (≈0.18K/$\mu\Omega$-cm [Koch, 1974]). In general, the analysis of mechanisms causing the depression of T_c in Nb films is a complicated issue. In past work, it was found that the competing factors of lattice dilation, lattice damage, and inert or reactive gas incorporation all have a strong effect on T_c in Nb films [Heim, 1975].

It is important to note that with the optimum beam conditions given above we have reproducibly prepared Nb films with a $T_c \geq 9.0$K and a transition width of ≤ 0.03K. To our knowledge, this is the first report of T_c values this high for Nb films deposited without the use of high rates (> 10 Å/sec), heated substrates, or a very high vacuum environment ($P < 10^{-7}$ Torr). Because on the use of room temperature substrates, these Nb films were also easily patterned using standard photoresist liftoff techniques.

Structural data obtained from TEM and x-ray diffraction studies showed that the Nb films were bcc polycrystalline and had a grain size of ≈150 Å. The TEM micrographs and x-ray diffraction scans are nearly identical to those for bcc Ta in Figs. 3-6a and 3-7a which are discussed in the next section. No significant change in T_c with grain size was observed. TEM diffraction patterns showed no preferred orientation of grains with respect to rotations in the plane of the substrate. X-ray diffractometer scans, however, indicated a strong preference for the (110) lattice planes to be parallel to the substrate. This (110) texturing was found for all substrates. A plot of T_c versus lattice constant a_o, as determined by the position of the (110) lattice reflection, is given in Fig. 3-5 and is compared with previous work on bulk Nb [Koch, 1974]. Note that our x-ray diffraction technique only gives us the spacing between planes of atoms that are parallel to the substrate. The data in Fig. 3-4 suggest that a mechanism other than oxygen incorporation, possibly inert gas incorporation or film

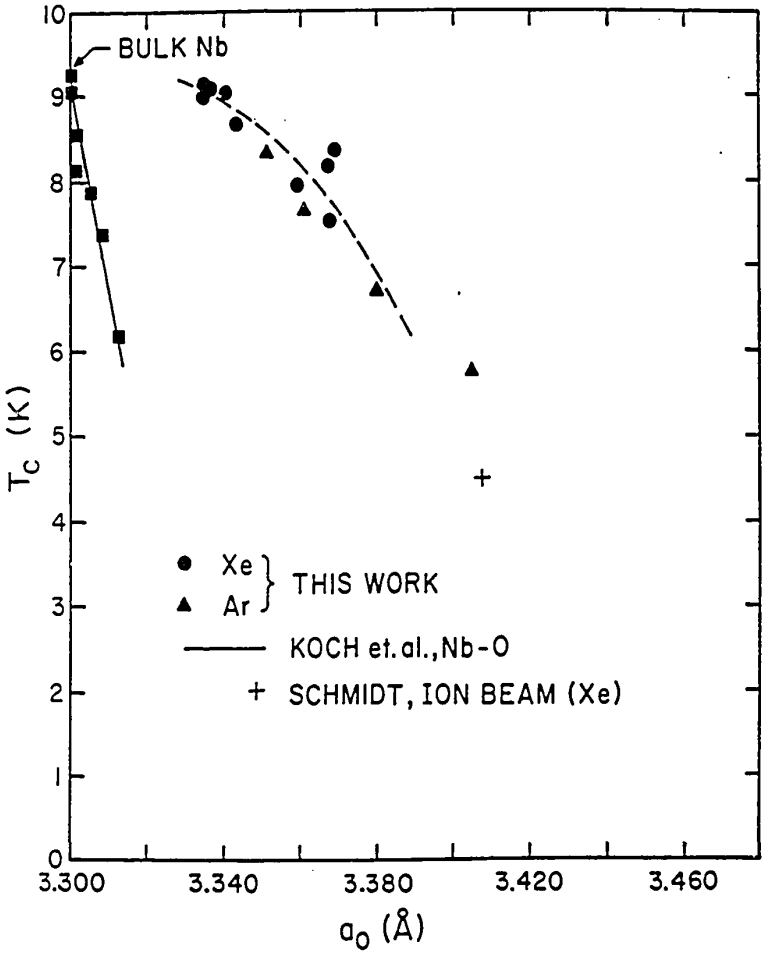

Fig. 3-5: Superconducting transition temperature T_c of ion beam deposited Nb films vs crystal lattice constant a_o. Data from this work is given in Table 3-1. Other data is from Schmidt, 1974 and Koch, 1974.

stress [McWhan, 1983] may be expanding the lattice constant of our ion beam deposited films. We have made on estimate of the amount of compressive stress in our films by performing a simple bulk calculation. This simple calculation assumes that compressive stress in the X-Y plane will cause an expansion of the crystalline lattice plane spacing in the Z direction (i.e. the unit cell will be distorted from bcc to body centered tetragonal (bct)). The ratio of the strain in the Z direction ($\delta Z/Z$) to the strain in the X or Y direction ($\delta L/L$) is given by the Poisson ratio,

$$(\delta Z/Z)/(\delta L/L) = \nu \qquad 3\text{-}1$$

where the stress is related to the strain through the Young's modulus,

$$(\delta L/L)/F = Y. \qquad 3\text{-}2$$

For Nb, $Y \simeq 1x10^{-12}$ dynes^{-1}cm^2 and $\nu = 0.38$ and the observed $\delta Z/Z$ from a_o in Table 3-1 is ((3.335Å - 3.301Å)/3.301Å) which gives a compressive stress of $\simeq 1.6x10^{10}$ dynes/cm^2. A similar calculation for Ta with $\nu = 0.35$, $Y = 1.86x10^{12}$ dynes^{-1} gives a compressive stress of $1.7x10^{10}$ dynes/cm^2. The absence of any detectable levels of xenon or argon by energy dispersive x-ray analysis indicates that the concentrations of Xe of Ar must be less than ≃0.5 at.%.. In addition, a SIMS analysis of our best films reveals that oxygen and carbon impurity concentrations are < 0.1 at.%.

Previous work on inert gas ion-beam sputter deposition of refractory superconducting films has demonstrated clear trends as a function of sputtering gas and crystal lattice expansion [Schmidt, 1973]. Properties of those films, however, differed significantly from the bulk material. More recently, ion-beam-deposited Nb-Ti films with properties reported to approach those of the bulk material have been produced on a heated

substrate with a high energy duoplasmatron-type ion source [Bouchier et al., 1978].

3.5.3 Tantalum Films

All investigations of Ta film deposition were performed with a xenon ion beam using the beam conditions which we found to be optimum for Nb. These conditions produced a Ta deposition rate of 2.7 Å/sec. It was found that on room temperature glass or silicon substrates, we always produced high resistivity (150-200 $\mu\Omega$-cm) films characteristic of the well known β phase of Ta [Read, 1965; Moseley, 1973; Heiber, 1982; Read, 1973; Feinstein, 1973; Westwood, 1975]. This is consistent with previous work [Kane, 1979; Schmidt, 1972] on ion beam deposited films. We note that in all of the previous work where bcc Ta films were obtained, a heated substrate or a special substrate material such as gold was required to obtain the bcc phase. The residual resistance ratio (ρ_{298K}/ρ_{10K} = RRR) is always less than but close to one for the β-Ta films. The TEM micrograph in Fig. 3-6b and the x-ray diffractometer scan in Fig. 3-7b confirm the existence of the β-Ta tetragonal crystal structure and a strong degree of (100) texturing. Although there can be difficulties in interpreting diffractometer scans without the use of off-axis information [Read, 1972], our data do suggest that little or no Ta in the bcc phase exists in our β-Ta films. The β-Ta films did not become superconducting above 1.5K, which is consistent with the published T_c of 0.5K [Read, 1965] for the β-Ta phase.

In order to promote the formation of Ta in the bcc phase (bulk T_c = 4.4K) we have ion beam deposited a layer of Nb onto the Si substrates just before depositing the Ta. This was accomplished by depositing a layer of Nb 3 to 600 Å thick and then immediately (within ≈1s) rotating the target holder to the Ta position without turning off the beam or closing the shutter. Nb underlayers of 3 and 10Å caused a dramatic decrease in the

Fig. 3-6: (a) Transmission electron micrograph and diffraction pattern for a 300 Å Ta film on a 30 Å Nb underlayer to nucleate the bcc crystal structure. (b) Same as (a) but without the 30 Å Nb underlayer. This film has the β-Ta (tetragonal) crystal structure. (both (a) and (b) were deposited on a 200 Å carbon film on a standard 200 mesh TEM grid.

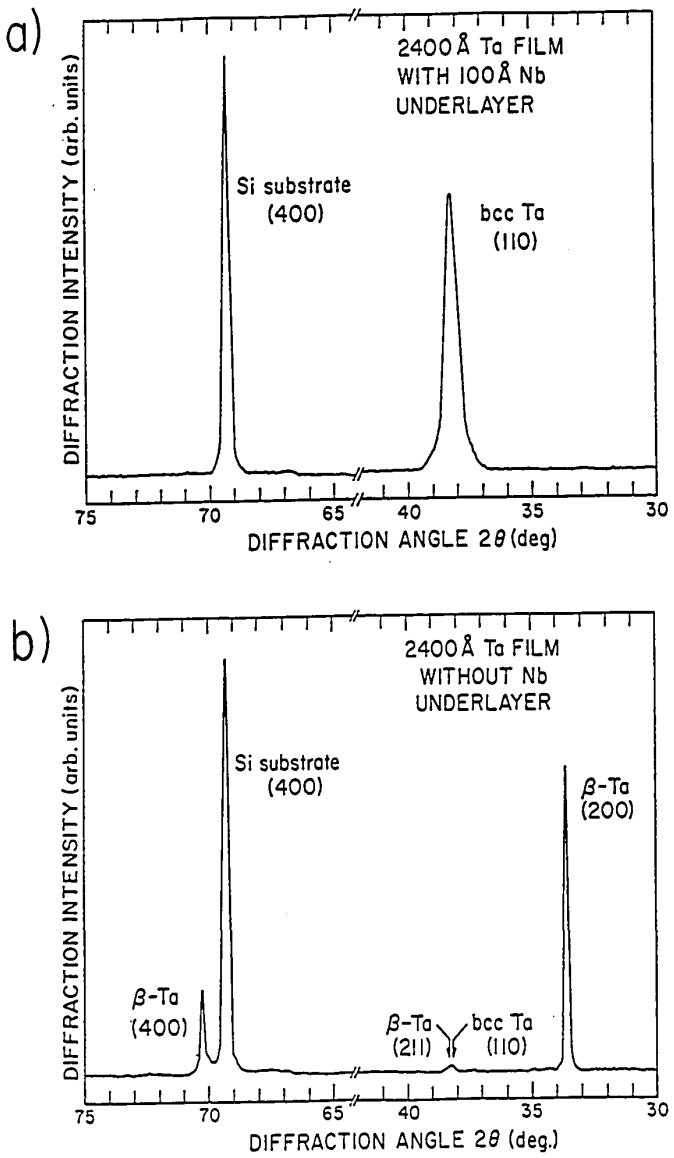

Fig. 3-7: X-ray diffractometer scan of a 2400 Å Ta film on a 100 Å Nb underlayer used to nucleate the bcc structure. (compare TEM in Fig. 3-6a). (b) Same as (a) but without the Nb underlayer. This film has the β-Ta (tetragonal) crystal structure. (Compare TEM in Fig. 3-6b).

amount of β-Ta, by a factor of more than 100. Ta films on underlayers thicker than 10Å showed no detectable amount of β-Ta as shown in Fig. 3-6a for a 30Å Nb underlayer and Fig. 3-7a for a 100Å Nb underlayer. Nb underlayers of all thicknesses produced a large increase in the amount of bcc Ta as inferred from T_c, low temperature resistivity, and x-ray diffractometer scans. X-ray data in Fig. 3-7a also show a strong degree of (110) texturing. The Ta film data are summarized in Table 3-1. Consistent with the proximity effect theory [Deutscher, 1969], Ta films on Nb underlayers with thicknesses > $\xi(0) \simeq 100$Å [Ruggiero, 1982] appear to have enhanced values of T_c.

The strong influence of the substrate on the nucleation of β-Ta has been previously observed by other workers [Heiber, 1982; Feinstein, 1973]. Our findings suggest that the thin Nb underlayer is modifying the substrate surface to provide a surface that favors the formation of the bcc phase of Ta. These findings are consistent with the hypothesis of Feinstein, (1973), that the presence of O or OH, formed by the reaction of H_2O with the surface oxide favors the nucleation of β-Ta. There may also ba a propensity for bcc Ta growth due to the close lattice match of bcc Ta and Nb shown in Table 3-1. The use of a Nb underlayer is a very convenient way to obtain the bcc phase for our tunnel junctions. In addition, this study shows that thin Ta overlayers on Nb will be bcc and can be used as oxidized metal overlayers for artificial tunnel barriers (see sections 3.2.3 and 5.4.2).

Using the large area tunnel junctions discussed in chapter IV and V, we have measured the temperature dependence of the energy gap for our Ta films. A plot of $\Delta(T)$ is shown in Fig. 3-8 and compared with the BCS exact theory. The deviations from the BCS form are also seen by other workers [Wolf, 1985] and arise because of strong coupling effects which are ignored in the weak coupling BCS theory (see chapter II). Clearly, our ion

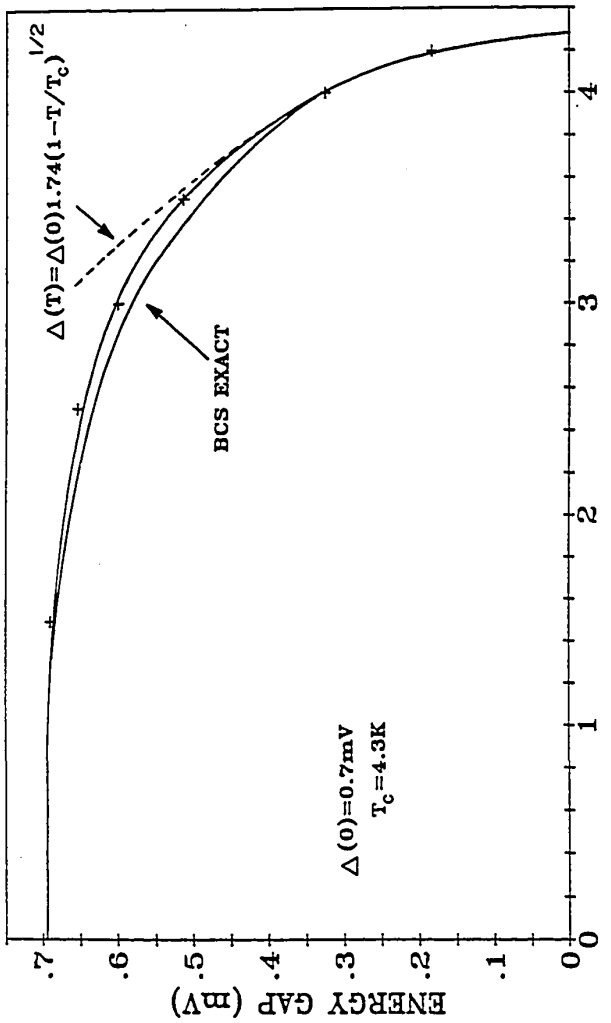

Fig. 3.8: Variation of the superconducting energy gap as a function of temperature showing the deviation from the BCS theory due to strong coupling effects (see text). The lower curve is the exact BCS result and the upper curve is a guide to the eye through the experimental points.

beam deposited Ta films are behaving very much like bulk Ta material and should serve well as a base electrode material for tunnel junctions.

3.6 Conclusions

In summary, we find that the ion beam deposition technique is capable of producing high quality superconducting films of Nb and Ta. While high quality films may be produced by other techniques, ion beam deposition offers some special advantages. Importantly, Nb and Ta films can be produced on room temperature substrates, in the moderate quality vacuum system which is available, and with moderate deposition rates. These ion beam deposited films are compatible with standard photoresist liftoff techniques, which is an important advantage for the tunnel junction fabrication in chapter IV. In addition, the ability to sequentially deposit different materials, using a multiple target holder, is of general utility and is helpful in conveniently obtaining the bulk bcc crystal structure in Ta films. In the next chapter, we have also used the ability to deposit a thin Ta overlayer on a Nb base electrode as an artificial tunnel barrier (OMO) to improve the tunneling characteristics.

IV. JUNCTION FABRICATION

This chapter describes the fabrication techniques for both large area ($\simeq 10^{-4}$ cm^2) and small area ($\simeq 10^{-8}$ cm^2) tunnel junctions. The large area junctions were developed to evaluate the quality of junctions that could be made with the ion-beam deposited Nb and Ta films. Based on the encouraging results from large area junctions, the fabrication of small area junctions was pursued. The purpose of fabricating the small junctions was to produce junctions suitable for SIS mixer experiments (i.e. high current density ($\geq 10^3$ A/cm^2) junctions with a sharp and low leakage I-V's). This involved a number of special considerations such as the use of a low energy ($\simeq$ 150 eV) ion cleaning process to minimize barrier/interface damage. A novel step-defined process was also developed that eliminates photoresist processing between barrier formation and the subsequent metal deposition. This eliminates a potential source of contamination. The reduced number of processing steps was also helpful in minimizing the time required to explore different techniques for tunnel barrier formation. In the end, a dc glow discharge oxidation technique was found to produce extremely high quality junctions with subgap currents approaching the minimum allowed by the BCS theory. The electrical measurement of these junctions is discussed in chapter V.

4.1 Large Area Junction Fabrication

Large area tunnel junctions were fabricated on ion-beam deposited Ta and Nb films that were deposited with the optimum deposition conditions discussed in chapter III. The Ta films were always deposited on a 20 to 100 Å Nb underlayer to nucleate the bcc (superconducting) phase of Ta. Following deposition, the system was brought to atmospheric pressure with dry nitrogen gas and the substrates were exposed to air for varying lengths

of time. Longer oxidation times generally produced higher resistance junctions as described in chapter V. After oxidation, the desired sample was placed in a sample holder with a 75 μm wide wire mask stretched across the film surface. This mask (a 75 μm diam. steel wire) protected a narrow strip on the surface of the film during the subsequent evaporation of a Ge film ($\simeq$ 2000 Å). The Ge serves as an insulator at 1.5K and defines one dimension of the tunnel junction area. The other dimension of the junction was defined by the width of the counter-electrode strip that crosses the base electrode opening in the Ge as shown in Fig. 4-1. The counter-electrode width was defined with a simple mechanical mask with a slot opening (300 μm wide) that runs perpendicular to the opening in the germanium. The counter-electrode (PbBi, Pb, or Sn) was evaporated by resistive heating of a conventional Ta boat to achieve a rate of 20 - 30 Å/sec. After fabrication, the junctions were stored in liquid nitrogen to prevent aging and to protect the junctions from physical or electrical damage.

A few of the large area Ta junctions were prepared with an amorphous Si (a-Si) tunnel barrier to search for any possible advantages of this barrier. This idea was motivated by the successful work on a-Si tunnel barriers at Sperry by Smith et al., (1983) and at Stanford [Rudman, 1980]. The a-Si barrier (50 Å or 70 Å thick) was deposited immediately after the Ta film deposition by simply rotating the Si target under the beam. The rotation from Ta to Si targets typically took about 1 sec. The other process steps discussed above were identical. During the transfer from the ion-beam system to the thermal evaporator the a-Si barrier was exposed to air for ~10 min. This brief air exposure probably formed a thin oxide on the Si surface and may also fill any potential pinholes in the a-Si by oxidizing the exposed Ta surface under the pinhole. The electrical properties of these junctions are discussed in chapter V.

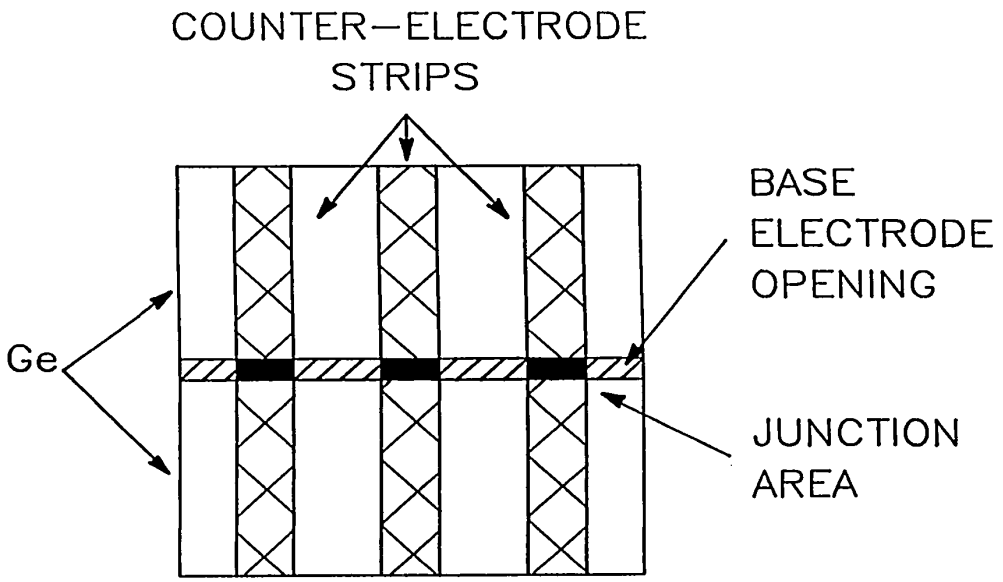

Fig. 4-1 Top view of the large area junction pattern shown for three junctions. The entire base electrode surface (except for the narrow base electrode opening) is covered with Ge which acts as an insulator at 4.2K. The strip opening in the Ge layer is created by wire mask during Ge evaporation. The overall chip size is 1/4 x 1/4 inch.

4.2 Small Area Junction Fabrication - Step Defined Process

The following sections describe the fabrication of small area tunnel junctions for SIS mixer experiments. The first section describes the essential elements of the optimum process (with dc glow discharge oxidation) while the subsequent sections and Appendix A discuss the specific details of important fabrication steps. Other (less successful) tunnel barrier formation techniques that were explored are also discussed. The dc electrical measurements of these junctions are presented in chapter V.

4.2.1 Step Defined Junction Fabrication

The step defined process illustrated in Fig. 4-2 and 4-3 (see also Appendix A) was developed to allow the deposition of the base- and counter-electrode metallizations without the need for photoresist processing between the depositions. The elimination of resist processing between depositions allows the rapid optimization of oxidation conditions and offers the possibility (in future experiments) of complete junction fabrication without breaking vacuum. The process begins by patterning a series of Cr lines 1-2 μm wide by 500 Å thick using standard photolithography on a standard 2 inch diam. Si (100) wafer[1]. These lines are placed end to end on 914 μm (36 mil) centers as illustrated in cross section in Fig. 4-2 and in a top view in Fig. 4-3. The Cr serves as an etch mask during the subsequent reactive ion etching (RIE) which is used to define a 0.7 μm high step in the Si substrate (see Fig. 4-2a). As discussed below (section 4.2.3), we use a mixture of 90% CF_3Br and 10% O_2 as the etch gas for RIE. After RIE, the Cr film was removed with a wet chemical etch[2]. An undercut resist stencil suitable for liftoff is used to define the width of the junction

---

[1] General Diode, Corp., Framingham, MA.

[2] Chromium mask etchant - Transene Co., Rowley, Mass. 01969

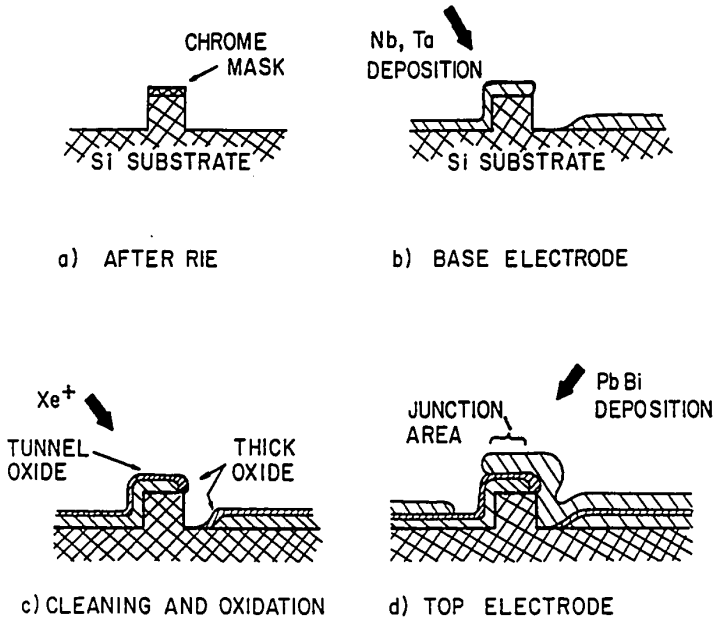

Fig. 4-2 Step-defined fabrication sequence (cross section) showing the importance of the thick oxide for edge protection.

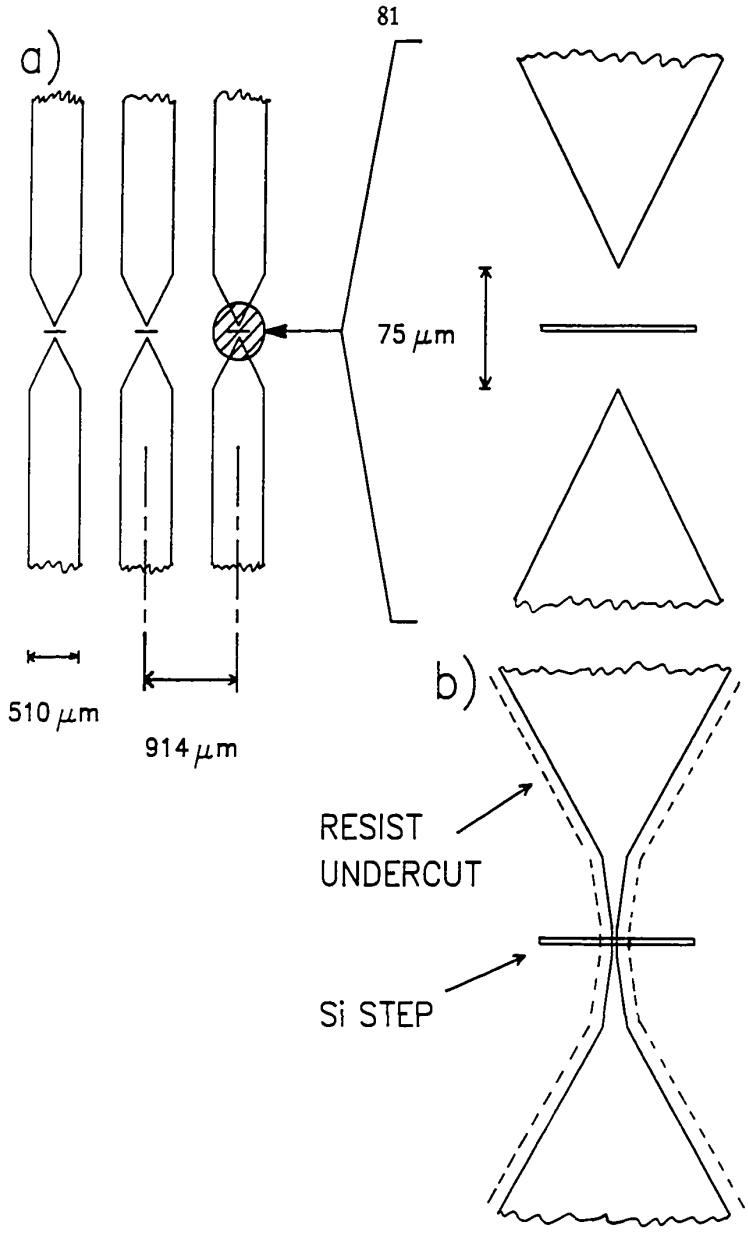

Fig. 4-3 a) Top view of the step defined process (for three junctions) showing the large leads that are patterned to come within 75 μm of the Si step. b) Final pattern projection to open a slot over the Si step for angle deposition as shown in Fig. 4-2. The undercut resist is also indicated.

perpendicular to the plane of Fig. 4-2. This stencil is a three-layer photoresist structure which defines a 1-2 μm slot over the Si step (see section 4.2.2 for details). On each side of the step the slot flares out to form the 500 μm wide leads to the junction as illustrated in Fig. 4-3. After the preparation of this liftoff stencil, the substrate is ready for metal deposition.

The 3000 Å thick Ta base electrode is deposited by ion-beam sputtering at a 45 degree angle, leaving a break in the shadow of the step as shown in Fig. 4-2b. The multiple target capability of our sputtering system allows us to deposit a thin 200 Å Nb underlayer to nucleate the Ta film in the bcc (superconducting) phase without the use of substrate heating. Ta films without the Nb underlayer grow in the non-superconducting β phase as discussed in chapter III. Following the Ta deposition, a thick oxide layer is grown over the entire Ta film by intentional exposure to air for 1-2 hours. The sample is then loaded into a separate vacuum system and pumped to a pressure of $<7\text{x}10^{-7}$ Torr. This system is equipped with a small Kaufman ion source which is used to clean the surface of the Ta film with low energy (160 eV) Xe^+ ions at a current density of $\sim$100 $\mu A/cm^2$ for 3 minutes. The Xe^+ ion beam impinges on the surface from the same angle that the Ta film was originally deposited. As illustrated in Fig. 4-2c, this process leaves a thick oxide layer on the shadowed edges of the film at the break and thus eliminates tunneling into this region. Damaged regions at Ta/Nb/Si interface on the edge of the film may have reduced energy gap values which would contribute to an increased width of the current rise at the sum gap and thus to degraded mixer performance. All photoresist layers which are exposed to the ion-beam during cleaning are covered with a Ta film. This helps to reduce contamination of the junction surface due to photoresist sputtering during cleaning.

After cleaning, the surface is re-oxidized in an oxygen dc glow discharge at a pressure of 125 mTorr for 10 to 30 seconds, depending on the current density desired. For a 20 sec oxidation, we find $J_c \approx 10^3$ A/cm^2. We estimate that the O_2 ion energies at the junction surface are less than 20 eV [Chapman, 1980]. This provides a relatively gentle ion--assisted oxidation process. Without the glow discharge, the oxidation rate with O_2 at this pressure is found to be negligible. As discussed in chapter V, junctions made with this technique have nearly ideal I-V characteristics, even at current densities of 1300 A/cm^2. In addition, the lack of a proximity effect "knee" at the sum gap indicates a well defined insulator to metal interface (see section 5.5.2). Following oxidation, the substrate is rotated and a 3000 Å $Pb_{0.9}Bi_{0.1}$ counter-electrode is evaporated from an alloy source at 50 Å/sec as shown in Fig. 4-2d. Finally, the photoresist stencil is lifted off in acetone. An SEM micrograph of a completed junction is shown in Fig. 4-4.

In some ways, this step-defined process is analogous to the process developed by Dolan (1977); see also Dunkelberger (1978) which employs a suspended photoresist bridge and two depositions from different angles to define the tunnel junction area. A careful examination of the Dolan process, however, reveals that it is not well suited to deposition from broad (non-point-like) sources such as we have with ion-beam deposition. Non-point sources cause a broad slope to the edge of the deposited film in an area that is critical for junction formation in the Dolan process. The thin metal regions associated with this broad slope can contribute to poor tunneling characteristics due to a locally depressed energy gap value. This is not a problem in the step-defined process because the film is abruptly terminated at the step edge and all of the tunnel junction material near the barrier is relatively thick (>1000 Å). In addition, the step process has a more open geometry which allows easier surface cleaning and oxidation.

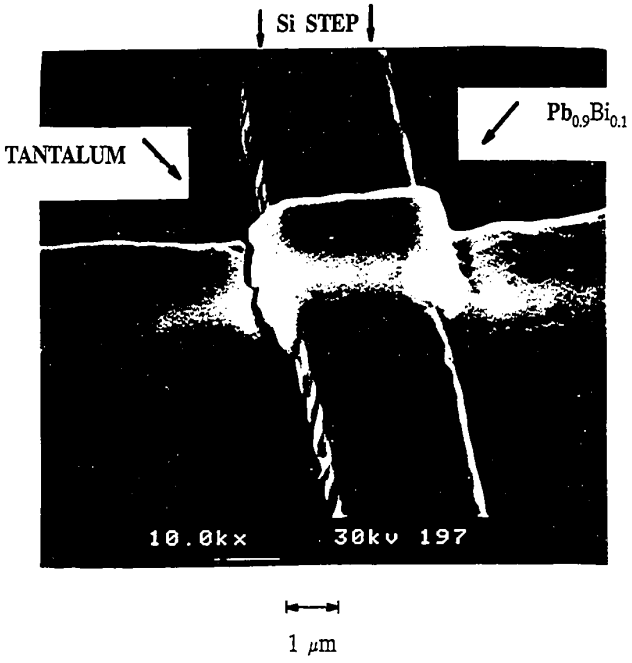

Fig. 4-4 SEM micrograph of a completed junction from the step-defined process. Deposition directions are shown.

4.2.2 Photolithography

The ~ 1 μm Cr lines for masking the tops of the steps during RIE in Fig. 4-2a were patterned by liftoff with a single layer of AZ-1350B photoresist[3]. This resist was patterned by contact printing with a Cr mask that had the desired line pattern. The detailed photoresist processing parameters are standard and given in Appendix A. The Cr mask was made by projection lithography with a Zeiss microscope [Feuer, 1980; Wisnieff, 1986] and subtractive etching on a standard 2.5 inch glass plate.

The tri-layer resist used for defining the junction area and leads consists of an exposed 1.5 μm thick bottom layer of AZ1350J, a 500 Å Al isolation layer, and a 1.0 μm top layer of AZ1370 photoresist. Attempts to use a thinner top layer of AZ1350B resist (for improved resolution) often resulted in a collapsed photoresist edge instead of an undercut. The processing parameters are given in Appendix A. In this resist structure, the top layer is intended for high resolution pattern exposure, while the bottom layer provides an undercut resist profile. The undercut profile allows relatively thick (~ 5000 Å) metal films to be deposited on top of the resist and then easily removed (lifted off) by dissolving the resist in a solvent (acetone). This liftoff process leaves a patterned metal film on all regions of the substrate where the resist was absent. With the tri-layer resist on the substrate, a low resolution contact mask is used to define the lead geometry which narrows to within ~ 75 μm of the RIE defined steps as shown in Fig. 4-3a. After developing this pattern (in the top layer only), the high resolution portion of the final pattern is then added by projection lithography with the Zeiss microscope as shown in Fig. 4-3b. Now the Al isolation layer is etched and the bottom layer developed to produce a controlled undercut as indicated in Fig. 4-4b and described in Appendix A.

---

[3] Shipley Corporation, Inc., Newton, Mass. 01730

4.2.3 Reactive Ion Etching (RIE)

Reactive ion etching is a well established technique for directional etching of many materials in the semiconductor industry [Chapman, 1980]. The formation of vertical steps, with little or no undercut, is quite well established with this technique. The basic idea behind RIE is that by accelerating a chemically reactive ion towards a surface, one can achieve an etching process that is quite directional (anisotropic). With the proper choice of etch gas and ion energy, the process can also have high selectivity between different materials. Our RIE system[4] is a standard parallel plate arrangement with water cooling of the upper and lower plates (electrodes). The parallel plates are separated by ~ 5 cm. The rf (13.56 MHz) power is capacitively coupled with a tuneable rf matching network. This allows the plates to acquire a dc self bias (300 - 400 V depending on the rf power). This self bias is what accelerates the reactive ions to achieve the directional etching (see Chapman, 1980). The stainless steel plates have a diameter of 11.4 cm (4.5 inches). We have covered the upper and lower plates with a 1.6 mm (1/16 inch) thick fused quartz disk. The quartz disk is held in thermal contact with the stainless steel plate by a thin layer of Fomblin[5] Y25/9 diffusion pump oil and three small stainless steel clips at the edge. Both the mechanical pump and the diffusion pump on this system use Fomblin pump fluids which are inert to all of our process gases (CF_4, CF_3Br, and O_2). The mechanical pump fluid is continuously filtered with an activated alumina filter system[6] to remove particulates and acids.

---

[4]Model CV-300 - Cooke Vacuum Products, Norwalk, CT.

[5]Montedison Co. - New York, New York.

[6]Model 1x21 - Motor Guard Corp., San Leandro, CA 94577

Reactive ion etching with oxygen is relatively straightforward. The standard etching conditions for oxygen that we use are: chamber pressure = 3.5 mTorr (as measured by an MKS[7] capacitance manometer), oxygen flow rate ≈ 6 sccm, rf power ≈ 30 W, dc self bias ≈ -400 V. This gives a photoresist etch rate of ~ 1000 Å/min. The pressure is feedback controlled with an MKS model 254 controller. This controller reads the pressure and adjusts the mass flow of oxygen to keep the pressure constant ± 5%. If more than one gas is being used (up to three), the controller can maintain a constant ratio between the gases while varying the total flow. This is useful when we use a mixture of O_2 and CF_3Br for etching Si.

Initial attempts in our laboratory to etch Si with pure CF_3Br [see, e.g., Matsuo, 1980] produced a large number of sub-micron hemispheres on the Si surface when examined in the SEM. The Si surface also appeared white (milky) to the eye on removal from the RIE system. It was believed that these hemispheres could be the result of polymer formation on the upper electrode which then "rains" down on the substrate and causes a temporary masking of the area under the polymer blob when it falls on the surface. The first attempt to eliminate this effect was to add some oxygen along with the CF_3Br to consume any excess carbon. When this did not work, a small amount of power was coupled to the upper electrode which is normally unpowered (but not grounded). This gave the upper electrode a self bias of ~ -100 V while the lower electrode continued to operate with a self bias of ~ -300 V. The purpose of the small self bias on the upper electrode is to help keep it clean and prevent polymer build up by continuously etching the surface. This technique gave a remarkable improvement in the Si wafer smoothness after etching. With these considerations in mind, the standard Si etching process uses the following conditions:

---

[7]MKS Instruments, Burlington MA

chamber pressure = 3.5 mTorr, rf power ≈ 30 W, dc self bias = -300 V (lower electrode) -100 V (upper electrode), CF_3Br flow rate ≈ 8 sccm, O_2 flow rate ≈ 0.9 sccm. Under these conditions an etch rate of ~ 500 Å/min is achieved. A step in a Si substrate after etching for ~ 13 min (6500 Å) is shown in Fig. 4-4 with the junction metallization on top.

4.2.4 Ion Beam Cleaning and Oxidation

A small Kaufman ion source was installed in the thermal evaporator for surface cleaning and ion beam oxidation. The source was loaned to us by J.M.E. Harper and J.J. Cuomo of IBM research for exploratory studies of ion beam oxidation and processing which are described in this section. This ion source has the same arrangement of ion optics (graphite grids) and discharge chamber as the large ion source discussed in chapter III but is physically smaller. The smaller size makes the placement and operation of the source in the vacuum system much easier. The grids produce an output beam which has a nominal diameter of 2.5 cm, but the current density is strongly peaked in the center. In order to characterize the operation of the source a number of test runs were performed to determine the maximum beam currents that could be extracted for a given beam voltage. It was found that the accelerator current was directly proportional to beam current for small currents, as expected [Kaufman, 1982]. As the beam current was increased beyond a certain threshold value, I_{max}, the accelerator current increased rapidly. By plotting the ratio of the beam current to the accelerator current (I(beam)/I(acc)) versus the beam current it is easy to see where this threshold appears for a given beam voltage as shown in Fig. 4-5 for Ar gas. Xe gas gave quantitatively similar results. It was expected that the maximum beam current would be limited by space charge (Child's Law) [Child, 1911; Kaufman et al., 1982] and be of the form $I_{max} \propto V^{3/2}$. This dependence appears to apply for the data in Fig. 4-5, but a

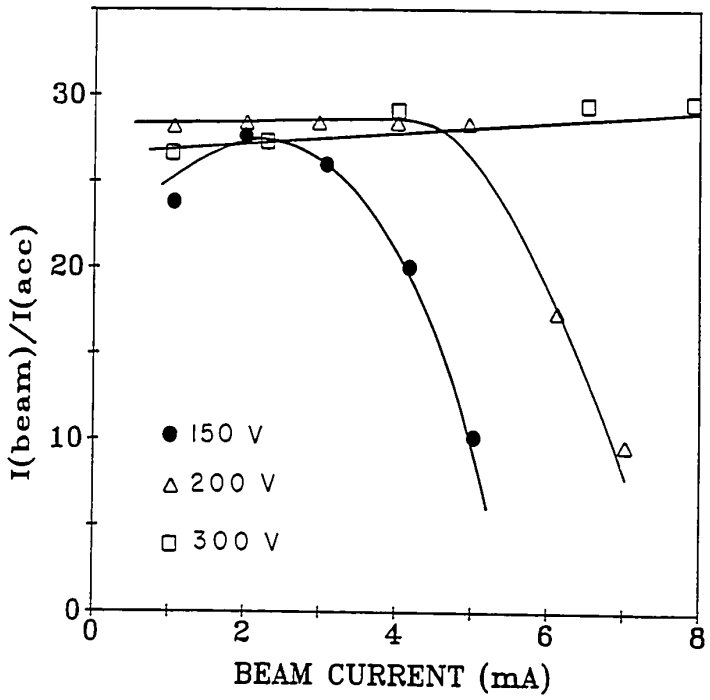

Fig. 4-5 Plot of (ion beam current/accelerator current) vs. the beam current for a series of beam voltages with Ar gas in the small IBM ion source. The maximum current for a given beam voltage is determined by the point where the accelerator current begins to climb rapidly (i.e., the ratio drops off).

more detailed study would be required. Accurate comparisons with Child's law are complicated by the non-uniform beam current density in our ion source and are discussed in detail by Kaufman et al., 1982. Based on the data in Fig. 4-5, the standard operating conditions of 160 V (beam voltage) and 2.0 mA (beam current) were chosen for Ar or Xe ion cleaning. These parameters represents a compromise between large beam current and low voltage operation. Low voltage is desirable for minimizing surface damage while a large beam current reduces the cleaning time and the effect of background impurities.

For ion beam cleaning it is first necessary to know the ion beam current density at the substrate. First, the ion beam was centered on the sample position by beaming on a 150 Å Al film (on a copper foil), observing the etched spot, and then repositioning the source. This process usually took one or two iterations for optimal source alignment. The current density was measured by positioning a 1 cm^2 Ta square (surrounded by a grounded shield) at the sample location with insulating stand-offs and connecting the Ta square to ground through a current meter. A total beam current of 2.0 mA produced a current density of ~ 130 $\mu A/cm^2$ at the sample position for a beam voltage of ~ 150 V and a source to sample distance of ~ 15 cm. A 200 V beam gave a slightly higher value of ~ 160 $\mu A/cm^2$. The corrections due to secondary electron emission are negligible at these energies (< 5%) [Chapman, 1980]. Low voltage sputter yields of Ta and Ta_2O_5 [Bispinick, 1979; Rosenberg, 1962; Laegreid and Whener, 1961] give a calculated Xe gas sputter rate of ~ 25 Å/min for Ta_2O_5 and 12 Å/min for Ta at 160 eV with current density of 130 $\mu A/cm^2$. Based on these numbers, a cleaning time of ~ 3 min was judged to be sufficient. Junctions made by cleaning and not oxidizing always produced shorts when a 3 min cleaning time of the Ta surface was employed, indicating that the surface was truly clean.

The small ion source was also used in a large number of attempts to grow an oxide tunnel barrier by ion beam oxidation. This technique was first used successfully for making SIS tunnel junctions (Nb/PbBi) by Kleinsasser, (1980, 1981) and further developed by Pei and van Dover, (1983). The basic idea is to take advantage of the directional energy and controlled ion current density of the ion source to grow reproducible and high quality barriers. In this regard, low energies (< 200 eV) are desirable for minimizing surface and interface damage in the tunnel barrier [Pei and van Dover, (1983)]. In our system, ion beam oxidation was performed by adding a small flow of oxygen to the Xe that was flowing into the ion source to produce an O_2/Xe ion beam. Both the Xe and O_2 flows were set with precision leak valves[8]. The Xe flow was adjusted to give a chamber pressure of 1.7×10^{-4} Torr (~ 1-2 sccm) while the O_2 flow was separately adjusted to give a chamber pressure of 2×10^{-5} torr. The chamber pressure tended to drift downward after an initial flow setting and generally required several readjustments of the gas flow over a 3-4 min period before the ion source was turned on. This problem is not important for single gas operation, but should be fixed for future mixed gas experiments by employing active feedback on the mass flow of each gas. We note however that it can become expensive to accurately control flow rates less than 1 sccm such as we have for oxygen.

After a number of O_2/Xe runs with tungsten and tantalum cathode filaments, it was found that the filaments only lasted for about 1 hour before they burned out. The precursor to the burnout was a gradual decrease in the required cathode current to maintain the discharge (because the filament resistance was increasing). Aside from the inconvenience of frequent filament changes, the oxidized filament material (an insulator)

---

[8]Series 203 - Granville Phillips Co., Boulder, Colorado.

tended to build up on the anode surfaces to the point where the source would stop working. The anode coating was removed by abrasive cleaning with #600 grit SiC paper. To avoid these problems, a set of special Thoria coated Iridium filaments were ordered[9]. These filaments have a very long life in oxygen environments and are commonly used in ion gauges. The first filament installed is still operating (after more than 50 hours of use). An additional advantage of these filaments is the lower operating temperature required for the same filament emission current.

As discussed in chapter V, the ion beam oxidation studies did not produce very high quality junctions nor was the process very reproducible. We note that all of the ion beam oxidation results in chapter V were obtained when using Ta filaments in the ion source. The few ion beam oxidized samples that were made with the the Thoria coated Iridium filaments showed similar behavior (in terms of not being reproducible and always having poor I-V characteristics). Possible explanations of this behavior are discussed in chapter V. In the meantime the successful glow discharge oxidation technique was discovered for Ta junctions. For this reason, the reported results on ion beam oxidation are limited in scope. Despite the disappointing oxidation results, we did learn that the Ta surface can be effectively cleaned with the low energy Xe ion source. As discussed in the next section, the ability to carefully control the cleaning process (on the Å level) turned out to be very useful when trying to clean a thin (~ 70 Å) Ta overlayer on Nb without removing it.

4.2.5 Artificial Barriers - Al and Ta

Al was used as an oxidized metal overlayer (OMO) barrier on Ta base electrodes to improve the tunneling characteristics over those obtained with

---

[9]Electron Technologies Inc., Kearny, NJ.

ion beam or thermally oxidized tunnel barriers. Al overlayers are also discussed in chapters III and V. The technique employed with our junctions was to follow the standard procedure up through the surface cleaning before oxidation. At this point a thin (~ 50 Å) Al film was evaporated onto the Ta surface at ~ 10 Å/sec. After evaporation, the hi-vac valve was closed and 1 Torr of pure oxygen admitted to the chamber to oxidize the Al film surface for ~ 20 min. After oxidation, the system was reevacuated to ~ $1x10^{-6}$ Torr and a $Pb_{0.9}Bi_{0.1}$ counter-electrode (3500 Å) evaporated at ~ 40 - 50 Å/sec. See sample #TJ29C in table 5-2 for electrical characteristics.

The Ta overlayers on Nb were prepared in a different fashion from Al. Namely, a Ta overlayer (~100Å) was deposited on the Nb film surface in the ion beam system immediately after deposition by merely switching sputtering targets. Switching targets takes ~ 1 sec. After this, the standard process steps were followed except for a slightly reduced ion cleaning time of 2 min rather than 3 min. See sample #TJ31F in table 5-3 for electrical characteristics.

4.2.6 DC Glow Discharge Oxidation

The dc glow discharge oxidation process was unquestionably the best technique for producing high quality SIS tunnel junctions with Ta base electrodes. DC glow discharges have been discussed in general by many authors (see for example Chapman, 1980) and are reasonably well understood in terms of the electrical potential distributions. The understanding of the complicated plasma oxidation chemistry is still largely empirical, however, especially when multiple reactive gases are involved. In our system, we employ a simple arrangement where the negatively biased electrode (a 10 cm diam. pure Al plate) is placed approximately 5 cm below the sample holder. The Al plate is backed by a ~ 12 cm diam. fused quartz plate. The fused

quartz plate helps to confine the glow discharge to the region between the Al plate and the sample holder by acting as an insulator between the Al plate and other grounded surfaces in the system. With this arrangement, an applied potential of ~ -390 V to the Al plate produces a dc glow discharge between the plate and the grounded sample holder. The discharge current is ~ 3 mA. The chamber pressure for these conditions is ~ 125 mTorr of pure oxygen. The oxygen pressure is maintained by setting the leak valve, discussed above for the ion source, so that the chamber pressure remains constant with a steady flow of O_2. The success of this process can be understood by recognizing that the ion energies at the junction surface are on the order of the plasma potential (< 20 eV) which is low for plasma processes. In addition, the higher pressure (compared to IB oxidation) allows the process to be less directional and more isotropic due to the shorter mean free path (~ 500 μm at 100 mTorr). This also eliminates the potential edge shadowing effects which may have caused the reproducibility problems with ion beam oxidation, as discussed in the next chapter. Glow discharge oxidation, in contrast, produces a uniform oxidation of the entire Ta junction surface.

4.3 Conclusions

The fabrication techniques described in this chapter are essential to the production of high quality SIS junctions for SIS mixer experiments. The novel step defined process has allowed the complete fabrication of junctions with no intervening resist processing steps. While this process may not be well suited to some applications, it has a number of unique advantages that make it particularly useful for SIS mixer fabrication. Although artificial barriers have been successfully implemented with the step process, Ta barriers formed by glow discharge oxidation were the best. The electrical properties of these junctions are discussed in chapter V.

V. DC JUNCTION MEASUREMENTS

This chapter describes the dc measurement techniques and results for the large and small area junctions that were fabricated in chapter IV. The chapter is broken into four major sections;

1.) Measurement techniques and cryogenic apparatus
2.) Large area junction results
3.) Small area junction results
4.) Discussion of tunneling mechanisms for "non-ideal" junctions

A special sample mounting technique with cryogenic spring contacts is described that allows for the rapid but careful measurement of a large number of small area junctions for SIS mixer experiments in chapter VI. The results for large area Ta/PbBi junctions show that low current density tunnel junctions of very high quality can be produced by simple air oxidation of our ion-beam deposited Ta films. The use of alternative barrier and counter-electrode materials is also described. The results for small area junctions with high current density show that a low energy ion cleaning followed by a dc glow discharge oxidation as discussed in chapter IV is crucial in obtaining low leakage Ta junctions at high (10^3 - 10^4 A/cm^2) current density. These tunnel junctions are among the lowest leakage and sharpest SIS junctions that have been reported to date in any junction technology at this current density. These low leakage and sharp I-V characteristics are crucial in obtaining the low noise mixing results of chapter VI. A number of physical mechanisms that can cause excess subgap current and a width to the current rise at the sum gap in our junctions are also discussed.

5.1 Low Temperature Apparatus

This section briefly describes the cryogenic equipment used at Yale for making low temperature electrical measurements of tunnel junctions and films. The cryostat is of standard design [White, 1979] and is very similar (except for the electrical lead configuration) to that used by B.J. Dalrymple and described more fully in his thesis [Dalrymple, 1983]. The low temperature end of the cryostat consists of a variable-temperature copper block located inside of a copper vacuum can. A separate copper can with two small holes at the bottom is often substituted for the vacuum can in order to make measurements directly in the LHe bath. The copper block has special electrical spring pressure contacts for making electrical connection to the small tunnel junction samples as described in the next section. The copper block also contains a thermally anchored electrical heater (1 kohm metal film resistor) and a calibrated Ge resistance thermometer, Cryocal[1] model RCR 1000. LHe bath temperatures as low as 1.25K could be easily achieved by pumping on the bath with two large mechanical pumps with a combined pumping speed of ~ 300 ft^3/min.

5.1.1 Sample Mounting

The large area tunnel junctions described in chapter IV and the thin films described in chapter III were mounted directly on the copper block with a small amount of Dow Corning silicone vacuum grease on the back of the substrate to hold them in place. Electrical contact was made with small #38 copper wires and pure indium or silver paint[2]. The indium was heated on a small soldering tip and then briefly touched to the desired contact area to make a secure mechanical and electrical connection. Only

---

[1] Cryocal, Inc., St. Paul, MN 55114.

[2] SC-12 Silver paint from - Micro-Circuits Company, New Buffalo, MI

silver paint contact was used only for making contact to the soft Pb and PbBi counter-electrodes of tunnel junctions, in order to avoid possible alloying with or melting of the film.

A special sample holder for the small tunnel junctions was constructed to allow the rapid testing of a large number of samples. It is shown in cross section in Fig. 5-1. The first part of the holder is a small copper plate measuring 5.72 x 0.89 x 0.16 cm^3 on which the samples were mounted (junction side up) with a small amount of high quality mechanical pump oil. The small drop of oil was spread uniformly over the surface of the copper plate and the back of the substrate to hold the sample in place during the rest of the assembly process. The copper plate also has two small alignment holes for aligning it with the rest of the copper block in Fig. 5-1. The other part of the holder has an arrangement of spring contact pins called POGO[3] pins (model ASR) as shown in Fig. 5-1. The pins were arranged such that two contacts for voltage and two contacts for current were made to each junction for performing four point electrical measurements as shown schematically in Fig. 5-2. A total of four junctions could be measured on one substrate which required a total of sixteen contacts. With careful sample alignment on the copper plate, all sixteen contacts were quite reliable.

5.2 Electronic Instrumentation

For the small area junctions, each electrical connection was made through a connection box on top of the cryostat. This grounded aluminum box contained shorting switches and EMI (electromagnetic interference)

---

[3] POGO is a registered trademark of the Pylon Co., Inc., 51 Newcomb St., Attleboro, MA 02703.

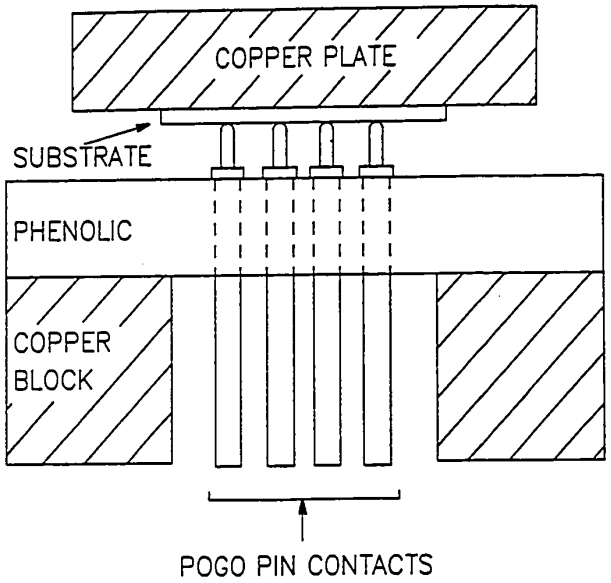

Fig. 5-1: Cross section view of the sample mounting block with the sample on the copper plate. The POGO pins are spring loaded electrical contacts arranged to make electrode contact as shown in Fig. 5-2.

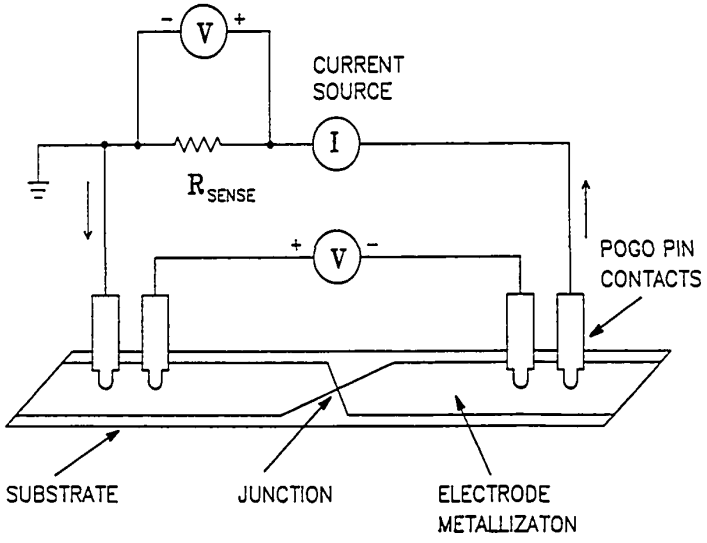

Fig. 5-2: Arrangement of the instrumentation and electrical contacts for making 4 point dc electrical measurements.

suppression filters[4] with a minimum of 50 dB insertion loss above 100 MHz. Each wire from the junction was connected through an EMI filter and a shorting switch as shown in Fig. 5-3. The shorting switch on each wire was useful when switching between different junctions to avoid electrical transients and junction burn out. Although Fig. 5-3 is drawn for a voltage lead going to the preamp, the switch and filter configuration was the same for current and voltage leads. The wires going from the EMI filters to the POGO pins at the junction were twisted pairs of insulated #38 wire. Both wires in a particular twisted pair always went to the same junction as either current leads or voltage leads. Electrical connections for the large area junctions and films did not have the EMI filters or shorting switches, but were otherwise the same as above.

The chopper input of most voltmeters and chart recorders was found to introduce extra noise into the sample and degrade the electrical measurement of the very sharp low leakage junctions discussed below. With this in mind, all voltage measurements (including the sense resistor for measuring the junction current) for the small area junctions were made by first amplifying the voltage with a precision instrumentation amplifier[5] (preamp) shown in Fig. 5-4. These preamps have an accurate gain calibration (±0.1% at G = 10), very low noise ($7nV/(Hz)^{1/2}$ at 1 kHz) and a high input impedance of 10^9 Ω. These preamps were also battery powered to eliminate 60 Hz pick-up. The output of the preamp then went directly to the chart recorder (HP 7047A) and/or the digital voltmeter (DVM)(HP 3556A or HP 3478A). The DVM's were interfaced to an HP 9816 computer for digitizing the data.

The current source shown in Fig. 5-2 and drawn schematically in Fig.

---

[4] Part # 1212-502, ERIE Technological Products, Inc., Erie, PA.

[5] Model AD 524C from Analog Devices, Norwood, MA 02062

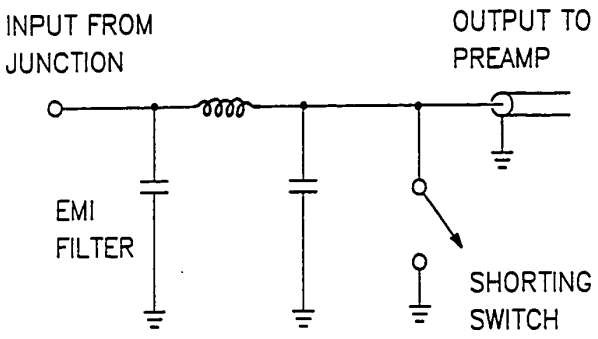

Fig. 5-3: EMI filter and shorting switch on each electrical lead to the sample in Fig. 5-2.

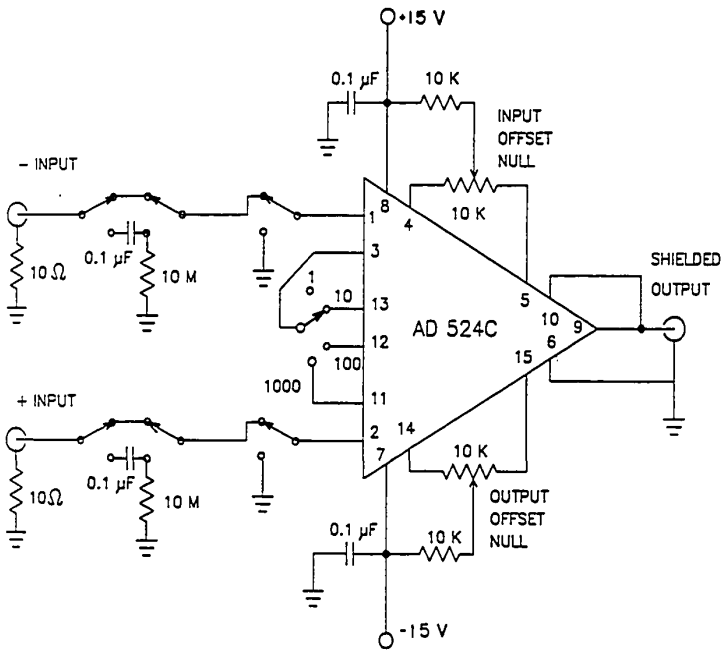

Fig. 5-4: Low noise preamplifier for all junction measurements

5-5 is capable of ramping the junction current from negative to positive values smoothly through zero [see Ruggiero et al., 1986b]. The ability to ramp through zero is not found in most current sources, but is important for the tunnel junction measurements described here. The current range, ramp speed and starting current are all adjustable from the front panel of the current source. In addition to producing dc current for I-V measurements, the current source could also produce a small ac current modulation δI on top of the dc current for performing dV/dI vs. V measurements. In this case the tunnel junction voltage has a small ac voltage component δV given by $\delta V = (dV/dI)\delta I$ where δI is the amplitude of the ac current modulation and dV/dI is the differential resistance at the bias voltage. δV was measured directly with a lock-in amplifier[6] set to the same frequency as δI and V was measured as described above. δI was always adjusted to produce a δV which was smaller than any structure being examined in dV/dI. A δV of less than 10-20 μV was usually sufficient. These measurements were useful in determining the tunnel barrier characteristics such as barrier height and thickness as discussed below.

5.3 Large Area Junction Measurements

The large area junctions which were fabricated with the procedures in chapter IV have been carefully measured with the low noise techniques just discussed. These large area (75 x 300 μm^2) junctions served to prove the concept of producing high quality $Ta/Ta_2O_5/PbBi$ tunnel junctions at low tunneling current densities (< 1 A/cm^2) with our ion-beam deposited Ta films. The success of these junctions lead to the work on small area high current density junctions discussed in section 5.4. In the course of this study, several counter-electrode materials (Sn, Pb, and $Pb_{0.71}Bi_{0.29}$) and

---

[6] PAR Model 126 - Princeton Applied Research, Princeton, NJ.

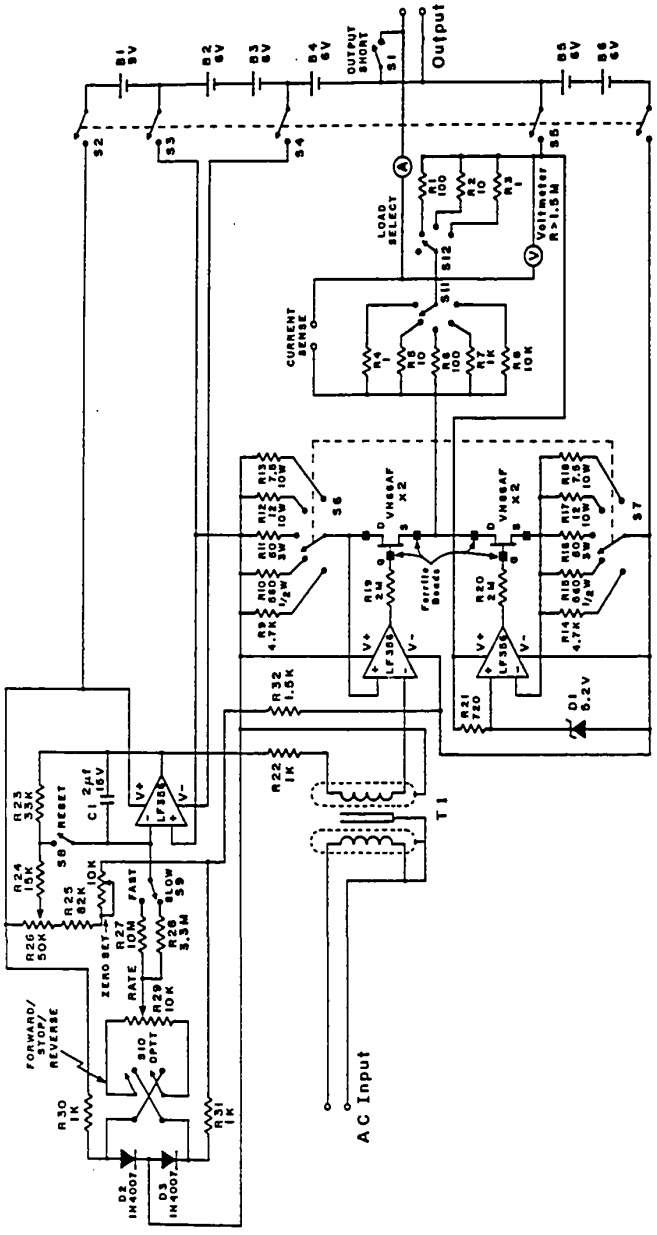

Fig. 5-5: Low noise ac/dc current source with continuous zero crossing. [from Ruggiero et al., 1986]

two tunnel barrier materials (Ta_2O_5 and sputtered amorphous Si) were evaluated. The Josephson critical current of the large junctions was often suppressed due to stray magnetic fields and was not measured carefully. For this reason the I-V curves do not show the Josephson current at zero voltage. All of the measurements were taken at 1.3K unless otherwise noted. The results are summarized in Table 5-1 and discussed below.

5.3.1 Tunnel Barrier Materials and Characterization

The properties of the various tunnel barriers produced on the Ta base electrodes have been characterized with a trapezoidal barrier model using the WKB approximation. This model assumes an ideal barrier with a barrier height ϕ_1 on the left and ϕ_2 on the right and a uniform thickness d. As discussed in chapter II and III and section 5.5 , this model is certainly a simplification of the complex nature of most real tunnel barriers, but is nonetheless a useful parametric tool for describing the properties of a large number of junctions. This model has been solved and put in a form that is useful for computing barrier parameters directly with dV/dI data from tunnel junctions by Brinkman, Dynes and Rowell (1970). (See also [Wolf, (1985)]). The equations derived by these authors are,

$$eV_{min} = 0.649\ (\Delta\phi/d\phi^{1/2}) \qquad 5\text{-}1$$

$$V^{+} + V^{-} = 11\phi^{1/2}/d \qquad 5\text{-}2$$

$$G(0) = (3.16\text{x}10^{10}\ \phi^{1/2}/d)\exp(-1.025\ d\phi^{1/2}) \qquad 5\text{-}3$$

where d is the barrier thickness in Å, ϕ is the average barrier height $(\phi_1 + \phi_2)/2$ in eV, and $\Delta\phi$ is the difference between ϕ_1 and ϕ_2 in eV. G(0) is the conductance (dI/dV) at zero bias in mhos/cm^2, V_{min} is the voltage

TABLE 5-1 Summary of large area Ta junction properties measured at 1.3K. I_{sg} is the subgap current that flows at 90% of the sum gap, ΔV is the width of the current rise at the sum gap (10% to 90%), R_N is the normal state resistance of the junction, t_{ox} is the oxidation time, ϕ and d are the tunnel barrier height and width respectively (determined from junction conductance vs. voltage). The PbBi alloy for all of these junctions is 29 wt.% Bi and 71 wt.% Pb.

Sample	Counter-electrode	barrier	t_{ox} (min)	R_N (Ω)	ΔV (μV)	$I_{sg}/\Delta I$	ϕ (eV)	d (Å)
83-006-2a	PbBi	Ta_2O_5	40	5.36	25	5%	0.87	15.8
83-006-2b	PbBi	Ta_2O_5	40	6.84	25	5%	0.81	16.5
83-006-2c	PbBi	Ta_2O_5	40	5.93	25	5%	0.84	16.1
83-006-3a	PbBi	Ta_2O_5	40	1.96	10	2.5%	...	...
83-006-3b	PbBi	Ta_2O_5	40	1.95	10	4%	...	...
83-006-3c	PbBi	Ta_2O_5	40	1.15	10	2.5%	...	...
83-006-5a	PbBi	Ta_2O_5	240	1.67	20	2.5%	...	...
83-006-5b	PbBi	Ta_2O_5	240	1.67	20	2.5%	...	...
83-006-5c	PbBi	Ta_2O_5	240	1.30	20	2.5%	...	...
83-006-8a	PbBi	Ta_2O_5	240	278	25	1%	1.0	18.4
83-006-8b	PbBi	Ta_2O_5	240	260	25	1%	...	...
83-006-8c	PbBi	Ta_2O_5	240	278	25	1%	...	...
83-008-2a	Sn	Ta_2O_5	95	1.97	50	5%	1.17	13.0
83-008-2b	Sn	Ta_2O_5	95	1.12	50	5%	...	...
83-008-4a	Sn	Ta_2O_5	300	722	200	5%	0.71	22.5
83-008-4b	Sn	Ta_2O_5	300	1129	200	5%	...	...
83-008-7a	PbBi	50Å a-Si	10	40.0	150	10%	0.041	68.0
83-008-7b	PbBi	50Å a-Si	10	30.8	...	10%	...	...
83-008-8a	PbBi	70Å a-Si	10	172	150	5%	0.045	71.5
83-008-8b	PbBi	70Å a-Si	10	174	150	5%	...	...
83-013-2a	Pb	Ta_2O_5	75	5.56	150	5%	...	...
83-013-2b	Pb	Ta_2O_5	75	7.18	150	5%	...	...
83-013-2c	Pb	Ta_2O_5	75	9.44	150	5%	...	...
83-013-3a	Pb	Ta_2O_5	140	11.31	150	5%	0.985	15.6
83-013-3b	Pb	Ta_2O_5	140	19.34	150	4%	...	...
83-013-3c	Pb	Ta_2O_5	140	27.89	150	3%	...	...

where the conductance is a minimum, V^+ is the positive voltage at which the conductance doubles and V^- is the negative voltage at which the conductance doubles. V^+ and V^- were typically ~ 300 mV for the 0.8 eV barriers listed in Table 5-1. The barrier asymmetry $\Delta\phi$ which is not listed in table 5-1 was always less than 10% of ϕ.

An examination of the barrier data in table 5-1 shows that the Ta_2O_5 barrier height is almost always in the range of 0.8 to 1.0 eV. In addition, the general observation of increasing Ta_2O_5 barrier height with decreasing barrier thickness is consistent with the results of Ruggiero et al. (1986a) on a wide range of barrier materials and current densities. The two junctions with amorphous Si (a-Si) barriers show a low barrier height of ~ 0.05 eV and relatively poor I-V curves as seen in Fig. 5-6. These results with a-Si barriers are comparable to the much more extensive work on a-Si barriers in the literature [see for example Jillie et al.,1982; Meservey et al., 1982; and Beasley, 1980]. Due to the increased leakage of the a-Si barriers compared to the high quality Ta_2O_5 barriers these studies were not pursued further. It is interesting to note, however, that the simple barrier model gives a thickness d that is quite close to the actual deposited thickness of a-Si which gives one additional confidence in the barrier model predictions.

5.3.2 DC I-V Curves

The notion of I-V quality necessarily implies that we have a standard I-V curve with which to compare and a well defined way of making the comparison. With this in mind, all of the experimental I-V curves have been characterized by measuring the ratio of the subgap current at 90% of the sum-gap voltage (I_{sg}) to the current rise at the sum-gap (ΔI). The voltage width ΔV of the current rise at the sum-gap is the voltage required to increase the current at the sum-gap from 10% to 90% of ΔI. For clarity, the sum-gap in this work is defined to be the inflection point of the

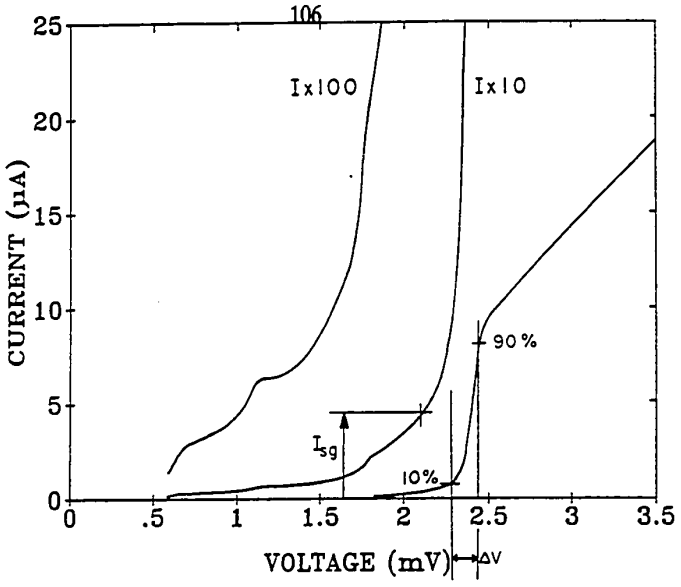

Fig. 5-6: I-V curve for an amorphous Si tunnel barrier junction (83-008-8a) with the parameters ΔI, I_{sg}, ΔV, and V_G defined.

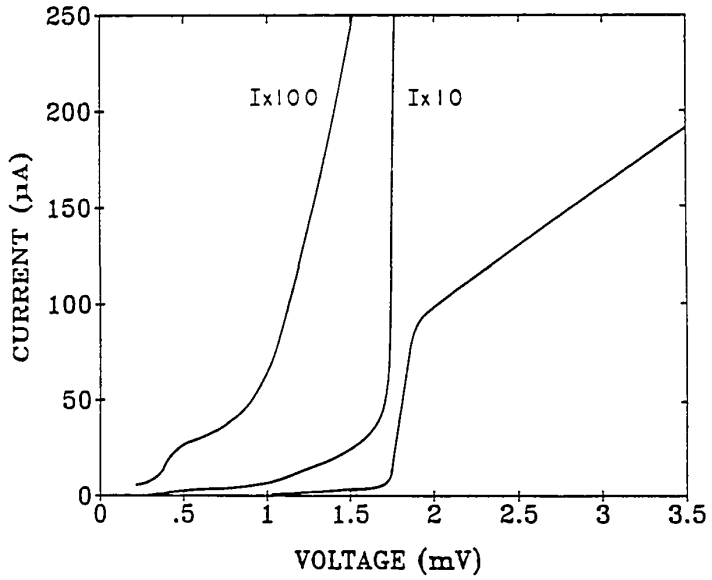

Fig. 5-7: I-V curve of a Ta/Pb tunnel junction (83-013-3c) showing the width of the current rise at the sum gap which is due to anisotropy effects in polycrystalline Pb films.

current rise ΔI. These definitions are indicated graphically in Fig. 5-6 for an a-Si tunnel barrier junction. A summary of these parameters for all of the large area junctions is given in Table 5-1.

Although excellent I-V's were obtained with a $Pb_{0.71}Bi_{0.29}$ counter-electrode, pure Pb and Sn counter electrodes were also evaluated. Pure Pb was also used in the early junction work to eliminate any possible complications due to the variation of the energy gap or crystal structure in an alloy counter electrode such as $Pb_{0.71}Bi_{0.29}$. The I-V curve of a junction with pure Pb counter-electrode is shown in Fig. 5-7 and illustrates the width ΔV to the current rise ΔI that is typically found with thick polycrystalline Pb junction electrodes. This width appears to be due to an intrinsic gap broadening typical of relatively thick polycrystalline lead films, where the energy gap is a function of crystallographic direction as discussed in chapter II and section 5.5.5. This effect is consistent with that observed in the high quality tunneling data of Shen (1972) on Ta/Pb junctions.

As shown in Fig. 5-8, a number of the junctions made with the $Pb_{0.71}Bi_{0.29}$ counter-electrodes exhibited a proximity effect "knee" structure at the sum-gap. This effect is discussed in section 5.5.2 and results from the presence of a thin normal or reduced T_c layer at the interface between the barrier and the thick superconducting electrode. This problem may be due to the undesired presence of a second phase of PbBi if the composition is not correct for the pure ϵ phase (hcp)(29 wt.% Bi) as discussed in chapter III. This problem was later solved by switching to a $Pb_{0.9}Bi_{0.1}$ composition for the small area junctions. This 10% Bi mixture produces an fcc phase and is very easy to deposit from an alloy source since the single phase region exists for the fcc phase with Bi concentrations from 0 to 17 wt.% (see phase diagram in chapter III).

The I-V curve for one of the lowest leakage junctions is shown in

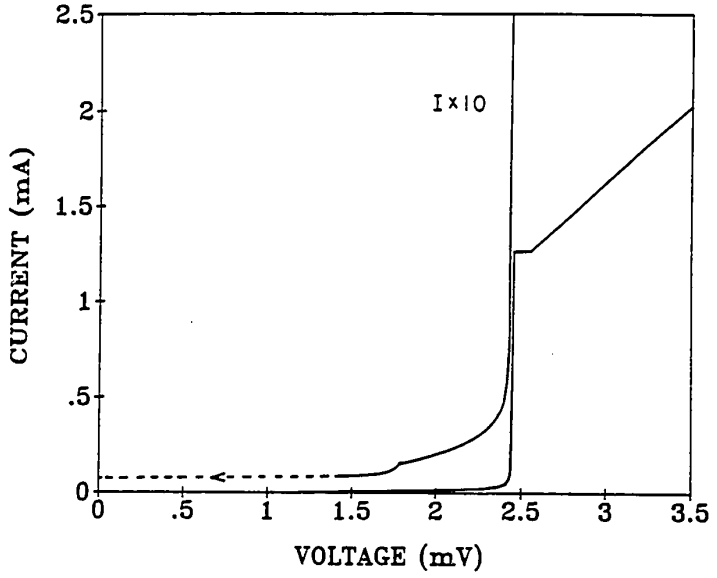

Fig. 5-8: I-V curve of a Ta/$Pb_{0.71}Bi_{0.29}$ tunnel junction with a proximity effect "knee" at the sum gap (83-006-5a).

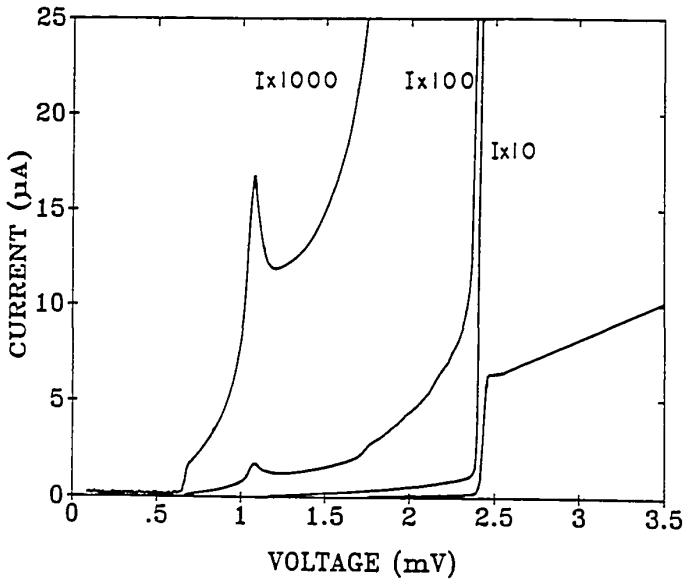

Fig. 5-9: I-V curve of one of the best large area Ta/$Pb_{0.71}Bi_{0.29}$ junctions (83-006-8c). The leakage is comparable to the best in the literature.

Fig. 5-9 with several amplifications of the current scale by factors of 10. This I-V is comparable (within a factor of 3) to the lowest leakage published I-V's in the literature [Shen, 1972] which used UHV outgassed single crystal Ta foils. These results can also be compared with the high quality $Nb/Al/Al_2O_3/Pb_{0.9}Bi_{0.1}$ junctions of Gurvitch et al. (1982) discussed in section 5.5.2 (see Fig. 5-21). As discussed in section 5.5, a number of different mechanisms can contribute to the subgap currents observed in these junctions and no one mechanism can be easily identified at this time. Most authors do not magnify the current below the energy gap so that a detailed comparison with other work was not always possible. As discussed in chapter III and section 5.5.3, the low levels of suboxide (TaO) formation found in Ta surface oxides [Himpsel, 1984] may favor the formation of a very abrupt metal to oxide interface and a nearly ideal tunnel barrier in these Ta junctions. The important conclusion of this section is that it is possible to make well characterized and very high quality junctions on our polycrystalline Ta films at low current densities. The extension of these results to small area and high current density junctions described in the next section and chapter IV was not trivial, however, since the relatively simple thermal oxidation techniques used here could not be easily extended to the high current density regime.

5.4 Small Area Junction Measurements

A large number ($n>100$) of small area junctions were fabricated and tested during the development of the step edge process in chapter IV. Many of the results were far from ideal and a reasonable degree of perseverance was required to continue trying new ideas when junctions came out shorted, leaky, or open circuited. It was by no means guaranteed that Ta would make good oxide barrier tunnel junctions at high current density. The experiments described in this section present the results of a

number of the different approaches that were tried before the best solution (dc glow discharge oxidation) was found. Some of these techniques, such as an oxidized Al overlayer, may ultimately be useful for other tunnel junction work with different materials. All of the I-V curves reported were measured in the LHe bath at 1.3K unless otherwise noted. The Josephson current is not indicated on most of the plots (so as not to complicate the figures) although it was always present as indicated in the tables of junction results.

5.4.1 Non Optimal Barriers - Al Overlayers, Ion Beam, and Thermal Oxidation

As discussed in chapter IV, a significant effort was made to produce junctions by using a low energy oxygen ion beam for oxidation of the Ta surface. The motivation for this work was provided by the high quality Nb junctions produced by Kleinsasser et al. (1981) using ion beam oxidation. When these techniques were attempted for Ta junctions in the step geometry, however, the results were not very reproducible or of very high quality. The I-V of one of the best ion beam oxidized junctions is shown in Fig. 5-10. Table 5-2 summarizes a selected but representative set of ion beam oxidized junctions. (Those that were very low resistance ($<1\Omega$) or open circuited have been omitted.) The subgap leakage in these junctions was almost always >20%. The junction resistances on the same wafer were sometimes different by a factor of 100 and not reproducible from run to run with the same cleaning and oxidation procedures. At the present time, this irreproducibility is believed to be due to the geometry of the step defined process and the directional nature of ion beam processing. In particular, the presence of a large photoresist overhang near the junction area can cause a shadowing of the edges of the junction area during the ion beam cleaning. This shadowing means that, after cleaning, the portions

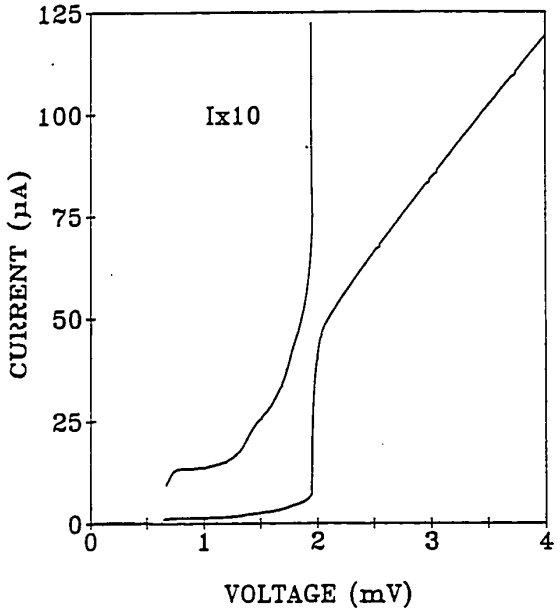

Fig. 5-10: I-V curve for an ion beam oxidized Ta/Pb tunnel junction (TJ25A4).

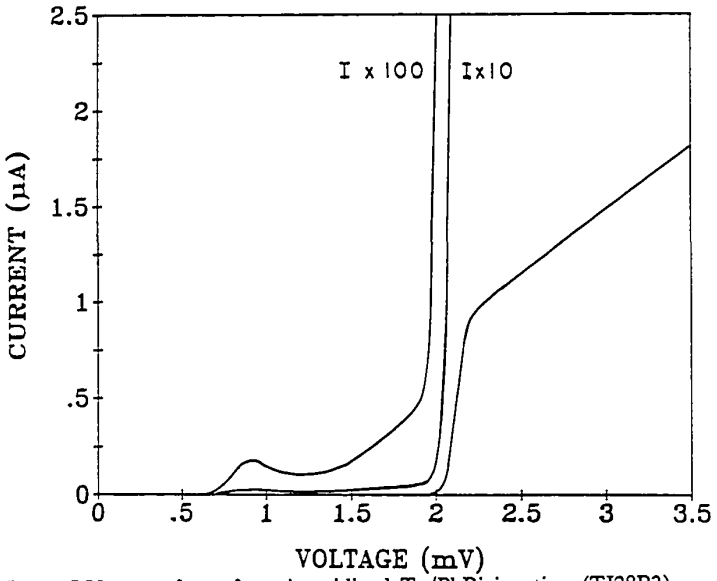

Fig. 5-11: I-V curve for a fast air oxidized Ta/PbBi junction (TJ28B3).

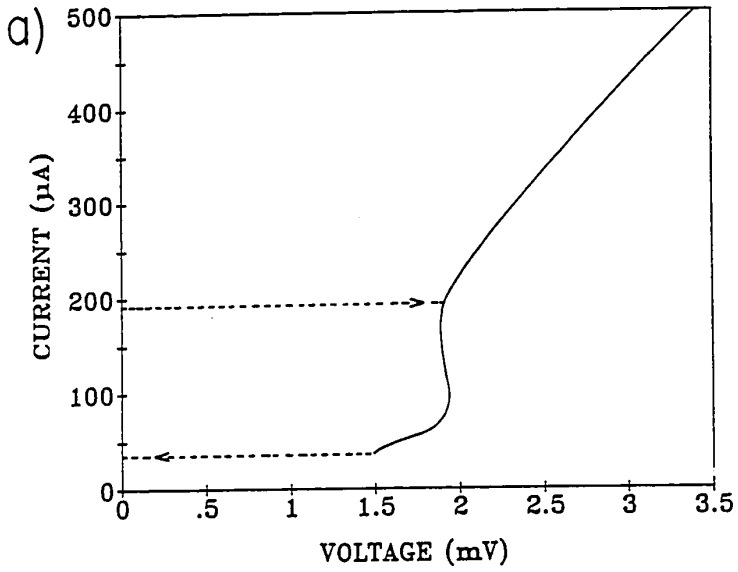

Fig. 5-12: (a) I-V curve for a low pressure O_2/H_2O oxidized junction (TJ30C2) (b) after 6.5 hour air anneal.

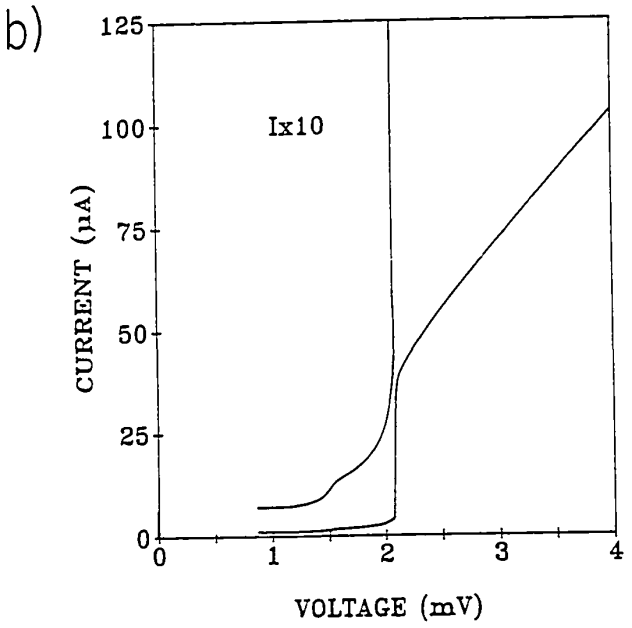

TABLE 5-2 Summary of small area Ta junction properties with various oxidation techniques other than dc glow discharge (see Table 5-3). The measurement temperature is 1.3K. I_{sg} is the subgap current that flows at 90% of the sum gap, ΔV is the width of the current rise at the sum gap (10% to 90%), R_N is the normal state resistance of the junction, I_c is Josephson critical current, and t_{ox} is the oxidation time. The PbBi alloy for all of these junctions is 10 wt.% Bi and 90 wt.% Pb.

Sample	Counter-electrode	barrier	oxidation technique	t_{ox} (min)	R_N (Ω)	ΔV (μV)	$I_{sg}/\Delta I$	I_c (μA)
TJ19C1	Pb	Ta_2O_5	Ion Beam	1.5	<2	...	...	660
TJ19C1	Pb	Ta_2O_5	Air Annealed	3 hr.	6	...	...	250
TJ20A1	Pb	Ta_2O_5	Ion Beam	5.0	15.7	150	25%	52
TJ20A2	Pb	Ta_2O_5	Ion Beam	5.0	27.8	200	20%	28
TJ20A3	Pb	Ta_2O_5	Ion Beam	5.0	16.2	100	25%	55
TJ25A3[a]	Pb	Ta_2O_5	Ion Beam	6.5	2.5	...	25%	500
TJ25A4	Pb	Ta_2O_5	Ion Beam	6.5	33.6	...	15%	30
TJ28B3	PbBi	Ta_2O_5	air	12.0	1740	120	1%	...
TJ29C1	PbBi	Al_2O_3[b]	1 Torr O_2	20.0	1030	100	10%	...
TJ29C3	PbBi	Al_2O_3[b]	1 Torr O_2	20.0	804	100	3%	...
TJ30C2	PbBi	Ta_2O_5	O_2/H_2O	90.0	6.8	...	20%	290
TJ30C2	PbBi	Ta_2O_5	Air Annealed	6.5 hr.	39.7	...	8%	36

(a) Junction sent to Berkeley for testing gave T_M = 3.8K
(b) Ta base electrode with 50Å aluminum overlayer.

of the tunnel junction area at the edge may not be fully oxidized by the ion beam oxidation process and therefore lead to shorts or low resistance. It is the directional nature of ion beam cleaning and oxidation process that causes edge effects to become important. Small variations in the ion beam angle and photoresist geometry from junction to junction can therefore lead to a large variation in junction resistances.

Attempts to use a fast air transfer (< 10 minutes) from the ion beam deposition system (for Nb or Ta) to the thermal evaporator for the $Pb_{0.9}Bi_{0.1}$ counter-electrodes almost always produced junctions with too large of a resistance (R > 1kΩ) although the I-V curves were quite good (see Table 5-2 and Fig. 5-11). Based on this information, we also attempted to clean the Ta surface with a low energy ion beam (~ 150 eV) after air transfer and then re-oxidize the surface by admitting oxygen into the system. The Ta surface after ion cleaning, however, was slow to oxidize for some unknown reason. One might even expect that the sputter cleaned surface should be more reactive due to the rough and damaged nature of the surface. One possible explanation for the slow oxidation rate is that a carbide layer, like that found in some Nb junctions [Kuan et al., 1982] after ion cleaning, is passivating the surface and reducing the oxidation rate. In addition to the slow oxidation, the I-V curves themselves were not outstanding as shown in Fig. 5-12.

A final approach which produced some promising results was the deposition of thin overlayer of Al after ion cleaning of the Ta surface. The thin aluminum overlayer was then thermally oxidized to form an Al_2O_3 tunnel barrier as described in more detail in chapter IV. These junctions had reasonable I-V curves as shown in Fig. 5-13 and probably could have been optimized to achieve the right resistance (~ 50Ω) with additional work. This approach is based on the successful Al overlayer techniques developed by Gurvitch et al. (1981) and discussed briefly in section 5.5.2. Although

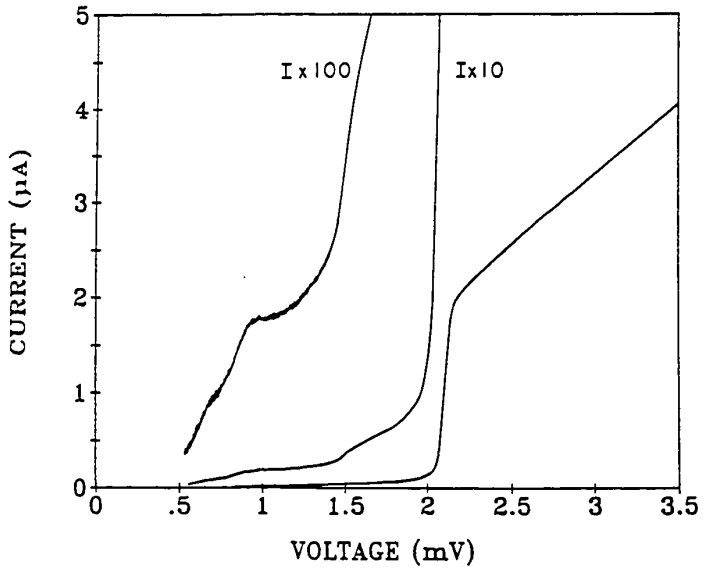

Fig. 5-13: I-V curve of an Al overlayer junction (TJ29C2).

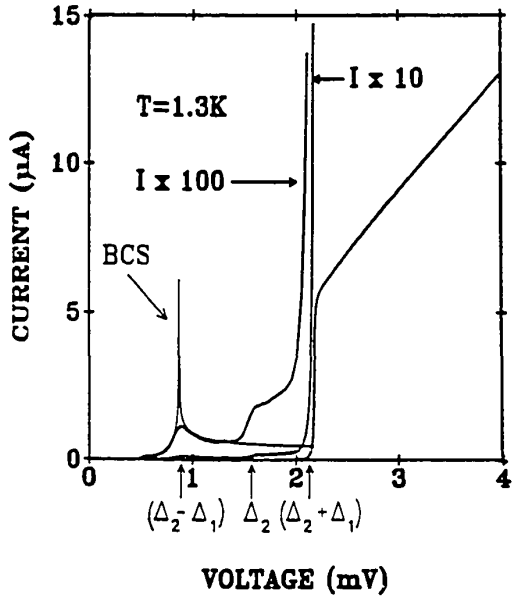

Fig. 5-14: I-V curve of a glow discharge oxidized Ta/PbBi junction (TJ31C3) with the current scales magnified by factors of 10 and 100. The curve labeled BCS is the BCS subgap current (x100) for two superconductors at 1.3K (Δ_1 = 0.65 mV (Ta) and Δ_2 = 1.54 mV (PbBi)). This BCS current is very close to the measured current (x100) up to Δ_2.

the Al overlayer technique was not actively pursued in this work, it might be a useful starting point for making tunnel junctions with more difficult materials such as Nb, NbN and A-15 compounds.

5.4.2 DC Glow Discharge Oxidation

The success of the dc glow discharge oxidation technique for Ta junctions was nothing less than a major breakthrough for making reproducible high current density Ta junctions required for the mixer experiments of chapter VI. The dc glow discharge technique (see also chapter IV) is an ion assisted process like the ion beam oxidation technique, but the ion energy is low (10 - 20 eV) and is not directional. The lack of directionality helps to minimize the shadowing effects that are present in ion beam oxidation. Quite a few junctions were made with this technique and their properties are summarized in Table 5-3. All of the junctions made with a 20 sec. oxidation time had resistances within a factor of two of each other ($\simeq$ 20 Ω) even though this data represents the results of three totally different fabrication runs. Other oxidation times also had quite predictable results. A number of I-V curves for different junctions produced with the glow discharge process are shown in Figs. 5-14 to 5-18 (all measured at 1.3K). Fig. 5-14 compares the sub gap current in one of the best junctions with the predictions of the BCS theory at 1.3K. Clearly the current below the $Pb_{0.9}Bi_{0.1}$ gap Δ_2 is well fit by the BCS theory (if a little noise rounding is added to smooth out the singularity at Δ_2 - Δ_1). The current rise at Δ_2 may well be explained by a combination of multiparticle tunneling and some normal metal inclusions at the Ta interface as discussed in section 5.5 but this is not clearly resolved at this time. The higher current density junctions (lower resistance) show even more leakage which suggests that there is a universal mechanism that degrades the quality of junctions as the current density is increased beyond 10^3 A/cm^2.

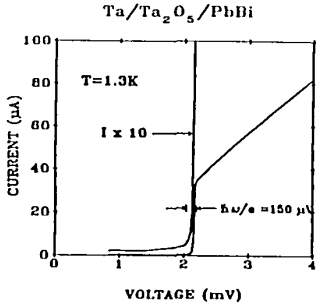

Fig. 5-15: I-V curve for a glow discharge oxidized Ta/PbBi junction measured at UC Berkeley and used for mixer experiments in chapter VI.

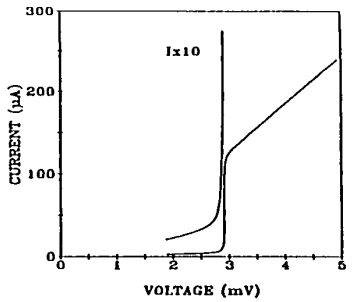

Fig. 5-16: I-V curve of an exceptionally good Nb/PbBi glow discharge oxidized tunnel junction (TJ31E4).

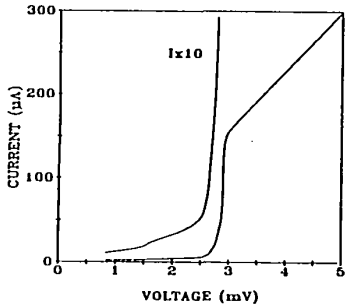

Fig. 5-17: I-V curve of a typical Nb/PbBi glow discharge oxidized tunnel junction showing rounding at the gap and subgap leakage current.

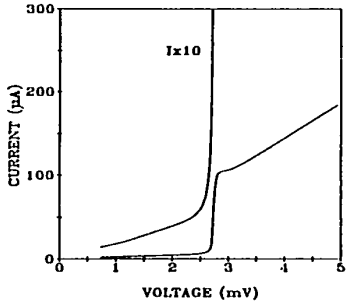

Fig. 5-18: I-V curve of a 70Å Ta overlayer on Nb junction with glow discharge oxidation and a PbBi counter-electrode.

TABLE 5-3 Summary of small area Ta junction properties with dc glow discharge oxidation I_{sg} is the subgap current that flows at 90% of the sum gap, ΔV is the width of the current rise at the sum gap (10% to 90%), R_N is the normal state resistance of the junction, I_c is Josephson critical current, and t_{ox} is the oxidation time. The PbBi alloy for all of these junctions is 10 wt.% Bi and 90 wt.% Pb.

Sample	Counter-electrode	barrier	oxidation technique	t_{ox} (min)	R_N (Ω)	ΔV (μV)	$I_{sg}/\Delta I$	I_c (μA)
TJ31B1	PbBi	Ta_2O_5	dc Disch	0.25	4.29	50	10%	295
TJ31B2	PbBi	Ta_2O_5	dc Disch	0.25	3.51	50	10%	380
TJ31B3	PbBi	Ta_2O_5	dc Disch	0.25	7.87	50	5%	160
TJ31B4	PbBi	Ta_2O_5	dc Disch	0.25	7.85	50	5%	160
TJ31B1	PbBi	Ta_2O_5	Air Annealed	24 min.[a]	7.40	50	5%	165
TJ31B2	PbBi	Ta_2O_5	Air Annealed	24 min.[a]	6.04	50	5%	165
TJ31B3	PbBi	Ta_2O_5	Air Annealed	24 min.[a]	13.86	50	2.5%	165
TJ31B4	PbBi	Ta_2O_5	Air Annealed	24 min.[a]	14.90	50	2.5%	165
TJ31C1	PbBi	Ta_2O_5	dc Disch	0.50	324	50	1%	1.2
TJ31C2	PbBi	Ta_2O_5	dc Disch	0.50	435	50	5%	1.2
TJ31C3	PbBi	Ta_2O_5	dc Disch	0.50	317	50	0.5%	1.2
TJ31C4	PbBi	Ta_2O_5	dc Disch	0.50	370	50	0.5%	1.2
TJ31D1	PbBi	Ta_2O_5	dc Disch	0.33	24.0	20	2%	47
TJ31D2	PbBi	Ta_2O_5	dc Disch	0.33	24.7	20	2%	47
TJ31D3	PbBi	Ta_2O_5	dc Disch	0.33	14.4	20	2%	87
TJ31D4	PbBi	Ta_2O_5	dc Disch	0.33	21.2	20	1.5%	56
TJ31E1[b]	PbBi	Nb-oxide	dc Disch	0.33	22.4	200	3%	70
TJ31E2[b]	PbBi	Nb-oxide	dc Disch	0.33	17.2	200	2.5%	95
TJ31E3[b]	PbBi	Nb-oxide	dc Disch	0.33	16.2	200	3%	102
TJ31E4[b]	PbBi	Nb-oxide	dc Disch	0.33	19.9	20	2.5%	82
TJ31F1[c]	PbBi	Ta_2O_5	dc Disch	0.33	22.4	100	5%	55
TJ31F2[c]	PbBi	Ta_2O_5	dc Disch	0.33	19.3	100	3%	70
TJ31F3[c]	PbBi	Ta_2O_5	dc Disch	0.33	19.7	50	3%	72
TJ31F4[c]	PbBi	Ta_2O_5	dc Disch	0.33	14.6	50	3%	100

(a) at 80°C on a hot plate
(b) Niobium base electrode
(c) Niobium base electrode with 70Å Ta overlayer

This trend has been noticed by other workers [Raider, 1985] and is clearly related to the fact that the barrier thickness is approaching a few atoms, so that small defects will have a big effect. These problems can be quite subtle and complex and represent an interesting area of study in themselves. Clearly, the modern tools of surface science and well controlled epitaxial film growth should have a major impact on our understanding of such tunneling systems (see, for example Braginski, 1986).

Table 5-3 also lists the results for several niobium junctions and Ta overlayer on niobium junctions produced with the glow discharge oxidation. Clearly, the Ta overlayer on niobium improves the sharpness of the current rise at the sum gap. This is presumably due to the suppression of Nb suboxide formation at the interface as discussed in detail in section 5.5.3 for other overlayers such as Al, Mg, and rare earths. Fig. 5-18 shows that the voltage at which the current rise occurs for the Ta overlayer on Nb is lower than that for pure Nb in Fig. 5-17. The magnitude of this effect is consistent with the proximity effect model discussed in section 5.5.2 for a 70Å Ta overlayer on Niobium (see also Ruggiero et al., 1986a).

5.4.3 Gap Suppression at High Current Density

Most of the junctions with current densities greater than ~ $5x10^3$ A/cm^2 displayed a negative slope (dV/dI) at the sum gap. This effect was observed when the junctions were directly immersed in the superfluid helium bath at 1.3K. Similar effects have also been observed by a number of other authors [Yeh and Langenberg, 1978; Kleinsasser, 1981; Winkler and Claeson, 1985] using high current density junctions. These authors attribute the effect to the presence of excess quasiparticles which locally perturb the superconducting state and reduce the energy gap. In order to confirm that this effect is not simple self-heating (due to the heat generated by the simple I^2R dissipation), we have calculated the temperature rise caused by

the power dissipation in the junction. We include only the heat conduction through the metal film (an underestimate which ignores the substrate and LHe bath heat conduction) and calculate the temperature rise due to the junction dissipation. The junction in Fig. 5-12a, for example, generates an amount of power given by $Q' = (200\ \mu A)x(2\ mV) = 4$ nW at the sum gap. Using the thermal conductivity for Ta, $K_{Ta} \simeq 0.1$ W/cm [Rosenberg, 1955], a length of 10 μm from the small junction to the large (bulk) electrodes, and $Q' = KA\Delta T/d$, we find a temperature rise ΔT at the junction of $\sim$ 0.01K which is far less than necessary to cause the observed gap depression (a ΔT of at least 1K is required).

A more likely explanation of the observed gap depression, as mentioned above, is that it results from the injection of a large number of quasiparticles into a small area (and volume) of the superconductor which strongly perturbs the equilibrium superconductivity in this region. The negative resistance arises from the fact that as the current is increased, more quasiparticles are injected through the tunnel barrier and the energy gap is more strongly depressed. This depression of the energy gap for increasing current results in the negative differential resistance. The actual magnitude of the gap depression is of course strongly dependent on the geometry of the metal films in the junction area and their ability to remove the large number of injected quasiparticles and the subsequent phonons of energy $\sim 2\Delta$ due to pair formation (i.e. quasiparticle recombination). This in turn depends on such material specific parameters as the quasiparticle recombination lifetime and phonon scattering time [see Kaplan, 1976]. Rough estimates of the magnitude of these effects for parameters similar to ours [Yeh and Langenberg, 1978; Winkler and Claeson, 1985] show that the magnitude of the gap suppression that we observe is reasonable. In light of the uncertainty in the quasiparticle lifetimes, phonon conduction

at interfaces, and similar transport parameters for our system, these rough calculations are all that can be expected at this time.

These effects point out one of the limitations of the step defined geometry for higher current densities ($>10^4$ A/cm^2). Other geometries, such as the window geometry and the edge junction [Kleinsasser, 1981], offer more effective "cooling" of the junction area and allow higher (up to 10^5 A/cm^2) current densities before the non-equilibrium effects are seen. We note in passing that these gap suppression effects are the physical basis for some of the recent superconducting transistor concepts [Faris, 1983]. The response time of those devices is also limited by the quasiparticle recombination and phonon lifetimes.

5.4.4 Thermal Cycling and Aging Effects

All of the Ta and Nb base electrode junctions survived repeated thermal cycling from room temperature to 4.2K without failure due to shorts or open circuits. If the junction was kept under vacuum or in dry nitrogen during the time at room temperature, the resistance changes were always less than 1%. Exposure to air, however, caused a gradual increase in the junction resistance which is presumably due to additional oxidation at the edges of the junction. The effect of a hot plate anneal in air at 80°C is shown in Table 5-3. This effect is consistent with the work at IBM [Broom et al., 1980] where the resistance increase was attributed to lateral diffusion of oxygen or water vapor from the junction edges. This problem was solved by the IBM workers by using a PbAuIn alloy counter electrode. The In is believed to act as a passivating layer by forming an In_2O_3 layer on the surface of the counter electrode and preventing oxygen diffusion. The PbAuIn was not used in our case because the inclusion of the low T_c phase $AuPb_3$ at the junction interface can broaden the width of the current rise at the sum gap and increase the sub gap current [Lahiri et

Table 5-4 Summary of recent work by other authors on high current density junctions. The Nb and NbN results are at a bath temperature of 4.2K while all of the other results are for bath temperatures ≤2K.

Base electrode	Barrier	Counter-electrode	J_c (A/cm^2)	$I_{sg}/\Delta I$	ΔV (μV)	Reference
Nb	Al/Al_2O_3	Nb	6000	5%	~100	A
Nb	Al/Al_2O_3	Nb	1000	5%	≤100	B
Nb	NbO_xC_y	Nb	~1000	5%	≤100	C
Nb	NbO_xC_y	Nb	~1000	5%	≤100	D
NbN	MgO	NbN	1000	10%	~300	E
Sn	Sn-oxide	Sn	250	2%	40-50	F
PbBi	In/In-oxide	PbBi	250	1.5%	60	G
"	"	"	1000	5%	100	G
Ta	Ta_2O_5	PbBi	1000	1%	20	H

A - Huggins and Gurvitch, (1985)
B - Morohashi et al., (1985)
C - Gallagher et al., (1983)
D - Kleinsasser et al., (1981)
E - Shoji et al., (1987)
F - McGrath et al., (1981)
G - Gundlach et al., (1982)
H - This work (see Fig. 5-15)

al., 1980]. An evaporated SiO passivation layer may also be helpful in reducing the aging effects.

5.4.5 Comparison With Other Work on High Current Density Junctions

In order to put our work on high current density junctions in perspective, Table 5-4 compares the characteristics of junctions made with other processes by other researchers. For more details, Raider (1985) has reviewed recent progress on all refractory metal tunnel junctions. Only junctions with current densities ≥ 100 A/cm^2 have been considered. Our best Ta junctions at ~ 1000 A/cm^2, such as Fig. 5-15, have leakage currents that are <1% and have a width ΔV at the sum gap of ~ 25 μV which is a clear improvement on the results in Table 5-4. It is important to note, however, that the results in Table 5-4 for Nb and NbN junctions are only quoted for 4.2K operation. These results could improve at lower temperatures of ~ 1.3K. The best Sn junctions of McGrath et al., (1981), have produced excellent mixer results with conversion gain G > 1 and low noise (T_M = 9 ± 6K) approaching the quantum limit. These junctions, however, do not survive repeated thermal cycling. This was one of the major motivations for the work discussed in this thesis.

5.5 Mechanisms for "Non-Ideal" Tunnel Junctions

A number of physical characteristics of real tunnel junctions can conspire to produce I-V curves that deviate from the ideal BCS I-V discussed in chapter II. Real tunnel junctions, for example, use tunnel barriers that vary in thickness, have defects and electron traps, and do not always form a sharp metal to insulator interface. Real metal films often have grain boundaries unless an effort is made to produce single crystal films in UHV on high temperature substrates. These grain boundaries can contain impurities which may locally reduce the energy gap through the

proximity effect. These effects are enhanced in superconductors with short coherence lengths such as Nb and Ta ($\xi \simeq 200$Å). Many superconductors such as Pb also have an energy gap that is different in different crystallographic directions which can lead to a width of the current rise at the sum gap for polycrystalline films. A brief description of these important mechanisms and their experimental relevance is given in the following sections.

5.5.1 Multiparticle Tunneling

As the name implies, multiparticle tunneling (MPT) is a process by which m particles (two or more) can tunnel at the same time through the barrier. This process was first described by Schrieffer and Wilkins (1963)(see also Wilkins, 1969; Hasselberg et al., 1974; and Mukhopadhyay, 1979) and is simply a higher-order tunneling process of expected rate $|T|^{2m}$, where T is the tunneling matrix element. This theory predicts a current rise at the m-particle threshold $eV = 2\Delta/m$ of,

$$\Delta J_m = \frac{e\Delta}{4\pi\hbar d^2} \tanh\left[\frac{\Delta}{2kT}\right]\left[\frac{e^{-s}}{16}\right]^m (s + m^{-1})\left[\left[\frac{2}{m!}\right]\left[\frac{m}{2}\right]^m\right]^2 \qquad 5\text{-}4$$

where $s = 2\kappa d = 1.025\, d\phi^{1/2}$, with d the oxide thickness in Å and ϕ the barrier height in eV. This relation predicts that the current jumps fall off rapidly with increasing m proportional to $\simeq \exp(-ms)$. From the barrier studies in section 5.3.1 we know that $d \simeq 15$ Å and $\phi \simeq 1$eV which implies that $s \simeq 15$. If this value of s is used to calculate the ratio of the current rise at the m=2 multiparticle tunneling steps ($V = \Delta_1/e$ or Δ_2/e) to the current rise at the sum-gap (m=1) we find $\Delta I(m=2)/\Delta I(m=1) \simeq \exp(-s) \simeq 3\times10^{-7}$. As discussed in section 5.3 and 5.4 and shown in Fig. 5-9, we typically find a current rise at Δ_1 or Δ_2 which is about 100 to 1000 times

smaller than the current rise at the sum gap. This experimental value for the current ratio is at least a factor of 1000 times greater than what is predicted by the multiparticle tunneling model. One possible way to account for this discrepancy within the model is to assume that the oxide is non-uniform and that the strong multiparticle currents come from the locally thin areas. If, for example, 15% of the single particle current comes from an area of the junction with a barrier thickness of 5Å then we find $\Delta I(m=2)/\Delta I(m=1) \simeq 10^{-3}$ which is closer to the experiment. Similar comparisons have been made for subgap currents in small Nb junctions produced at IBM by Gallagher et al. (1983). It should be noted, however, that the theory becomes questionable for such very thin (<10Å) barrier regions where the coupling of the electrodes is strong. This breakdown occurs because the theory is based on a perturbation calculation that is not valid when the matrix elements become of order unity as required for strong coupling. Recent progress on the problem of strong electrode coupling has been made by Arnold (1985) and Klapwijk, Blonder and Tinkham (1982) although the connection with multiparticle tunneling is not clearly resolved at this time.

An additional prediction of the multiparticle tunneling model that is easily checked is the ratio of the m=2 current jumps at Δ_1 and Δ_2. The theory predicts that $I(\Delta_1)/I(\Delta_2) = \Delta_1/\Delta_2 = 0.4$ for $Ta/Pb_{0.9}Bi_{0.1}$ while the data in Fig. 5-9 gives a ratio of $\simeq 0.1$. This value is significantly smaller than the theoretical prediction as are the ratios for the other I-V's in Table 5-1 and 5-2. This observation may be related to strong electrode coupling through the barrier mentioned above or the presence of additional mechanisms discussed below.

5.5.2 Proximity Effect Tunneling

A proximity effect tunneling structure is shown schematically in Fig.

5-19a. The N layer can be a normal metal or a superconductor with a reduced energy gap. In both cases the N layer is assumed to be thin compared to the coherence length in the proximity layer $d_N < \xi = \hbar v_{FN}/\pi\Delta_S$. The strong interaction of this N layer with the superconductor S induces a gap Δ_N in the N layer by the well known proximity effect [Deutscher and DeGennes, 1969; Wolf, 1985]. A small reduction of Δ_S also occurs at the NS interface, but this effect is usually <3% for thin N layers [Arnold, 1978]. This structure can represent the real situation in a tunnel junction if the metal/barrier interface is damaged (the damaged layer would look like a reduced T_c superconductor) and has a reduced energy gap or if a thin metal layer such as Al or Ta has been deposited on the surface to be oxidized as an artificial tunnel barrier (see sections 5.4 and 4.2.5). The theory of tunneling into proximity effect systems has developed significantly in recent years and has been recently reviewed by Wolf, 1985. The theory itself makes use of Green's function techniques which are quite involved and beyond the scope of this thesis to discuss in detail. Nonetheless, some of the salient features and their relevance to experiments are discussed below.

The basic physics of proximity effect tunneling is indicated in Fig. 5-19b and 5-19c, where the thick S layer has induced an energy gap Δ_N in the N layer. This square well potential at the tunnel junction interface produces at least one quasiparticle bound state of energy E_0 just below the energy gap Δ_S. A straightforward calculation (solving for the wavefunction in the potential well with $\Delta_N = 0$) by de Gennes and Saint-James (1963) finds the bound state energy E_0 to be given by,

$$E_o = \Delta_S[1 - (d_N\Delta_S/2\hbar v_F)^2] \qquad 5\text{-}5$$

$$= \Delta_S[1 - (d_N/2\pi\xi)^2] \qquad 5\text{-}6$$

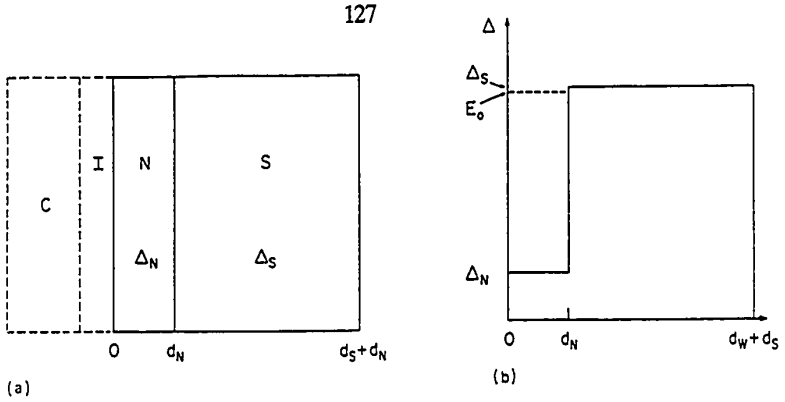

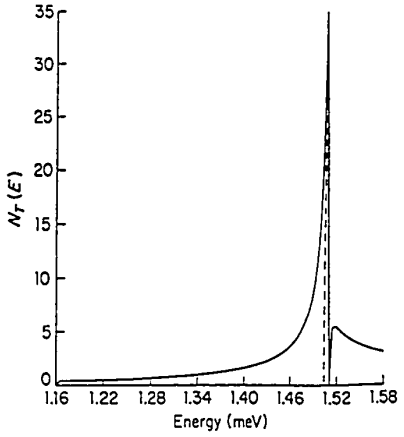

Fig. 5-19: (a) Schematic of the proximity effect tunneling geometry (b) the resultant energy levels and (c) the tunneling density of states (from Wolf, 1985).

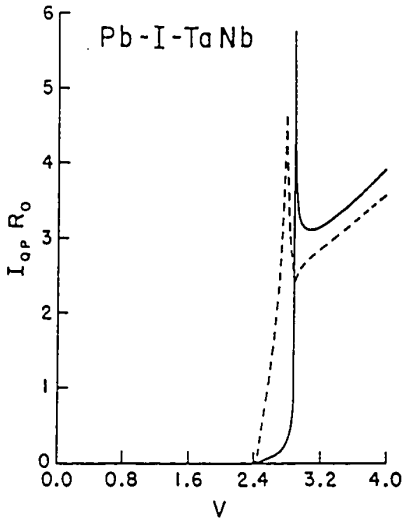

Fig. 5-20: Calculated I-V curve for a Pb-I-Ta(overlayer)Nb tunnel junction (from Arnold, 1985). Solid curve is for $R(=2d_{Ta}/\hbar v_{FTa})$ = 0.03, dashed curve is for R = 0.5.

Note that E_0 reduces to Δ_S for very thin N layers as one would expect in this limit. A more complete analysis (including strong coupling effects and scattering) by Arnold, (1978) (see also [Wolf and Arnold, 1982]) shows that E_0 is given approximately by,

$$E_o = \Delta_S[1 - (RZ\Delta_S/4)^2] \qquad 5\text{-}7$$

where

$$R = \frac{2Zd_N(1+r)}{\hbar v_F(1-r)} \qquad 5\text{-}8$$

and

$$r = \left| \frac{v_F(S) - v_F(N)}{v_F(S) + v_F(N)} \right| . \qquad 5\text{-}9$$

Z is approximately equal to $1 + \lambda \simeq 1$ where λ is the electron phonon coupling constant ($\lambda = N(0)\langle I\rangle^2/M\langle\omega^2\rangle$ [McMillan, 1968]) which is usually in the range $0 < \lambda < 1$. r is a measure of the reflection off the small potential step associated the difference in the Fermi wavevectors of N and S. For typical values of $r \simeq 0.1$, $Z = 1$, $d_N = 0.3\xi \simeq 30$ Å we find $E_0 \simeq 0.99\Delta_S$. Arnold also calculates the tunneling density of states for this system with strong electron-phonon coupling effects from which dc I-V curves are easily derived as shown in Fig. 5-20. The essential characteristic of the proximity effect I-V curve is an abrupt current rise at the voltage $\Delta_1 + E_0 < \Delta_1 + \Delta_2$ where the quasiparticles begin to tunnel into the bound state energy level at E_0. A negative resistance region between $\Delta_1 + E_0$ and $\Delta_1 + \Delta_2$ is also predicted. A beautiful experimental example

of these effects is provided by the work of Gurvitch et al. (1981) in Fig. 5-21 where a series of Al layer thicknesses are deposited on the surface of a Nb base electrode and oxidized to form an Al_2O_3 tunnel barrier. The remaining Al between the barrier and the Nb forms the N layer discussed above. The exact N layer thickness after oxidation in this case is not very well known because some of the Al was found to diffuse down the Nb grain boundaries. Nonetheless these I-V's clearly demonstrate the proximity effect and the advantages of having a high quality barrier to metal interface as discussed further in 5.5.3. The exact details of the tunneling density of states and the predicted dc I-V curve will of course be strongly dependent on the nature of the NS system being modeled. For example, one needs to have a good estimate of the coherence length, the N layer thickness (assuming no thickness variations), and the scattering properties of the interface [see, for example, Ruggiero et al., 1986a]. Unless a system is intentionally prepared with a well known N layer this modeling can be difficult. The important point here is that tunneling into a proximity effect system can produce I-V curves with significant conduction below the sum-gap and a negative or increased resistance region above the sharp current rise at $E_0 + \Delta_1$. Both of these effects are observed experimentally in sections 5.3 and 5.4.

5.5.3 Suboxides and Normal Metal Inclusions

The interface between a metal and an insulator generally contains defects and composition variations. A special effort is required to avoid this by growing an epitaxial insulator on a single crystal metal which is seldom possible for tunnel junctions. Even then, a certain level of defects and insulator cracks will always be present. The presence of defects and their electrical properties are especially important for the disordered oxide tunnel barriers and interfaces being discussed in this chapter.

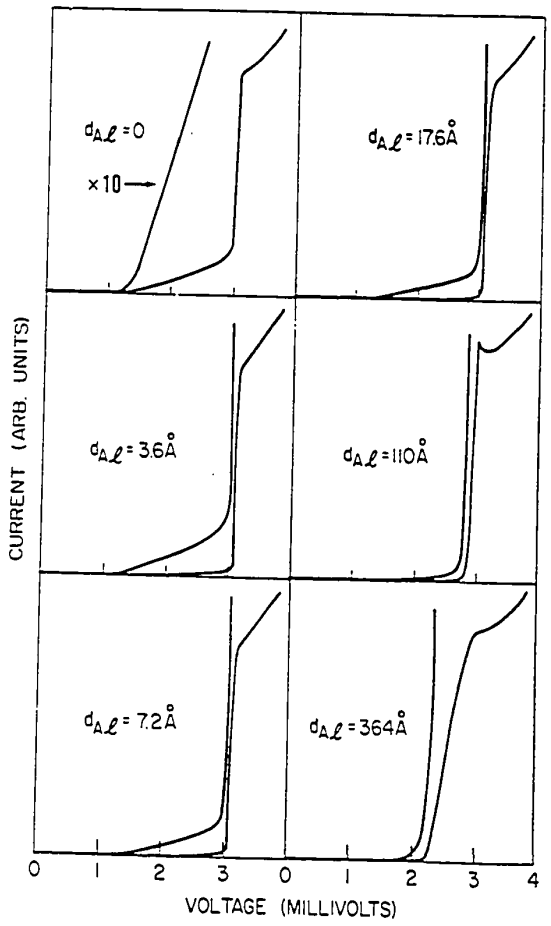

Fig. 5-21: High quality I-V's obtained by Gurvitch et al. for varying Al overlayer thicknesses in large area Nb/PbBi tunnel junctions. Note the clear demonstration of the proximity effect "knee" which moves to lower and lower energy as the Al overlayer thickness is increased [from Gurvitch et al., 1981].

As illustrated schematically in Fig. 5-22, Nb is a classic example of the problems associated with oxidizing a metal that forms multiple stable oxides (suboxides) such as NbO and NbO_2 [Samsonov, 1982; Halbritter, 1985]. In the case of niobium, NbO is actually a low T_c (~ 1K) superconductor which means that small inclusions of this suboxide (at grain boundaries for instance) may locally depress the gap and give rise to currents that flow below the gap of bulk clean Nb. Oxygen in solid solution is also well known to strongly depress the T_c of bulk Nb (~ 1K/at.%) [Koch et al., 1974] so that oxygen diffusion into Nb at the interface may also cause local depression of the energy gap. Recent studies of high quality Nb junctions at IBM [Kuan et al., 1982] show that a thin NbO_xC_y layer on the Nb surface can improve junction quality by acting as a barrier against the diffusion of oxygen into the Nb at the surface. Additional studies by Kwo et al. (1983) using oxidized rare earth and Mg overlayers on Nb, show that increased subgap leakage is strongly correlated with presence of Nb suboxide (NbO) at the interface (as determined by XPS). Recent studies of single crystal Nb films by Celaschi et al., (1983), show that the oxidation of single crystal Nb films is quite different from that of polycrystalline Nb. In particular, the single crystal Nb was found to produce high quality barriers with low subgap leakage and a large barrier height ($\phi \simeq 0.7$ eV). The I-V's also showed no proximity effect "knee" structure at the sum gap. These studies emphasize the importance of grain boundary effects in the oxidation of Nb and the incompleteness of our present understanding of the details of thin film oxidation.

As originally discussed by Shen (1972), Ta presents a very different situation from Nb in that it forms high quality barriers with simple air oxidation. A large amount of evidence suggests that this is mostly due to the lack of stable Ta suboxides [Samsonov, 1982] which leads to a sharp metal to Ta interface. Himpsel et al. (1984) have used core level shifts in

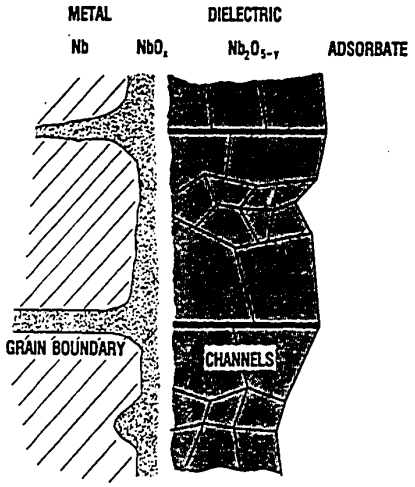

Fig. 5-22: Schematic representation of the Nb/Nb-oxide interface [from Halbritter, 1985].

XPS (X-Ray Photoelectron Spectroscopy) to study the surface oxidation of Ta in UHV. These authors find that Ta is only oxidized in the 3+ (Ta_2O_3) or 5+ (Ta_2O_5) valence state with no evidence for TaO (2+ valence). The electrical properties of Ta_2O_3 are not known since it does not form a stable bulk crystal. The exact amount of Ta_2O_3 may also depend on the oxidation technique so that these result should only be used as a guide. These XPS studies are in sharp contrast to similar work on the Nb/Nb-oxide system [Pollak et al., 1983] where many valence states of Nb are seen. Sputter profiles of anodized Ta and Nb films also reveal a much sharper interface for Ta/Ta_2O_5 than for Nb/Nb_2O_5 [Sasaki, 1980]. This indicates a reduced tendency for oxygen to diffuse into Ta and locally depress the energy gap as is found in Nb. The lack of a proximity effect "knee" structure in most of the very high quality Ta junctions in this chapter also supports the idea of a sharp Ta/Ta_2O_5 interface.

5.5.4 Resonant Tunneling and Barrier Defects

Most tunnel barriers have an inherent number of defects due to vacancies and impurities. These defects can produce states in the band gap of the insulator (tunnel barrier) and additional conduction mechanisms besides direct tunneling which can lead to increased subgap leakage current. Resonant tunneling is one such example that has been extensively discussed by Halbritter (1985). In this case an electron has an enhanced probability for tunneling through an empty (resonant) state in the band gap of the insulator when its energy is properly lined up with the energy levels in the left and right electrodes. Hopping conduction may also be possible for certain defect energy levels. The loss of energy information in the hopping process may also allow current to flow for voltages less than the sum gap. Neither resonant tunneling or hopping conduction have been directly correlated with subgap leakage current at this time (to my knowledge) so

that the above statements should be regarded as speculative. A low density of electron traps is found for many Ta_2O_5 thin films by optical means [Thomas, 1974; Seki, 1983]. This is probably related to the high quality junctions that we have been able to produce with Ta base electrodes although the direct connection is not clear at this time.

5.5.5 Gap Anisotropy

As discussed in chapter II, tunnel junctions can measure a superconducting energy gap which depends on the crystallographic orientation. For example, Pb single crystals have been measured by Rochlin, (1967) to have an energy gap of Δ = 1.49 mV in the 100 direction and Δ = 1.25 mV in the 110 direction. Other orientations give intermediate values of Δ. In polycrystalline films, such as those discussed in this thesis, variations in the crystal strain and microcrystalline orientation can cause a distribution of energy gaps to be measured by a tunnel junction that is physically larger than the grain size. We believe that this is the cause of the broad (200 μV) current rise always found with pure Pb counter-electrodes discussed in section 5.3. Markowitz and Kadanoff, (1963), have pointed out that impurity scattering can reduce the size of these effects by causing electron scattering to different portions of the Fermi surface, thus averaging the anisotropic properties [see also Campbell et al., 1966]. These Fermi surface averaging effects are important in dirty superconductors where the mean free path ℓ is less than the Pippard coherence length ξ_o (e.g. PbBi where $\xi_o \simeq$ 1000 Å and $\ell <$ 100 Å). Dirty superconductors such as PbBi show only one well defined value of Δ in all of the tunneling experiments to date [Dynes et al., 1978]. This was a major reason for our using an alloy such as $Pb_{0.9}Bi_{0.1}$ as a counter-electrode material for mixer junctions needing a sharp current rise at the sum gap. The mean free path in our Nb and Ta

films is also quite short ($\simeq$ 100 Å $\simeq$ grain size) which should average any anisotropy effects in these materials as well [Durbin et al., 1983].

5.5.6 Quasiparticle Lifetime Effects

As discussed in chapter II, the lifetime of quasiparticles near the superconducting energy gap Δ is determined by the time it takes to find another quasiparticle of equal and opposite momentum. These quasiparticles can then recombine to form a cooper pair and emit a phonon of energy 2Δ in the process. This quasiparticle recombination lifetime is strongly temperature dependent and is given by,

$$\frac{1}{\tau_r} \propto (\pi)^{1/2}\left[\frac{2\Delta(0)}{kT_c}\right]^{5/2}\left[\frac{T}{T_c}\right]^{1/2}\frac{1}{\tau_o}\, e^{-\Delta/kT} \qquad 5\text{-}10$$

where τ_o is related to the electron-phonon coupling strength λ through the Eliashberg theory as discussed in chapter II. The strong temperature dependence comes from exponential decrease in the number of available quasiparticles as the temperature is decreased. Values of τ_o have been calculated for various materials by Kaplan et al. (1976) (τ_o = 0.196 x 10^{-9} sec for Pb; = 1.78 x 10^{-9} sec for Ta; = 0.149 x 10^{-9} sec for Nb; and = 0.043 x 10^{-9} for $Pb_{0.9}Bi_{0.1}$). For Pb, excellent experimental agreement has been obtained by Hu et al. (1977).

As first demonstrated by Dynes et al. (1977) for $Pb_{0.9}Bi_{0.1}$, the quasiparticle lifetime can have a significant effect on the width of the current rise at the sum gap. Fig. 5-23 shows the temperature dependent I-V curves measured by these authors. The temperature dependent gap width is well fit by assuming that the temperature dependent lifetime broadening given by Eq. 5-10 ($\tau_R = \Delta E/\hbar$) with a τ_o given by the calculations of Kaplan et al. (1976).

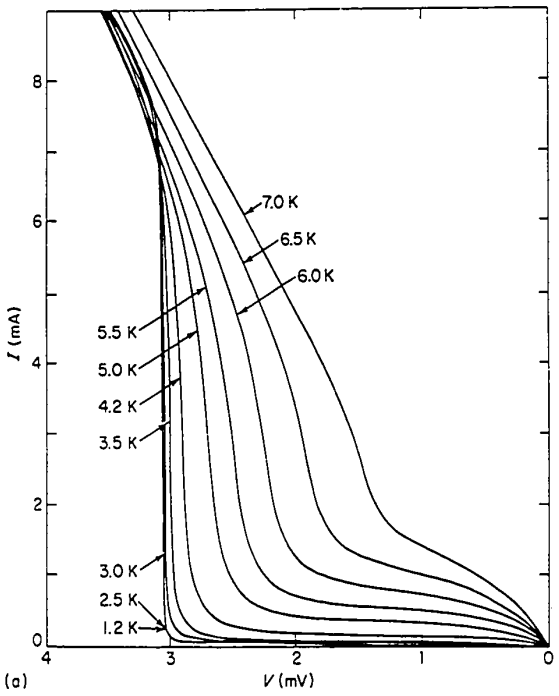

Fig. 5-23: I-V curve for a $Pb_{0.9}Bi_{0.1}/I/Pb_{0.9}Bi_{0.1}$ tunnel junction as function of temperature showing the gap broadening due to the short quasiparticle lifetime near T_c [from Dynes et al., 1978].

Fortunately for the application of quasiparticle mixers, this lifetime broadening becomes small at low temperatures ($T<0.3T_c$) and is not a real problem for most materials which have a τ_0 much larger than that of $Pb_{0.9}Bi_{0.1}$. The $Nb/Pb_{0.9}Bi_{0.1}$ mixer experiment at 4.2K discussed in chapter VI, however, does have a significant width at the sum gap due to the quasiparticle lifetime of the $Pb_{0.9}Bi_{0.1}$ counter-electrode. This width is seen to have a strong effect on the conversion efficiency of the mixer which makes a useful test of these results.

5.6 Conclusions

The small area Ta junction characteristics described in this chapter are nearly ideal for the SIS mixer experiments to be discussed in chapter VI. Nb junctions fabricated with the same process have less ideal characteristics, but can be improved with the use of a thin Ta overlayer. A number of mechanisms that can contribute to non-ideal junction characteristics have also been identified. The effect of these mechanisms on tunnel junction I-V's has also been compared with the Ta and Nb junction results. Several challenges remain, however, such as the elimination of the aging problem (junction resistance increases with air exposure) and the reduction of the junction area for higher frequency applications. An improved understanding of the microscopic mechanisms that contribute to non-ideal junction behavior at high current density is also clearly needed.

VI. ACCURATE MIXER MEASUREMENTS AT UC BERKELEY

This chapter describes a series of mixer measurements with the Ta and Nb junctions which were carried out in collaboration with W.R. McGrath and P.L. Richards at the University of California at Berkeley. The unique apparatus used for these experiments was specifically designed and built by the Berkeley group for making accurate gain and noise measurements near the quantum limit, and represents a significant experimental achievement in itself. This apparatus is capable of making noise temperature measurements with an accuracy of better than ± 1K. This is a factor of six improvement over previous measurements [McGrath et al., 1981]. Gain can also be measured accurately, to ± 5%. One of the primary purposes of these measurements is to make quantitative comparisons with the noise predictions of the quantum mixer theory when the noise approaches the quantum limit. This required the combination of two important experimental achievements; 1) a small-area high-current density tunnel junction with a low subgap current ("leakage") and a "sharp" current rise at the sum gap, as described in chapter V and, 2) a well characterized and accurate noise measurement system such as the one described in this chapter.

The measurements in this chapter show the dependence of mixer gain and noise on the I-V "sharpness", subgap ("leakage") current, and rf coupling of the junction. We find that the mixer noise is reasonably well predicted by the theory as discussed in chapter VII, but that the theoretical predictions for the gain are only accurate for junctions with rounded I-V's, having low gain. We also find that the achievement of large or infinite gain is strongly dependent on the rf coupling. In particular, the narrow-band coupling of our mixer block only allows large gain ($G >> 1$) with a low (< 50 MHz) IF frequency. The larger IF of 1.5 GHz produces $G \simeq 1$ which is lower than expected but still much higher than most SIS mixers

reported in the literature [Tucker and Feldman, 1985]. The large IF of 1.5 GHz is desirable for most applications and was well suited to the accurate noise measurement techniques discussed in this chapter.

6.1 Measurement Apparatus and Techniques

The measurement system discussed in this section was designed and built by W.R. McGrath and P.L. Richards and has been previously described [McGrath et al., 1985, and McGrath, 1985]. It is presented here for completeness and ease of discussion in later sections. As shown in Fig. 6-1, this apparatus employs variable temperature cryogenic loads T_1 and T_2 as calibrated noise sources at the rf input and IF output of the mixer. The basic technique of using hot/cold loads is not new [Blaney, 1980], but the implementation at LHe temperatures to produce well calibrated noise powers near the quantum limit is a new development. The various components of the apparatus and the measurement technique will be discussed individually below.

6.1.1 Variable-Temperature Waveguide Load

The noise source T_1 is of special design [McGrath, 1985] and consists of a 0.25 mm thick silicon vane inserted through a narrow slot in the broad wall of an OFHC copper waveguide as shown in Fig. 6-2. The vane is a section of a standard 2 inch silicon wafer with an evaporated NiCr film to provide a resistive absorbing film. The sheet resistance of the NiCr film is 200-400 Ω/□. The gradual taper of the wafer in the waveguide provides a nearly perfect absorber and therefore a nearly perfect blackbody radiator. Reflection measurements at 36 GHz give an attenuation of more than 30 dB and an input VSWR of < 1.16. These measurements imply an emissivity very close to unity (0.999). A thin (0.002 inch) mylar window across the output of the waveguide in Fig. 6-2 allows the thermal radiation to be coupled out

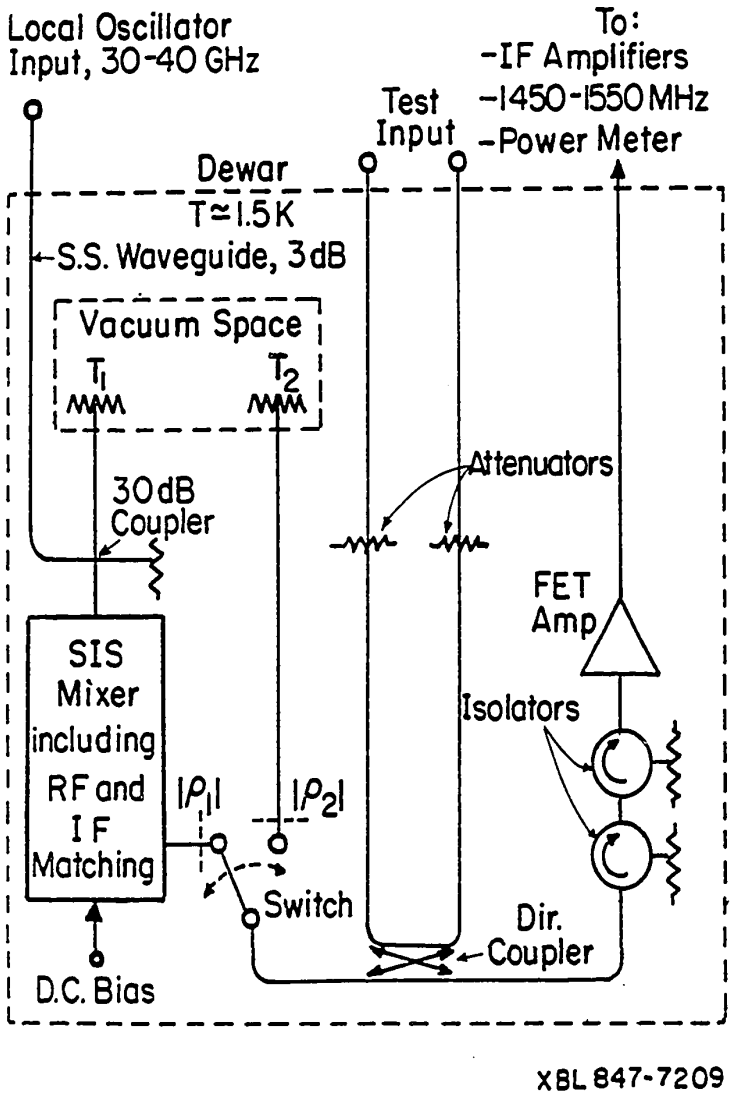

Fig. 6-1 Block diagram of the system for measuring noise temperature and conversion gain of SIS mixers. Variable temperature loads are used to produce calibrated signals for inputs to both the mixer and the IF system. (From McGrath et al., 1985).

while still maintaining a vacuum around the radiation source. A small amount of activated charcoal (with a high surface area) placed in the vacuum space helps to cryopump any He that leaks through the window.

Special care was also taken in the thermal design to insure a uniform temperature of the vane and a reasonable (≈ 10 sec) time constant at LHe temperatures. The vane temperature was measured with a calibrated four wire germanium resistance thermometer[1] and was varied with 1kΩ metal film resistor (heater). In order to accurately measure the silicon vane temperature, the electrical connections to the thermometer were made with low thermal conductivity manganin wire to insure that the thermometer was isolated from external sources of heat. The manganin wires were well heat sunk to the bath temperature before being connected to the thermometer.

6.1.2 Variable-Temperature Coaxial Transmission Line Load

The calibrated noise source for the IF consists of a thick-film chip resistor[2] connected between the inner and outer conductor of a 0.085 inch diameter rigid coaxial line as shown in Fig. 6-3. Both the inner and outer conductors are made of stainless steel. The return loss from this load was measured during each experimental run and was always greater than 18 dB for measurements discussed in the next sections. This indicates that the load is well matched to the line and is a good blackbody radiator. As with the rf load, the thermal design of the IF load required special considerations to insure accurate temperature and noise power measurements. The low thermal conductance of the 3 cm long section of stainless steel coaxial line allowed for good thermal isolation of the IF load from the bath and an acceptably low loss of ≈ 0.15 dB at 1.5 GHz. A careful calibration of the

---

[1] Cryocal Inc., St. Paul, MN 55114

[2] State of the Art, Inc., State College, PA

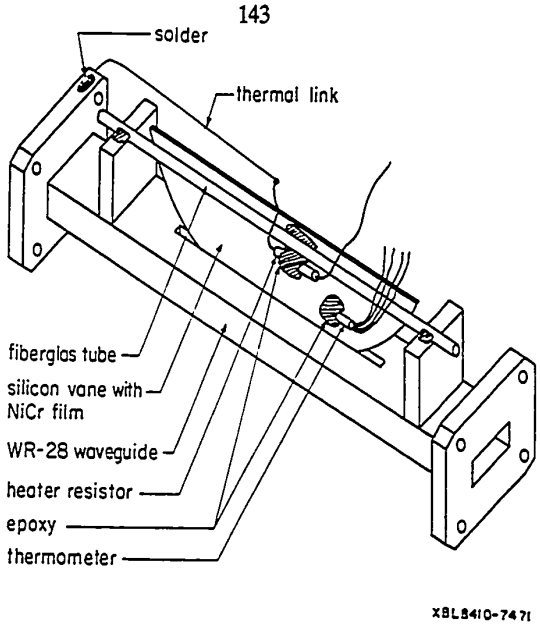

Fig. 6-2 Variable temperature rf load T_1 for producing calibrated input powers to the mixer. (From McGrath et al., 1986)

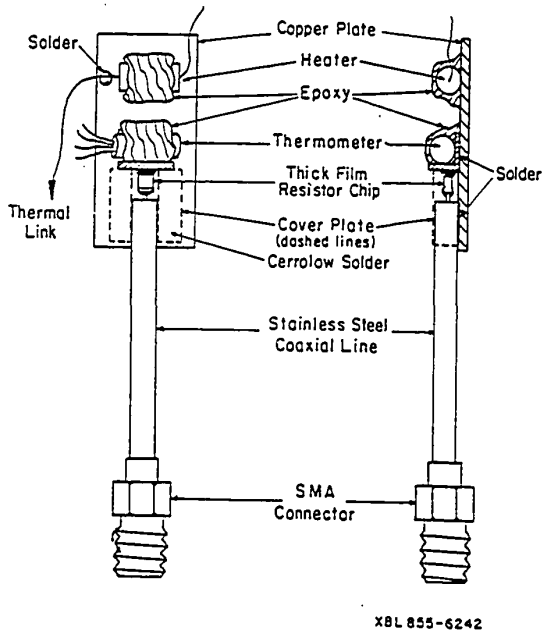

Fig. 6-3 Variable temperature IF load T_2 for producing calibrated noise powers at the IF. (From McGrath et al., 1986)

noise power from this load arrangement showed that the noise power from the chip resistor was given by the thermometer temperature to an accuracy of ±3% at 100 Hz.

6.1.3 Cooled IF Amplifier and Isolators

Another important component in Fig. 6-1 is the cooled GaAs FET amplifier for the mixer IF output at 1.5 GHz. This state of the art amplifier has an input noise temperature of ~ 14K at 1.5 GHz and was designed and specially built for these types of low noise applications by S. Weinreb [Weinreb, 1982]. Since the noise temperature of the IF amplifier depends on the impedance that is presented at its input, two 20 dB cooled isolators are also added between the mixer and the IF amplifier to insure that the impedance seen by the IF amplifier input (and therefore its noise) is independent of the mixer output impedance. The corrections for the loss and noise of these components are presented in section 6.1.5. The availability of a well characterized low noise IF amplifier and reasonably compact IF isolators (unlike the bulky isolators at low (< 1 GHz) frequency) are two of the most important reasons for choosing an IF of 1.5 GHz for making accurate noise measurements.

6.1.4 Mixer Block and RF Tuning

The mixer block used in these experiments has been previously described [Richards, et al., 1979; Shen, et al., 1980]. This block uses a screw tuner and a sliding backshort to obtain rf matching and is shown in Fig. 7-5b. Recent scale model measurements [Raisanen et el., 1985] show that this arrangement can provide a wide range of desirable impedances for rf matching to SIS mixers. (These rf impedances {=[admittance]$^{-1}$} enter as admittances, Y_m, into the mixer model discussed in section 2.3.2.) These rf impedances have a strong frequency dependence, however, which means that

a constant rf impedance can only be provided over a narrow instantaneous bandwidth. With large IF frequencies (f > 100 MHz), the narrow bandwidth results in unequal impedances in the image and signal frequency bands. (If the signal frequency is given by $\omega_S = \omega_{LO} + \omega_{IF}$ then the image frequency is given by $\omega_{image} = \omega_{LO} - \omega_{IF}$ or vice versa.) This produces single sideband (SSB) mixer operation. The importance of this effect is demonstrated in this chapter with large IF (1.5 GHz) and low IF (25 MHz) measurements. These measurements and the theoretical modeling in chapter VII show that large gain is more readily obtained with broad-band rf coupling where the image and signal see the same impedance. This evidence provides additional motivation for the development of broad-band matching techniques [Raisanen et al., 1985].

6.1.5 Accurate Gain and Noise Measurement

As also used by McGrath, (1985), the word mixer refers to the mixer block which contains the junction (pumped by a local oscillator), screw-tuner, backshort, rf choke, and the IF matching transformer. T_1 supplies a calibrated input signal power of P_1 to the mixer, and T_2 is heated to produce a power P_2 equal to the mixer IF output. Under these conditions, the relationship between P_1 and P_2 is ideally

$$P_1 = P_2/G_C - P_M \qquad 6\text{-}1$$

where G_C is the coupled mixer gain and P_M is the mixer noise power referred to the input of the mixer (see chapter II). The powers P_1 and P_2 are calculated from the physical temperatures T_1 and T_2 of the hot/cold loads discussed above using the Planck radiation formula,

$$P_M = \frac{\hbar\omega\ B}{\exp(\hbar\omega/kT_M) - 1} \qquad 6\text{-}2$$

where B is the limiting bandwidth of the IF system. In our experiments, G_C and P_M/B are determined by plotting P_1/B versus P_2/B for several pairs of data points which means that the bandwidth need not actually be measured. Coupled gain G_C is converted to available gain G_A by measuring the power reflection coefficient $|\rho_1|^2$ at the output of the mixer as indicated in Fig. 6-1 and discussed in chapter II ($G_C = G_A(1 - |\rho_1|^2)$.

Equations 6-1 and 6-2 provide a satisfactory definition of the noise power of the mixer, as defined above, only if a number of detailed conditions are met. The reflections and losses in all of the components were evaluated with great care and several corrections to Eqs. 6-1 and 6-2 were found to be necessary. These are for the loss L between the load T_1 and the mixer, for reflections at the output of the mixer and the load T_2, for the thermal noise from the local oscillator waveguide loss, and the isolator termination. Including these corrections McGrath et al., (1985), obtain:

$$P_1 = \frac{P_2}{G_{C'}} - P_{M'} \ , \qquad 6\text{-}3$$

where

$$G_{C'} = \frac{G_C}{L(1 - |\rho_2|^2)} \ , \qquad 6\text{-}4$$

and

$$P_{M'} = L\left[P_M + \Delta P_A - \frac{(|\rho_2|^2 - |\rho_1|^2)\ P_b + \Delta P_{IF}}{G_C} \right]. \qquad 6\text{-}5$$

Each experimental mixer run measures $G_{C'}$, $|\rho_1|^2$, $|\rho_2|^2$, and $P_{M'}$. The

other factors in Eqs. 6-3 to 6-5 are constant and discussed below.

For our Ka-band system the loss between noise source T_1 and the mixer is L = 0.16 ± 0.05 dB. Matching transformers are used which insure that the amplitude reflection coefficient at the output of the mixer is $|\rho_1|$ < 0.5. The analogous coefficient for the IF load is $|\rho_2|$ < 0.13. Both $|\rho_1|^2$ and $|\rho_2|^2$ are determined for each mixer measurement by using the directional coupler in Fig. 6-1 to inject a test signal and measure the ratio of reflected to incident power ($|\rho|^2$ = P(reflected)/P(incident)). The thermal noise from the L0 waveguide attenuated by the 30 dB cross-guide coupler and the noise contribution from the loss L combine to give ΔP_A. Expressed as a temperature, this term is ΔT_A = 0.19 ± 0.04 K. The noise power P_b from the cooled terminations of the IF isolators is computed from the LHe bath temperature of ≃ 1.5K. The change in IF system noise ΔP_{IF} when the switch goes from the noise source T_2 to the mixer output is computed using the above values of $|\rho_1|$ and $|\rho_2|$ and 40 dB of isolation. When expressed as a temperature we find $|\Delta T_{IF}|$ < 0.05 K [Weinreb, 1982]. Since the phases of ρ_1 and ρ_2 are unknown, the sign of ΔT_{IF} cannot be determined. The magnitude of this term is included in the error. The only additional noise source which might contribute is the noise from the local oscillator which is discussed in the next section. All other losses and reflections are expected to be negligible.

The receiver noise temperature referred to the low temperature rf input is easily determined by measuring the total IF output noise power versus the input noise power from the rf load and extrapolating to zero IF output noise power. T_R represents the physical temperature of T_1 required to double the IF output noise of the system. Unlike T_M, the receiver noise includes all of the system losses, impedance mismatches, and IF system noise temperature T_{IF} ≃14-18K. An example of this technique is shown in Fig. 6-6 for a niobium junction at two different bath temperatures.

6.1.6 Local Oscillator Noise

The signal to noise ratio for klystrons is typically 170 dB in a 1Hz bandwidth at 1.5 GHz from the operating frequency [Ediss et al., 1982] which gives a very small (insignificant) added noise at the junction of less than 0.007K for an LO power of 10 nW. This is a typical LO power level for a well matched junction. For poorly matched junctions, however, much larger LO powers approaching 1 to 10 μW are required. These large LO powers can cause the LO noise to become significant ($T_{LO} \simeq .7K$ to 7K). This possible source of noise has only recently been appreciated for our measurements. For this reason, no prior attempt was made to directly measure the LO noise in our experiments. In order to make an estimate of the LO noise we note that a Pb-alloy junction array measured by McGrath et al., 1985, in the same system with an LO power of ~ 500 μW gave a mixer noise temperature of ~ 10K. If, in the worst case, all of the mixer noise could be attributed to LO noise, this would imply a maximum LO noise for the Ta experiments of $T_{LO} \simeq 0.05K$ where the maximum LO power used was $\simeq 2.3$ μW. It should be possible to eliminate this concern in future experiments with the appropriate band pass filters on the LO [Ediss et al., 1982].

6.1.7 Optimization of Mixer Performance

Before performing accurate measurements with the techniques discussed above, a monochromatic signal from a Gunn oscillator is used to optimize the mixer for the largest coupled gain on a particular photon step. This procedure requires a systematic variation of the LO power, backshort position, and screwtuner position to find the optimum conditions. A careful and systematic optimization generally requires about two hours if nothing is known about the junction or matching beforehand. This lengthy procedure

is required to insure that the best overall performance is found and that it is unique. This optimization was followed for all of the experiments discussed below and always gave a unique optimum for each photon step. Once the general range of tuning and LO power are known, however, the mixer output can be easily optimized in less than 15 minutes.

The monochromatic signal is also used to measure the mixer gain to an accuracy of ±1 dB. This measurement of gain is always compared with the gain determined by the hot/cold loads to make sure that they agree within ±1 dB. By adjusting the frequency of the monochromatic signal to be equal to the image frequency, the gain in the unoptimized sideband is also measured. The ratio of the gain at the signal frequency to the gain at the image frequency is referred to as the sideband ratio. For all of the experiments at 1.5 GHz IF discussed below, the sideband ratio was > 18 dB.

6.1.8 Low IF Apparatus

This section describes the modification of the 1.5 GHz apparatus discussed above in order make low IF measurements. This modification was made in order to look for large gain with low IF's as discussed in section 6.6. The low noise GaAs amplifier and subsequent amplification stages were replaced with a series of high quality room temperature amplifiers. The first and most important of these was a MITEQ[3] model# AU-3A-0150 with a calibrated gain of 46 dB from 1 to 500 MHz and a noise figure of ≃ 1.5 dB (T_{IF} ≃ 125K). This was followed by two HP 8447 amplifiers with a gain of 20 dB for each. Each stage was isolated from the next with 3 dB attenuators to insure against reflections and standing wave effects. The input to the first stage (MITEQ) also had a 3 dB attenuator although it could usually be eliminated without any adverse effect in order to decrease the

---

[3] MITEQ Inc., 100 Ricefield Lane, Hauppauge, NY 11787

required input signal level. The entire amplification chain was calibrated to an accuracy of ± 0.2 dB using precision attenuators over the frequency range 25-300 MHz. Accurate gain calibration is required because the hot cold loads cannot be used at this IF frequency. This is because the IF amplifier is not as quiet as before ($T_{IF} \simeq 125K$ vs. $T_{IF} = 14K$ for the cooled GaAs amplifier) and we do not have cooled isolators that will fit into our cryostat at these lower frequencies of 25-300 MHz. These considerations also preclude accurate noise measurements with the low IF amplifiers.

6.2 Niobium at 4.2K and 1.3K

These experiments present an illuminating situation where the same junction can be made to perform in the strong or weak quantum regime by simply changing the LHe bath temperature. The main advantage of using the same physical junction to show strong and weak quantum effects is that the rf embedding impedances, which depend on the electrode geometry and the junction capacitance, remain unchanged. Since mixer performance is strongly dependent on the embedding impedances, keeping these constant allows one to separate out the effects of changing I-V quality. At 4.2K, the Nb I-V is quite rounded on the voltage scale of $\hbar\omega/e$ and shows only weak quantum effects. When the temperature is lowered, the I-V becomes considerably sharper and shows strong quantum mixing effects.

After optimization of the mixer with a monochromatic signal at 33 GHz and an LO frequency of 34.5 GHz, the mixer gain and noise were measured with the hot/cold loads. The largest gain at both 1.3K and 4.2K was found on the fourth step below the gap and is listed in Table 6-1. The pumped I-V curves are shown in Figs. 6-4a and 6-5a along with a theoretical fit discussed in chapter VII. The variation of IF output power (coupled gain) with dc bias is shown in Figs. 6-4b and 6-5b for best

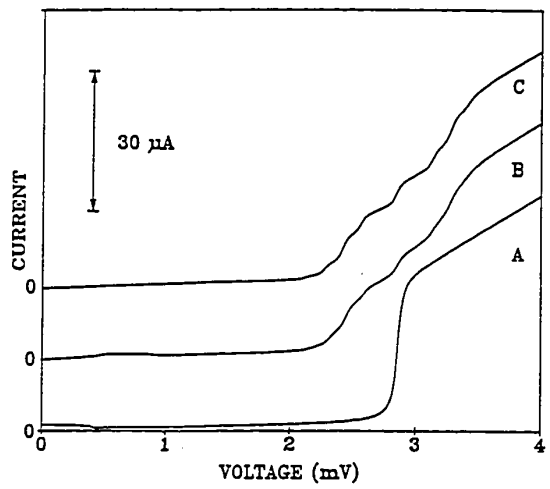

Fig. 6-4a (A) Experimental dc I-V for the Nb junction at 4.2K. (B) Experimental pumped I-V to produce the best gain on the fourth photon step. (C) Calculated voltage driven pumped I-V with V_{LO} adjusted to match the experimental pumped current on the fourth photon step (V_{LO} = 0.575 mV) as discussed in chapter VII. Zeros are offset for clarity.

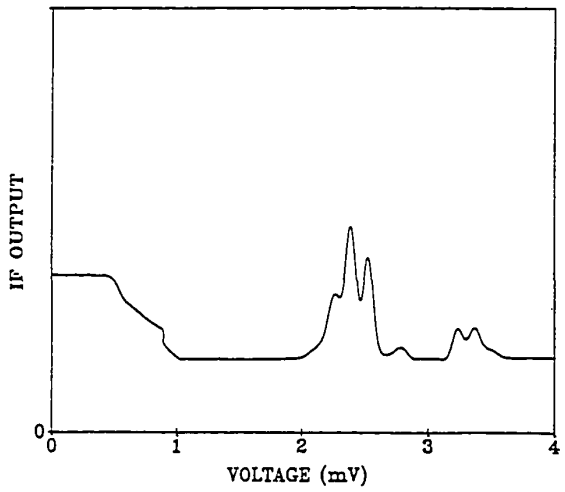

Fig. 6-4b Experimental plot of IF output vs. dc bias for Nb at 4.2K. The peak height on the fourth step (V = 2.37 mV) represents a coupled gain of 0.26 and an available gain of 0.27.

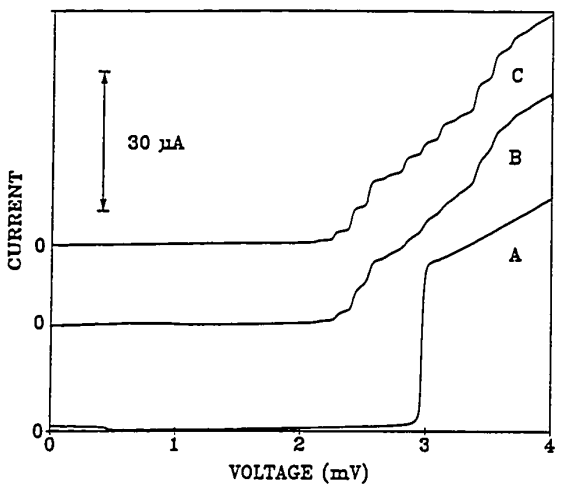

Fig. 6-5a (A) DC I-V at 1.3K for the Nb junction. (B) Experimental pumped I-V for best gain on the fourth step. (C) Calculated voltage driven pumped I-V with V_{LO} adjusted to match the experimental pumped current on the fourth step (V_{LO} = .675 mV). Zeros are offset for clarity.

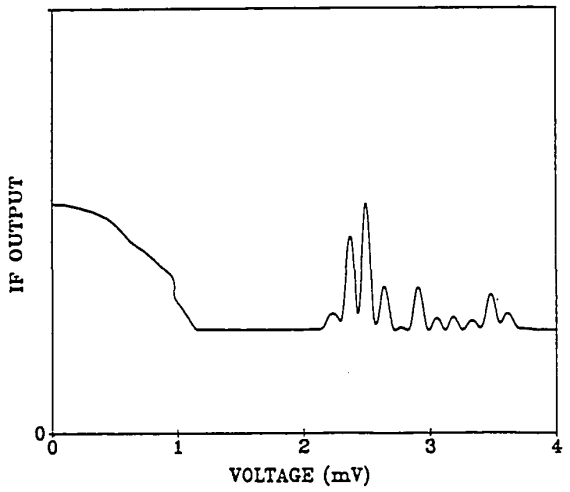

Fig. 6-5b Experimental plot of IF output vs. dc bias for Nb at 1.3K. The peak height on the fourth step (V = 2.49 mV) represents a coupled gain of 0.55 and an available gain of 0.56.

performance on the fourth photon step. By comparing these results at 4.2K with those at 1.3K, it is clear that the sharper I-V curve in Fig. 6-5a at 1.3K displays more well defined photon steps, a stronger modulation of the IF output, larger gain, and lower noise. All of these effects are expected when the I-V becomes sharp on the voltage scale $\hbar\omega/e$. Detailed modeling of these effects with the quantum mixer theory is discussed in chapter VII and shows that the reduced noise at 1.3K is consistent with the theory. The theory, however, also predicts very large or infinite available gain which was not observed in these experiments at 1.3K. The possible causes of this discrepancy are discussed in chapter VII.

As discussed in 6.1.5, we have also determined the receiver noise temperature for the niobium junction at 4.2K and 1.3K. The plot in Fig. 6-6 illustrates the procedure graphically with the actual RF and IF powers used to determine T_R. Clearly, the sharper and lower leakage I-V at 1.3K makes a significant improvement in the receiver noise temperature from 96K to 42K.

6.3 Tantalum at 1.3K - Gain and Noise vs. Photon Step

In order to investigate the variation of mixer performance with photon step, we have accurately measured the gain and noise of a 44 Ω Ta junction at a series of bias voltages. These results are also summarized in table 6-1. The pumped I-V curves for each of the bias voltages are shown in Fig. 6-7 and show well defined photon steps. The variation of IF output power (coupled gain) with dc bias is also shown in Fig. 6-8 and demonstrates the strong gain modulation on the voltage scale $\hbar\omega/e$. Both of these figures are compared with the predictions of the quantum mixer theory in chapter VII. The pumped I-V's are quantitatively well modeled by the theory while only the relative variation of coupled gain with dc bias can be accurately predicted. As with the Nb junctions, the best gain and lowest noise are

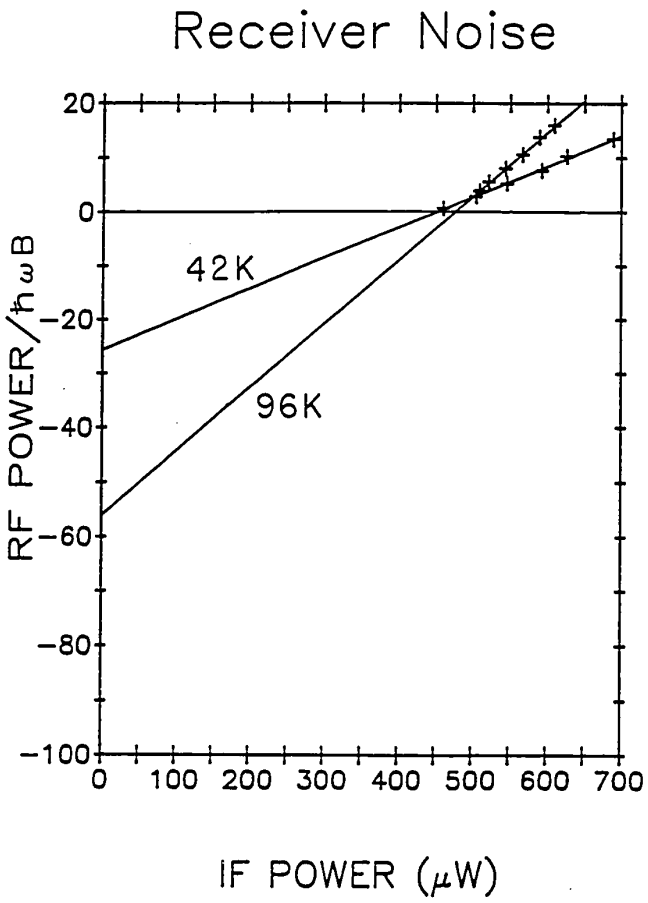

Fig. 6-6 Plot of IF output power vs. input power from the hot/cold load T_1 in units of photons per unit bandwidth for the Nb junction at 1.3K and 4.2K. The slope of the line is proportional to the overall receiver gain and the zero IF power intercept is the receiver noise power. Converting these powers to temperatures gives T_R = 96K and T_R = 42K for the Nb junction at 4.2K and 1.3K respectively.

found on the fourth photon step below the gap. The gain is also strongly modulated as a function of bias voltage whereas the noise is nearly constant. The values of receiver noise for each photon step are also listed in Table 6-1. The lowest receiver noise of 24 ± 1K is the lowest value reported to date for a heterodyne receiver in this frequency range. These values of receiver noise and mixer noise are competitive with the best results for masers in this frequency range [Moore and Neff, 1982; Moore and Clauss, 1979].

The experimental results discussed thus far, using a 1.5 GHz IF, do not show the large gain that can be achieved with such high quality tunnel junctions [McGrath et al., 1981]. By adjusting the backshort and screw tuner, values of the RF embedding impedance could be found that produced regions of negative resistance on as many as 5 photon steps as is shown in Fig. 6-9. The simple mixer model in chapter II and previous experiments [McGrath et al., 1981; Kerr et al., 1981] suggest that negative resistance implies infinite available mixer gain for a low enough IF that the embedding impedance is the same at the signal, LO, and image frequencies. Since the RF bandwidth of our mixer block is narrow compared with the 1.5 GHz IF, however, the signal frequency is badly mismatched when the coupling is adjusted for negative resistance steps. Low values of gain, $G_A << 0.1$, are observed under these conditions. These results suggest that large or infinite gain may be available for a low enough IF such that signal and image impedance are nearly equal. Experiments to show this effect have been performed and are described in section 6.6.

6.4 Tantalum at 1.3K and 2.08K - Noise vs. Subgap Current

In order to investigate the dependence of mixer gain and noise on subgap current, we have measured the Ta junction discussed above at two different bath temperatures (1.3K and 2.08K). As expected from theory (see

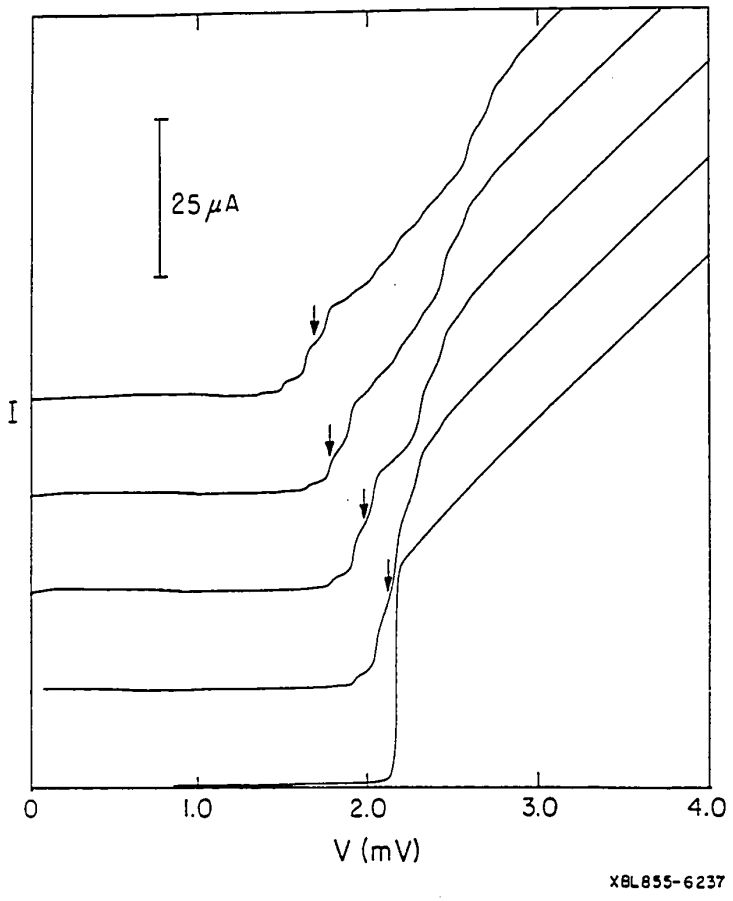

Fig. 6-7 Pumped and dc I-V curves for the 44 Ω tantalum junction with zeros offset for clarity. The bias voltages where the mixer data in Table 6-1 were taken are indicated. (Figure courtesy of W.R. McGrath.)

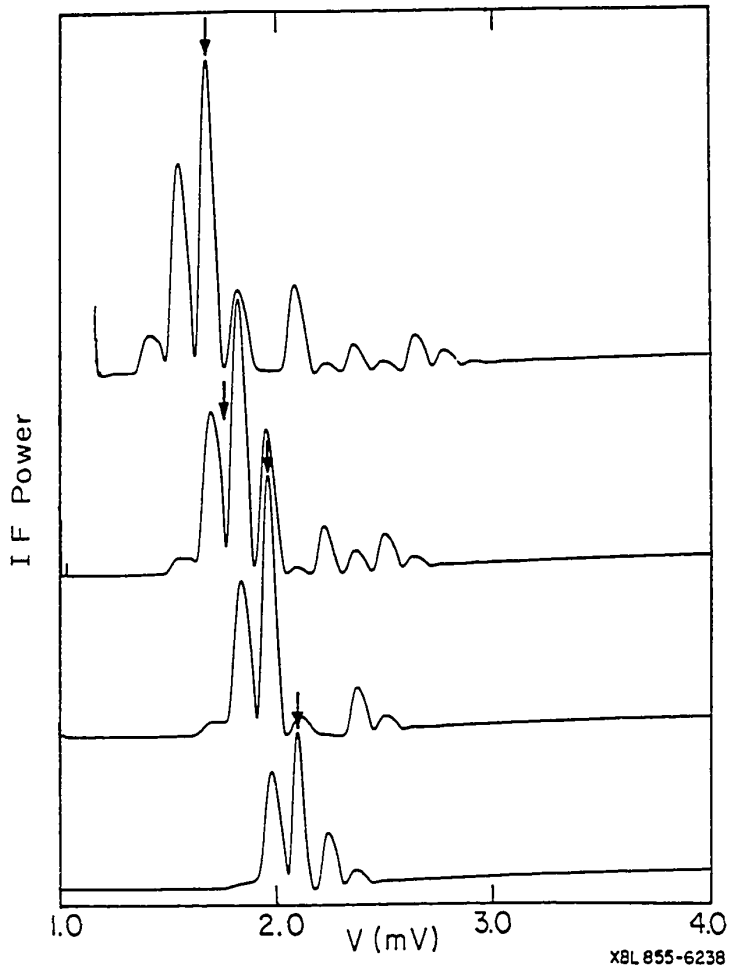

Fig. 6-8 IF output power vs. dc bias for the pumped I-V curves in Fig. 6-7 with the bias voltages for the data in Table 6-1 indicated. Zeros are offset for clarity. (Figure courtesy of W.R. McGrath.)

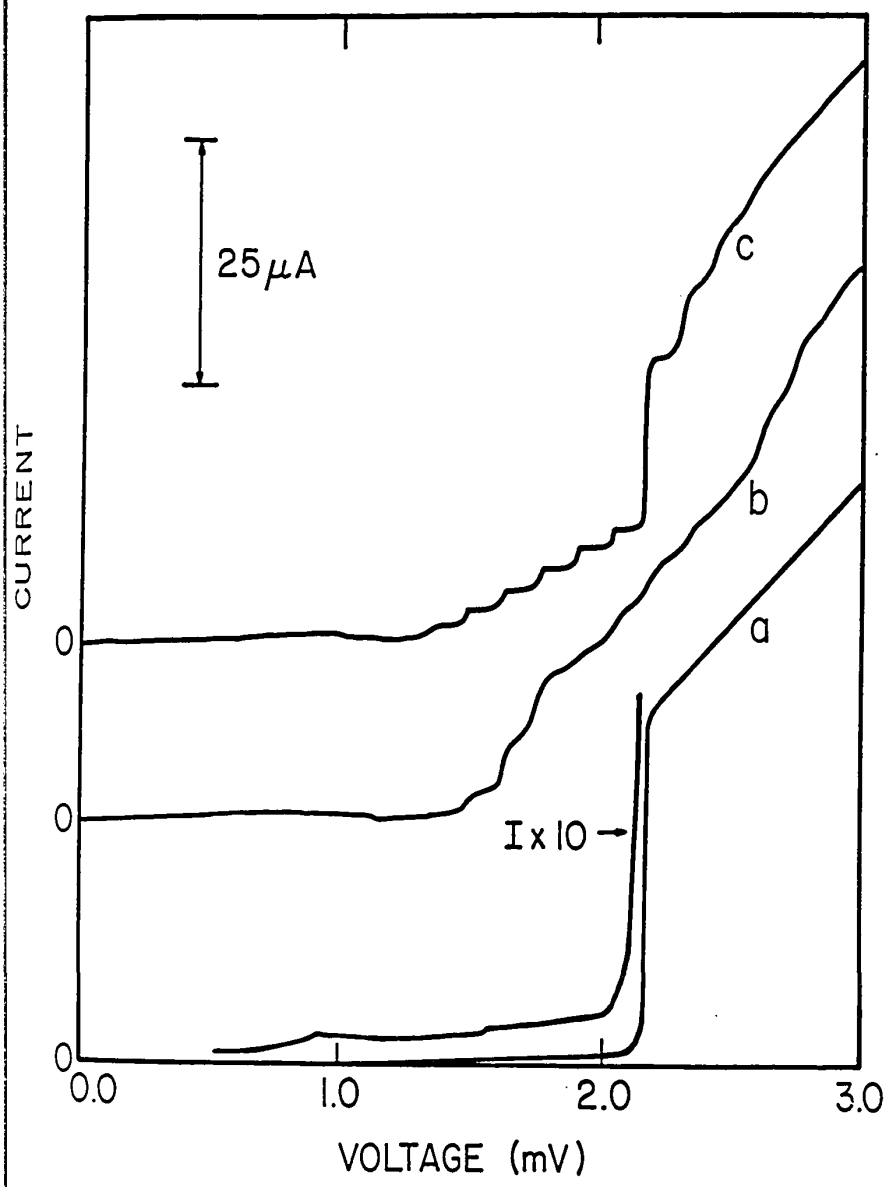

Fig. 6-9 (a) DC I-V curve for 44 Ω Ta junction at 1.3K. (b) Typical pumped I-V for mixer gain of ≈1 on the fourth photon step. (c) Same junction with rf tuning adjusted to produce negative quasiparticle resistance on five photon steps simultaneously. Zeros are offset for clarity.

chapter II) and shown in Fig. 6-10, the subgap current is strongly dependent on temperature while the width of the current rise at the sum gap is relatively insensitive to temperature in this range. This allows the effect of subgap current to be studied independently from the effect of I-V sharpness. As shown by the results in Table 6-1, the mixer noise in this junction increases by about 0.4 ± 0.4K from 5.2 ± 0.4K to 5.6 ± 0.4K, while the gain stays constant at 1.1 ± 0.1. These results for increased noise are consistent with the theoretical modeling discussed in chapter VII.

6.5 Lowest Leakage Tantalum - Quantum Noise Limit

An early experiment with a 101 Ω Ta junction with very low sub-gap leakage current (< 0.5%) but a slightly rounded I-V at the sum-gap produced the lowest value of T_M (= 3.8 ± 1K) that we have measured. The slightly rounded I-V is due to the use of a pure lead counter-electrode which shows some width to the current rise at the sum-gap due to energy gap anisotropy effects. Anisotropy effects are discussed in detail in chapters II and V. The use of a PbBi alloy counter-electrode in all of the other junctions eliminates this effect. The gain and noise were only measured on the first step for this junction. The lower value of gain for this junction (G = 0.38) is probably due to the width of the current rise at the sum-gap. Unfortunately, this junction was blown out by an electrical transient (opps!) before additional measurements on different photon steps could be performed.

6.6 Tantalum at 1.3K with Low IF - Effects of the rf Bandwidth

As mentioned in section 6.3, it is possible to find values of the rf embedding impedance that produce negative or very large dynamic resistance on up to five photon steps. As discussed in chapter two and by McGrath et al., (1981), this large dynamic resistance on the pumped I-V indicates that large gain is available for a low enough IF that the signal and image

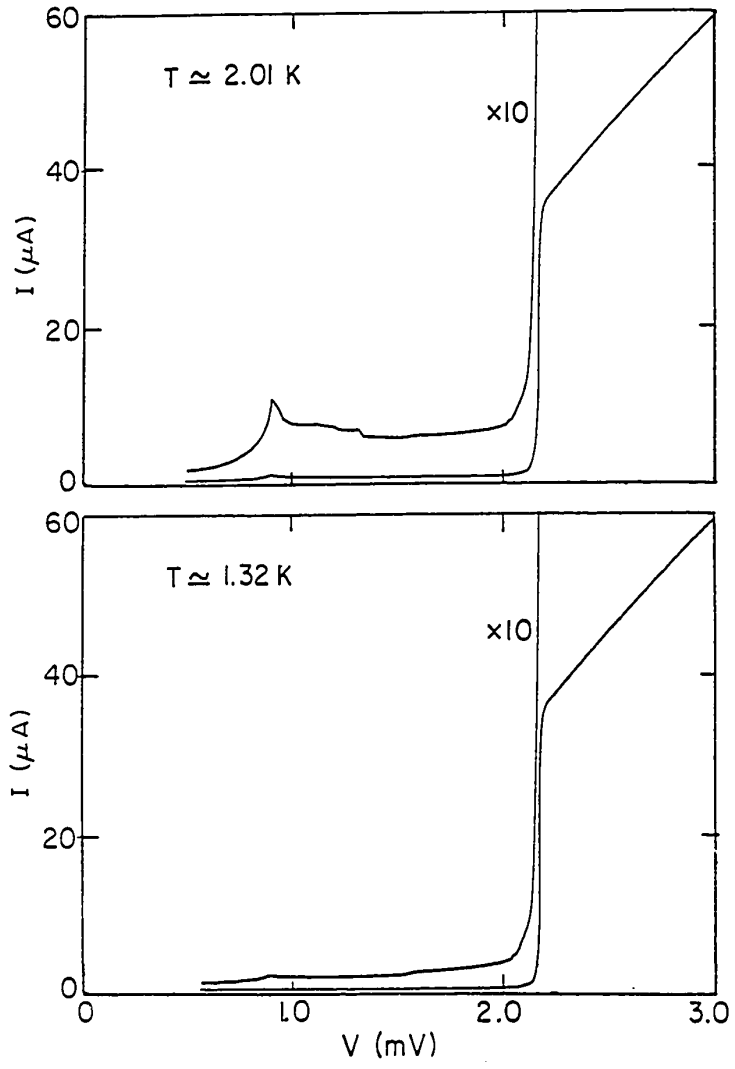

Fig. 6-10 DC I-V curves for 44 Ω Ta junction at two different bath temperatures 1.32K and 2.08K illustrating the increase in sub-gap current at higher temperature with relatively little change in the sharpness of the current rise at the sum-gap.

TABLE 6-1 Summary of mixer results with an IF of 1.5 GHz. G_A is the available gain and G_C is the coupled gain. θ is the mixer noise power in units of photons per unit bandwidth $\hbar\omega B$. Measured noise temperatures are accurate to ±0.6K or better unless otherwise noted and approach the quantum limit of 2.5K. The gain measurements are accurate to ±10%. Measurements with IF=1.5 GHz have sideband ratios >18 dB. The lowest noise junction had a broad current rise at the sum gap due to the use of a Pb (not PbBi) counter-electrode and therefore had a lower gain.

Junction R_n (Ω)	Photon Step	θ ($\hbar\omega B$)	T_M(SSB) (K)	G_A (SSB)	G_C (SSB)	Receiver Noise T(K)
72 (Nb)	4	2.8	5.5±0.8	0.56	0.55	42 ± 1
	4	4.9	9.0±1.6[a]	0.27	0.26	96 ± 2
101 (Ta)	1	1.8	3.8±1	0.34	0.33	...
44 (Ta)	4	2.7	5.2	1.1	0.79	29 ± 1
	4	2.9	5.6	1.1	0.79	30 ± 1
	4	2.4	4.7	0.83	0.74	24 ± 1
	3-4	4.1	7.6	0.064	...	...
	2	3.0	5.7	0.58	0.41	38 ± 1.5
	1	3.1	6.0	0.40	0.39	52 ± 2

a.) Measured at a bath temperature of 4.2K

frequency have nearly the same embedding impedance. With this in mind, we have performed a series of experiments with IF's of 25, 100, and 300 MHz to look for large available gain. The LO frequency has been held fixed at 36 GHz for all of these experiments. Two junctions have been used; one junction is the same one discussed in section 6.3, but with an increased resistance (73 Ω vs 44 Ω) due to exposure to air for ~ 6 hours while the other is a new junction with a resistance of ≈23 Ω. Large gain and negative resistance were easily observed with both of these junctions using a 25 MHz IF. The results for each junction will be discussed separately below.

In order to investigate the effect of different IF's, the 73 Ω junction was optimized for the largest coupled gain in the upper sideband with an IF of 25 MHz and then the IF was varied by changing the signal frequency without readjusting the tuning. The output power of the signal source was of course kept constant (±0.2 dB) as the frequency was varied. The largest coupled gain occurred when the dynamic resistance (R_D = dV/dI) on the first photon step approached ≈500 Ω. Larger and negative values of R_D produced smaller but finite coupled gains. The fact that the coupled gain remained finite as R_D and the impedance mismatch became infinite indicates that infinite gain was available for a matched IF load. This observation is consistent with previous experiments [McGrath et al., 1981; Kerr et al., 1981]. {Recent experiments [Raisanen et el., 1986] using an IF matching transformer demonstrate that large coupled gains can be achieved for a large R_D and a well matched IF output.} The variation of the coupled gain with IF is shown in Fig. 6-11 and illustrates the narrow-band coupling of our mixer block. The bandwidth (for 3 dB gain compression) under these tuning conditions is $\Delta f \approx 100$ MHz. It is interesting to note that the best gain is found on the first photon step with the low IF of 25 MHz, while the fourth step showed the largest gain with a 1.5 GHz IF. As discussed in

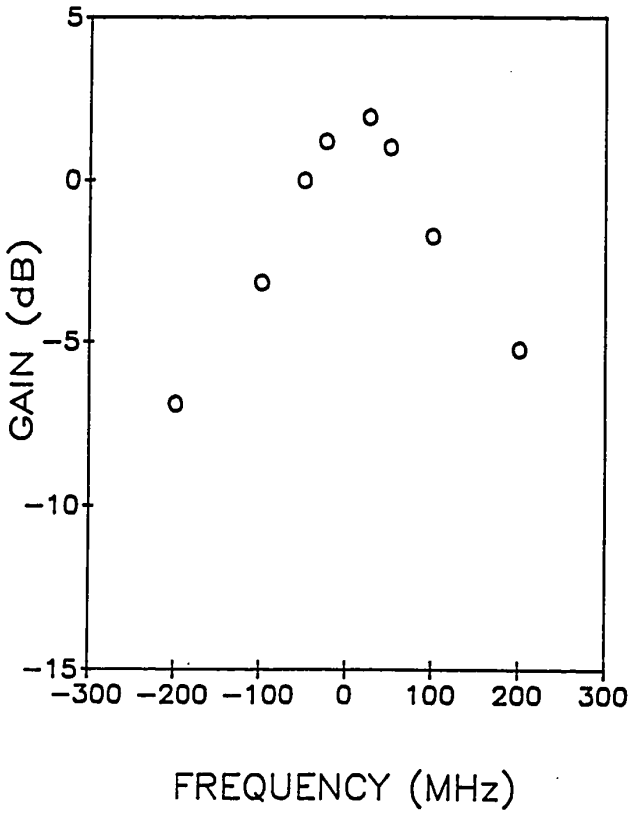

Fig. 6-11 Variation of the coupled gain with IF for the 66 Ω Ta junction in Table 6-2 optimized for best coupled gain in the upper sideband with an IF of 25 MHz on the first photon step. The best coupled gain of ≈2 dB corresponds to an available gain of 6.7 dB.

chapter VII, this observation can be explained by the different image impedances for the 25 MHz and 1.5 GHz experiments.

In order to further investigate the dependence of gain on IF, we have also studied a ≃ 23 Ω Ta junction with an even wider range of IF's and tuning conditions. The aim of this study is to find the maximum coupled gain for a series of IF's (25 MHz, 100 MHz, and 300 MHz). The previous experiment simply optimized the gain with a 25 MHz IF and then allowed the IF to vary without readjusting the tuning. This experiment optimizes the gain at a series of IF's for the signal in the upper or lower sideband. The results of this optimization and IF variation are listed in Table 6-2. Clearly, the best gain is found with a 25 MHz IF on the first photon step. The pumped I-V's and variation of the IF output with dc bias are illustrated for each of the optimized IF's in Figs. 6-12a-e. As the IF is increased, the maximum achievable gain is reduced and moves to photon steps further from the gap. The three dB bandwidth also increases from ≃100 MHz with a 25 MHz IF to ≃200 MHz with a 300 MHz IF.

These experiments illustrate the importance of a broad instantaneous rf bandwidth (i.e. double-sideband mixer operation) in obtaining large mixer gains. A broad instantaneous rf bandwidth is also technically useful for real receivers. We anticipate that broad-band rf matching with an IF of 1.5 GHz would have given large gain G>1 and low noise for the experiments discussed in sections 6.2-6.4. These ideas have recently been confirmed in experiments by Raisanen et al., (1986), [see also Richards, 1987] where large gain was observed with a 1.5 GHz IF and broad-band coupling at 90 GHz.

6.7 Conclusions

The experiments discussed in this chapter represent the most accurate and extensive series of measurements to date of noise and gain in SIS mixers showing strong quantum effects. These measurements show that

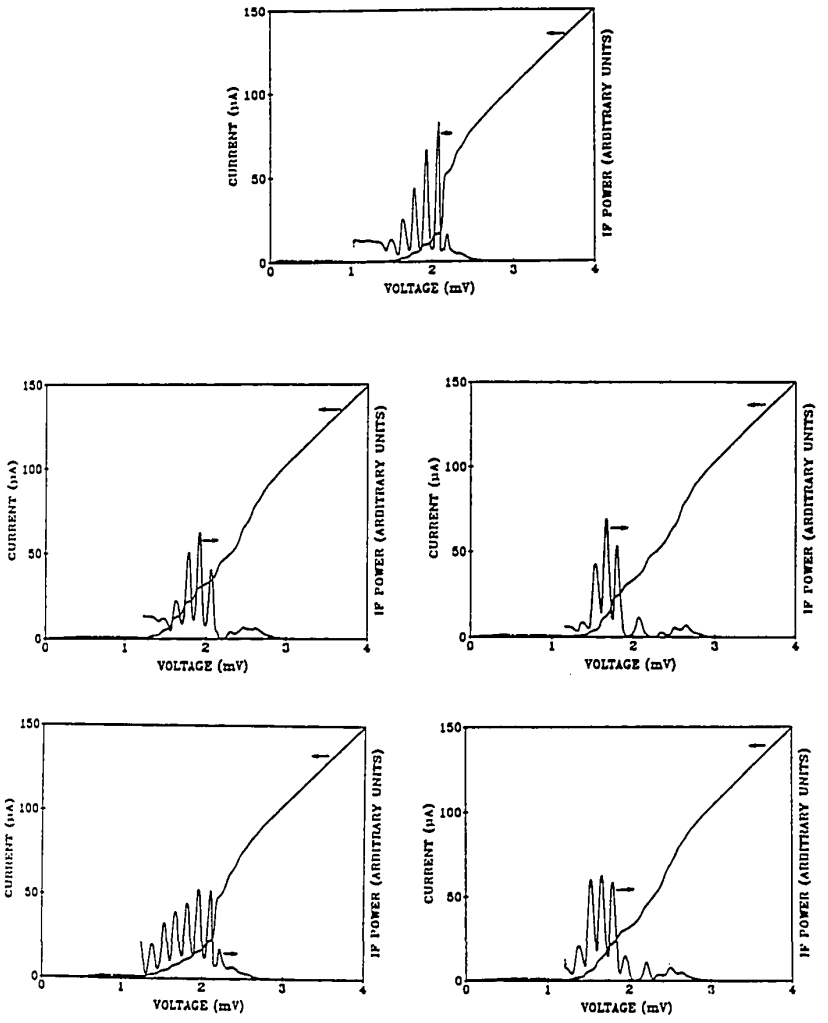

Fig. 6-12 Pumped I-V's and coupled gains for the 23 Ω Ta junction listed in Table 6-2. (a) Optimized for best coupled gain G_C on the first photon step (n=1) with a 25 MHz IF (USB). (b) Optimized for the best G_C on n=2 with 100 MHz IF (USB). (c) Optimized for the best G_C on n=2 with 100 MHz IF (LSB). (d) Optimized for the best G_C on n=4 with 300 MHz IF (USB). (e) Optimized for the best G_C on n=4 with 300 MHz IF (LSB).

TABLE 6-2 Summary of mixer results with a low IF of 25 to 300 MHz. The photon step (n) is the one where the best coupled gain was found for the particular IF and sideband being optimized. G_C is the coupled gain into our 50 Ω IF system and G_A is the available gain into a matched load assuming a mixer IF output resistance of R_D.

Junction R_n (Ω)	Photon Step	f_{IF} (MHz)	Dynamic R_D(Ω)	G_A (SSB)	G_C (SSB)	Sideband Ratio (dB)	Sideband
66	1	25	500	4.7	1.6	0.8	USB
23	1	25	107	1.3	1.2	0.1	USB
	2	100	37	0.5	0.49	3.0	LSB
	3	100	50	0.64	0.64	6.6	USB
	4	300	20	0.63	0.51	11.2	LSB
	4	300	24	0.60	0.52	11.6	USB

noise powers approaching the quantum limit and large gain can be obtained for tunnel junctions with sharp low leakage I-V characteristics. The receiver noise temperature of 24 ± 1K is the lowest reported to date for a heterodyne receiver. The lowest mixer noise temperature of 3.8 ± 1K is within a factor of two of the quantum limit of 2.5K at 36 GHz. These results are already competitive with low noise masers and unlike masers should be easily extendable to higher frequency. The variation of mixer gain and noise with I-V sharpness and subgap leakage has also been accurately quantified. The modeling of mixer noise and gain in the next chapter would not have been possible without these kinds of accurate measurements with low leakage junctions. The observation of larger gain for low IF frequencies in our narrow band mixer block illustrates the need for broad-band rf coupling in future experiments with a 1.5 GHz IF.

VII. Theoretical Modeling

This chapter discusses several studies to compare our experimental results in chapter VI with the predictions of the three port quantum mixer theory described in chapter II. The model calculations are divided into five major sections;

1) Modeling of the pumped dc I-V curves - photon assisted tunneling
2) Niobium junction at 4.2K - weak quantum mixing effects
3) Niobium junction at 1.3K - strong quantum mixing effects
4) Ta at 1.3K - gain and noise vs. photon step (n)
5) Ta at 2.08K - gain and noise vs. subgap current.

All of the noise calculations include the zero point fluctuation noise (P_N = 1/2 $\hbar\omega$B) of the image and signal impedances as discussed in section 2.3.7. Since all of the model calculations are performed for single sideband mixers (with poor image frequency coupling), the image termination noise is insignificant. For our low noise mixers, this means that the input noise power of the mixer contains two contributions; 1/2 $\hbar\omega$B from the signal impedance and a minimum of 1/2 $\hbar\omega$B from the mixer shot noise. The sum of these two contributions corresponds to a minimum input noise temperature of T_Q = $\hbar\omega$/kln2 = 2.5K.

It is found that the theory overestimates the experimentally measured gain by ~ 2 dB and underestimates the noise power by factor of ~ 2 for junctions displaying weak quantum mixing effects such as the niobium junction at 4.2K. Importantly, it is also demonstrated that a shorted image port leads to larger mixer gain on the fourth photon step than on the first step. This result agrees with the experimental data and is in contrast with the usual case (DSB mixers) where the largest gain occurs on the first step.

Junctions which are strongly in the quantum limit, such as the sharp Ta and Nb junctions at 1.3 K, however, have gains that are considerably less than the theoretical predictions. The failure of the three port theory is especially severe on the first photon step below the energy gap where large regions of infinite available gain are predicted to occur. A detailed discussion of the gain predictions on different photon steps is presented and compared with experimental results of chapter VI for Ta. The theory underestimates the measured noise power by a factor of 1.5 to 2 for high gain and low gain mixers. The theory, however, correctly predicts the increased noise due to increased ("leakage") current flowing below the sum gap. The consistent presence of an extra 1-3 K of noise in the experimental data, however, indicates the possibility of additional noise sources which have not been included in the present analysis. Table 7-1 at the end of the chapter provides a summary comparison of the experimental and theoretical results. The large disagreement in gain and the excess noise may indicate the need to include higher harmonics in our model (i.e., a five port calculation), but this has not been confirmed.

Before discussing the modeling results, it is useful to have an overview of the entire modeling procedure with the various inputs and outputs. This overview is provided by a flow diagram in Fig. 7-1. These calculations do not make the low IF approximation as is done in most other work, but include the IF on an equal footing with signal, image and LO frequency. The theory for these calculations is presented in chapter II. The accuracy of the computer calculations is discussed in Appendix C.

7.1 Modeling the Pumped DC I-V

As pointed out in chapter II, the general solution for currents flowing in the tunnel junction at the LO frequency and all of its harmonics is an extremely complex non-linear problem requiring knowledge of the embedding

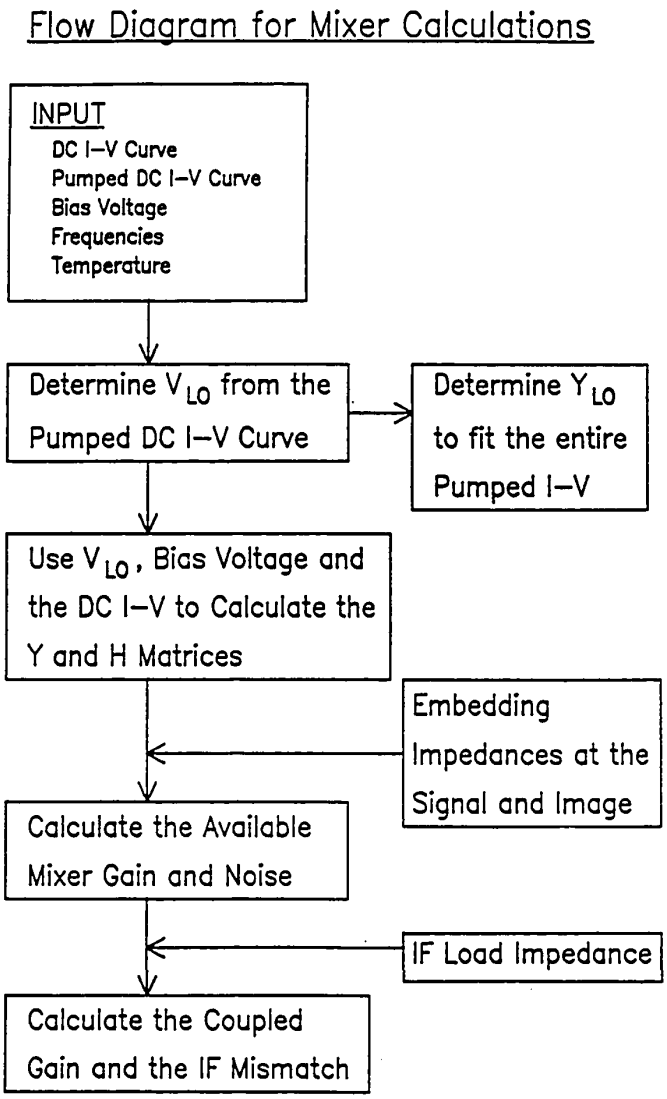

Fig. 7-1 Flow diagram for mixer calculations showing the various input and output information.

impedances at all of the harmonic frequencies. For the purpose of this analysis, we assume that all of the LO harmonics are shorted (by the junction capacitance) and solve for the DC and LO frequency currents. It will be shown by the end of this section that a reasonable fit to the experimental pumped I-V is obtained under these conditions.

The problem of modeling the pumped DC I-V curve is now reduced to finding the magnitude of the LO current source, I_{LO}, and the complex embedding admittance, Y_{LO}, which are shown in the equivalent circuit of Fig. 7-2. Once I_{LO} and Y_{LO} are determined, as discussed below in sections 7.1.1-3, V_ω is determined by the solution to Eq. 7-1

$$I_{LO}(V_\omega) = I_\omega(V_o,V_\omega) + Y_{LO}V_\omega \qquad 7\text{-}1$$

which expresses current conservation in the circuit of Fig. 7-2. The voltage across the junction is given by,

$$V(t) = V_o + V_\omega \cos\omega t \qquad 7\text{-}2$$

The current flowing in the junction at the LO frequency is given by,

$$I_\omega(V_o,V_\omega) = A \cos \omega t + B \sin \omega t \qquad 7\text{-}3$$

with the coefficients A and B given by,

$$A = \sum_{n=-\infty}^{\infty} J_n(\alpha)[J_{n+1}(\alpha) + J_{n-1}(\alpha)]I_{dc}(V_o + n\hbar\omega/e) \qquad 7\text{-}4$$

$$B = \sum_{n=-\infty}^{\infty} J_n(\alpha)[J_{n+1}(\alpha) + J_{n-1}(\alpha)]I_{KK}(V_o + n\hbar\omega/e) \qquad 7\text{-}5$$

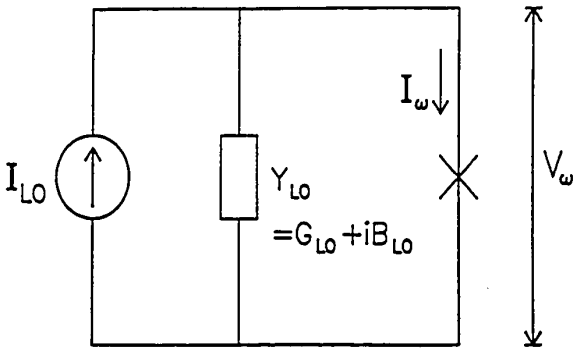

Fig. 7-2 Equivalent circuit for the SIS junction at the LO frequency.

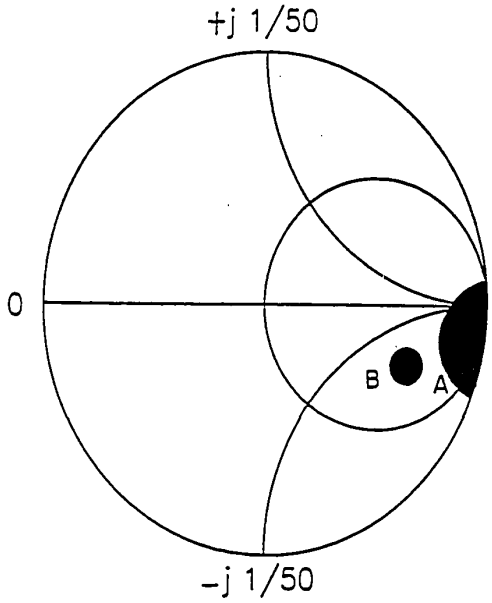

Fig. 7-3 Range of admittances Y_{LO} that reproduce the experimental pumped I-V curves. Region "A" reproduces the pumped I-V for the 1.5 GHz experiments while region "B" reproduces the pumped I-V for the low IF 25 MHz experiment.

where $\alpha = eV_\omega/\hbar\omega$, J_n is the nth order Bessel function of the first kind, and I_{KK} is the Kramers Kronig transform of the unpumped DC I-V discussed in chapter II. After solving Eq. 7-1 for V_ω, the pumped DC current at V_0 is given by,

$$I_o(V_o,V_\omega) = \sum_{n=-\infty}^{\infty} J_n^2(eV_\omega/\hbar\omega)\ I_{dc}(V_o + n\hbar\omega/e) \qquad 7\text{-}6$$

By solving Eq. 7-1 for V_ω at a series of bias voltages, V_0, and using V_ω in Eq. 7-6 the pumped DC I-V curve can be plotted. From the experiment, we know the available LO power (which is proportional to I_{LO}^2), the physical position of the screw tuner and the backshort (which determine Y_{LO}), and the pumped and unpumped DC I-V curve. Three different techniques have been used to determine Y_{LO} and I_{LO} for the actual experimental conditions and are discussed below.

7.1.1 The "Eyeball" Technique

As the name implies, this technique uses a simple "eyeball" comparison of the experimental pumped I-V to a series of theoretical pumped I-V's in order to determine the best values for Y_{LO} and I_{LO}. The "eyeball" technique is the most successful of the three techniques discussed in this section and was originally developed by Phillips and Dolan, (1982). In this technique, Y_{LO} is treated as a free parameter and I_{LO} is set by the computer program in order to force the pumped dc current to match the experimental value at one dc bias voltage (usually the center of the first

photon step below the current rise). By searching the Smith[1] chart for admittances that give the best fit to the pumped I-V, Y_{LO} can be determined. Fortunately, it is possible to find an acceptable range of admittances fairly quickly since a large portion of the Smith chart gives obviously poor fits. Fig. 7-3 shows the range of admittances that gives a "good" fit to the experimental pumped I-V for the Ta junction that gave the best gain in chapter VI. These admittances are normalized to a conductance of 1/50 mho and are plotted on a simplified Smith chart that contains only the constant conductance circles for 0 and 1/50 mho and the constant reactance contours for 0 and ± j1/50 mho (the center of the chart represents a real conductance of 1/50 mho). Two calculated pumped I-V's and the original experimental pumped I-V are shown in Fig. 7-4 to demonstrate the quality of the fit. The original experimental data is also shown in Fig. 6-7 in the upper curve. All of the other pumped I-Vs for experiments with a 1.5 GHz IF are well fit by admittances in this range as will be shown in the following sections. The pumped I-Vs for the low IF experiments with flat steps and negative resistance have also been modeled. A search for admittances to fit the pumped I-V for our best coupled gain with a 25 MHz IF gave admittances in the range labeled "B" in Fig. 7-3.

7.1.2 Low Frequency Scale Model

Because it is virtually impossible to make direct impedance measurements in our mixer block at 36 GHz, an 8.2 times enlarged scale model was constructed by Antti Raisanen and Rob McGrath to allow direct measurements at ~ 4 GHz with a standard network analyzer (HP Model 8746B S

---

[1]Smith charts commonly used for representing complex impedances (or admittances) and are well discussed in many standard texts on microwave engineering.

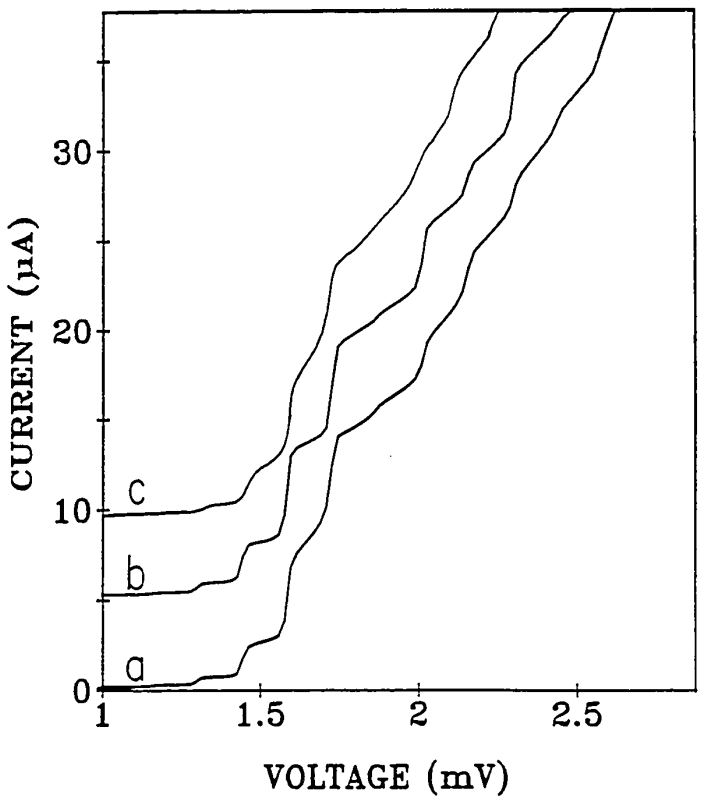

Fig. 7-4 a.) Experimental pumped I-V for the best gain at 1.5 GHz IF on the fourth photon step with the Ta junction from chapter VI (see the upper curve in Fig. 6-7). b.) Voltage driven pumped I-V (Z_{LO} = 0) c.) Z_{LO} = 0.01 + j10 Ω.

parameter test set) with a frequency range of 0.5 to 12.4 GHz. The details of the model and the measurement technique have been described by Raisanen et al., (1985). Basically, everything in the actual mixer block shown in Fig. 7-5b was scaled up by a factor of 8.2. The silicon substrate (dielectric constant ϵ_r = 11.7) with superconducting electrodes was modeled by an Epsilam-10[2] (ϵ_r = 10.2) substrate with copper electrodes defined by etching. A rigid copper coaxial cable of 0.86 mm diameter was soldered flat onto one copper electrode and extended into the center of the waveguide where the center conductor could make contact to the other copper electrode as shown in Fig. 7-5a. The impedance seen by the end of the coaxial cable looking out into the scaled mixer block should be the same as the experimental SIS junction sees when the screw tuner and backshort are properly adjusted to match their measured positions in the actual mixer block. This impedance, of course, will not include the junction capacitance which must always be added in parallel with the scale model impedance. The circuit diagram for this situation is shown in Fig. 7-6 where Y_S is the admittance determined from the scale model and C_J is the junction capacitance to be added in parallel.

The results of these measurements for several of the experiments described in chapter VI are shown in Fig. 7-7a. The results are measured using a 50 Ω reference impedance and are plotted on simplified Smith charts which contain only the constant resistance circles for 0 and 50 Ω and the constant reactance contours for 0 and ± j50 Ω (the center of the chart represents a real impedance of 50 Ω). The regions labeled "B" in this figure corresponds to the range of impedances that the junction could have seen at the LO frequency. The size of the region represents the sum of our

---

2 Epsilam-10, Electronic Products Division/3M, 225-4S-02 3M Center, St. Paul, MN 55144, U.S.A.

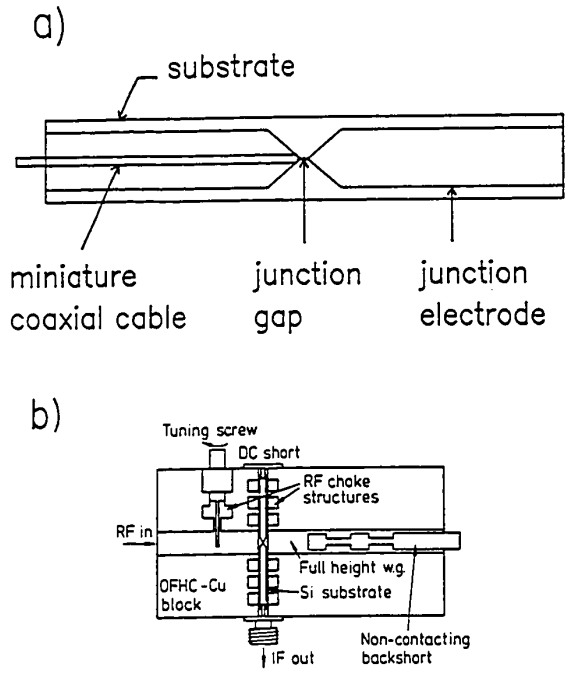

Fig. 7-5 a.) Scale model substrate with copper electrodes and miniature coaxial cable (not drawn to scale). b) The actual mixer block with screw-tuner, backshort and junction in place (from Raisanen et. al. (1985)).

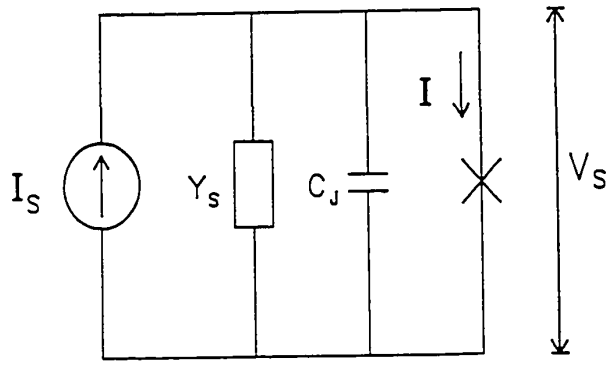

Fig. 7-6 Equivalent circuit for the scale model admittances with the junction capacitance added in parallel.

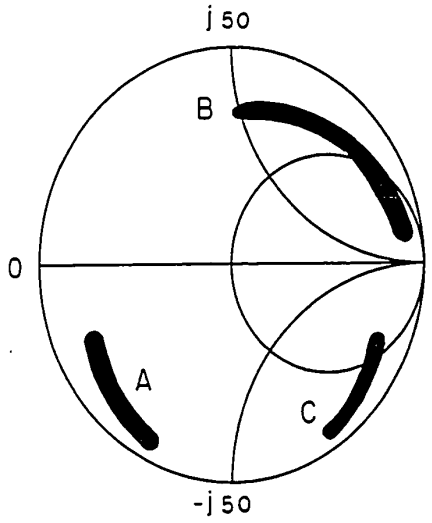

Fig. 7-7a Scale model impedances seen by the Ta and Nb junctions at the (A) signal (B) LO (C) and image frequencies.

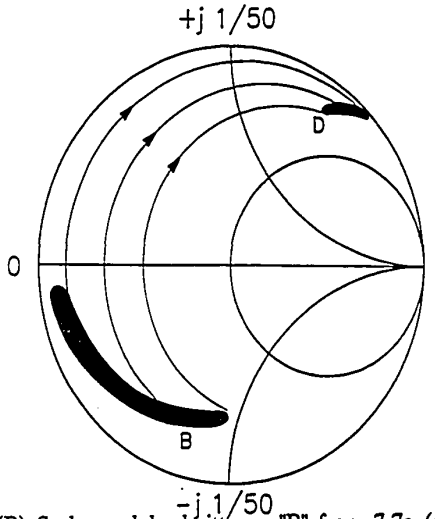

Fig. 7-7b (B) Scale model admittance "B" from 7-7a (note the simple 180 degree rotation). (D) Scale model admittance "B" with the the junction capacitance of 300 fF added in parallel (See equivalent circuit in Fig. 7-6).

uncertainties in the actual screwtuner and backshort positions and the junction position in the block which we could measure with an accuracy of ± 0.2 mm. In order to compare these impedance measurements with the admittances calculated in section 7.1.1, the impedances must be converted to admittances and the junction capacitance must be added in parallel. Fig. 7-7b shows an admittance plot of the data in Fig. 7-7a normalized to 1/50 mho (notice that this is just a 180 degree rotation of Fig. 7-7a). Region "D" shows the admittance obtained by adding the junction capacitance (~ 300 fF) in parallel with the scale model admittance. This is the admittance (Y_{LO}) seen by the junction in Fig 7-2.

Using the scale model admittances at the LO, an assumed range of junction capacitance from 300 to 600 fF in parallel with the junction, and the measured LO power, a number of pumped I-V curves were calculated. Unfortunately, none of these admittances in parallel with the assumed range of junction capacitance gave a pumped I-V that was even close to the measured pumped I-V curve. The range of admittances that does reproduce the pumped I-V (see section 7.1.1 and Fig. 7-3) is far removed from the "D" region of Fig. 7-7b. An excess capacitance of at least 2pF would be required to bring the region "D" close to the values calculated in section 7.1.1. At the present time, no source of error in our measurement technique appears to be large enough to account for the discrepancy and we must conclude that the scale model is not giving reliable values for Z_{LO}. This unfortunate situation means that the scale model impedances from the regions "A" and "C" (for the signal and image impedances) can not trusted to accurately model the mixer performance. As will be shown in section 7.2, the regions "A" and "C" do, in fact, predict mixer performance that is not observed in our experiments.

7.1.3 The Intersecting Circle Method

As originally discussed by Shen (1981), this technique uses the measured value of P_{LO} and the pumped current at a bias voltage V_0 to determine a circle of allowed values for Y_{LO}. The calculation of the circle coordinates begins with the relationship of P_{LO} to I_{LO} and Y_{LO}

$$P_{LO} = |I_{LO}|^2/8G_{LO} \qquad 7\text{-}7$$

$$= \{(V_{LO}G_{LO} + A)^2 + (V_{LO}B_{LO} + B)^2\}/8G_{LO}$$

where G_{LO} and B_{LO} are the real and imaginary parts of Y_{LO} and A and B are given in Eqs. 7-4 and 7-5. Equation 7-7 can be rearranged to give the equation of a circle:

$$(G_{LO} - x_o)^2 + (B_{LO} - y_o)^2 = r^2 \qquad 7\text{-}8$$

with radius

$$r = \left[\left[\frac{4P_{LO}}{V_{LO}^2} - \frac{A}{V_{LO}}\right]^2 + \left[\frac{A}{V_{LO}}\right]^2\right]^{1/2} \qquad 7\text{-}9$$

and centered at

$$x_o = 4P_{LO}/V_{LO}^2 - A/V_{LO} \qquad 7\text{-}10$$

$$y_o = -B/V_{LO} \qquad 7\text{-}11$$

where A and B are defined in Eqs. 7-4 and 7-5. Each different bias point generates a different required V_{LO} and therefore a different admittance circle. If harmonics are not important, then all of the circles should

intersect at a single point. It turns out, however, that the circles are very sensitive to small errors in the measurement of the pumped DC current and P_{LO} especially when large values of P_{LO} are used (i.e. when there is a large mismatch at the LO frequency). This means that when the junction is driven by a source that approximates an ideal current or voltage source it will be very difficult to use this technique to obtain Y_{LO}. This sensitivity makes it difficult to uniquely determine Y_{LO} for our experimental conditions with a 1.5 GHz IF. One possible solution to this problem is to require that the pumped I-V also have the correct slope at each bias point where the pumped DC current is being matched. Based on the fact that a large number of the circle defined admittances produce pumped I-Vs with the wrong slope at the chosen bias voltage, it seems likely that requiring the slopes to match would narrow the choice of allowed admittances to fit the pumped I-Vs. This improvement has not been pursued since the "eyeball" technique in section 7.1.1 already gave a good estimate of Y_{LO}.

7.2 Modeling of Niobium Results at 1.3K and 4.2K

These experiments present an illuminating situation where the same junction performs in either the strong or weak quantum regime by simply changing the LHe bath temperature. The main advantage of using the same physical junction to show strong and weak quantum effects is that the RF embedding impedances, which depend on the junction geometry and capacitance, remain unchanged. Since mixer performance is strongly dependent on the embedding impedances, keeping these constant allows one to separate out the effects of changing I-V quality. At 4.2K, the Nb I-V is quite rounded on the voltage scale of $\hbar\omega/e$ and shows only weak quantum effects. When the temperature is lowered, the I-V becomes considerably sharper and shows strong quantum mixing effects as discussed in chapter VI. The broadened I-V at 4.2K (compared to 1.3K) is due to the short

quasiparticle lifetime in the PbBi counter-electrode at this temperature (see chapters II and V).

7.2.1 Modeling of Niobium Results at 4.2K

Fig. 6-4a shows the pumped and unpumped I-V for the Nb/PbBi junction at 4.2K discussed in chapter VI . The theoretical pumped I-V in Fig. 6-4a was obtained by assuming an ideal voltage source at the LO frequency and adjusting its amplitude, V_{LO}, until the pumped current calculated with Eq. 7-6 on the fourth step matched the experimental value. This technique gave a reasonable fit to the pumped I-V. Once V_{LO} is determined by this technique, the Y and H matrices can be calculated with the quantum mixer theory and the mixer performance predicted for any combination of impedances at the IF, signal, and image frequencies. The range of signal and image impedances obtained from the scale model for this experiment is shown in Fig. 7-7. When these impedances are used with the calculated Y and H matrices, low gain (< -10 dB) and large noise (T_M > 10K) are predicted. If contours of constant gain are plotted versus the real and imaginary part of the signal impedance, it is very obvious that the scale model impedances are a long way from any local optimum for mixer performance. The theory predicts that the best performance will occur for signal impedances in the upper half plane where the junction capacitance is almost completely tuned out. This is clearly not where the scale model impedances are found (see region "A" in Fig. 7-7a). Even after accounting for our worst possible measurement errors of junction, backshort and screwtuner position, the scale model always predicts impedances in the lower half plane. Unfortunately, this evidence along with that discussed in section 7.1.2 forces us again to seriously doubt the accuracy of the scale model measurements at this time.

To make progress we must assume a reasonable range of impedances

for the signal and image frequencies. If one allows complete freedom for all of these variables (4 in all) the problem becomes hopelessly complex. Fortunately, the only range of signal impedances that gives reasonable agreement with the experiment is in the region that resonates out the junction capacitance. We have assumed that the capacitance of the Nb and Ta junctions is given by the literature value [Broom et al., 1980] for Nb junctions of 140 fF/μm^2, which gives ~ 300 fF for our 2 μm^2 junctions ($1/j\omega C_J \simeq$ -j15 Ω for 300 fF at 36 GHz). Different values for C_J merely shift the best performance to a slightly different Z_S. Fig. 7-8a shows a plot of constant available gain contours on the fourth photon step for a range of signal impedances Z_S with a shorted image frequency. Fig. 7-8b shows a plot of constant noise temperature for the same conditions as in Fig. 7-8b. Different image impedances (other than a short circuit) have also been studied and found to produce similar gain and noise contours. For all image impedances, the best gain and lowest noise occur for approximately the same values of Z_S. This $Z_S \simeq 3 + j15$ Ω, in parallel with the assumed C_J produces a nearly real impedance of approximately 75 Ω across the junction. The mixer non-linearity parameter η (see Eq. 2-66) was also evaluated for this junction and found to be less than one on the fourth step. This implies that mixer gain will always be less than 0 dB on the fourth step. This is also the case for classical mixers (see chapter II). The maximum gain from the contour plot (~ -3.8 dB) is clearly larger than the experimental value of $G_A = 0.27 \pm 0.03$ (= -5.7 ± 0.4 dB). The predicted minimum noise temperature of 5.3 K is also clearly less than the measured value of $T_M = 9.0 \pm 1.6$K.

For these results with a rounded Nb I-V curve, the difference between coupled and available gain turns out to be relatively small for typical IF impedances of 50 to 100 Ω (i.e. the impedance mismatch at the IF port is small). To illustrate this fact, the coupled gain is plotted in Fig. 7-9 for a

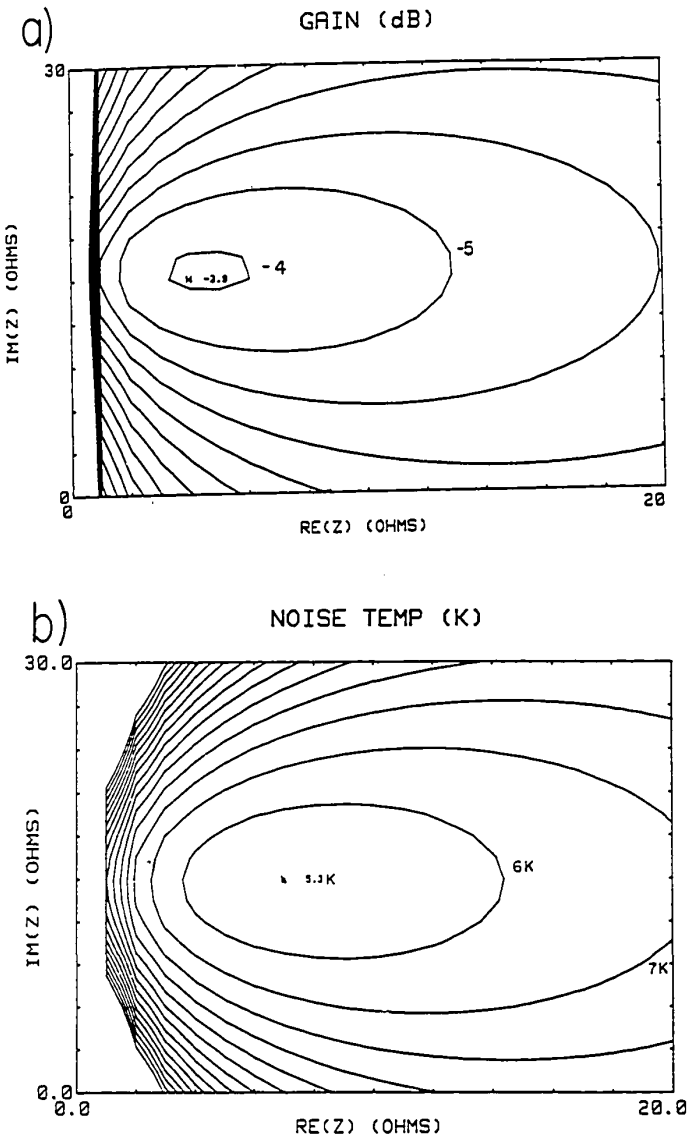

Fig. 7-8 a) Contour plot of available gain vs. Z_S for Nb at 4.2K on the fourth step using V_{LO} = .575 mV with a shorted image impedance (Z_i = 0.01 + j0.01 Ω) b) Noise contour plot for the same parameters. The experimental gain was -5.7 dB and the experimental noise temperature was 9.0 ± 1.6K.

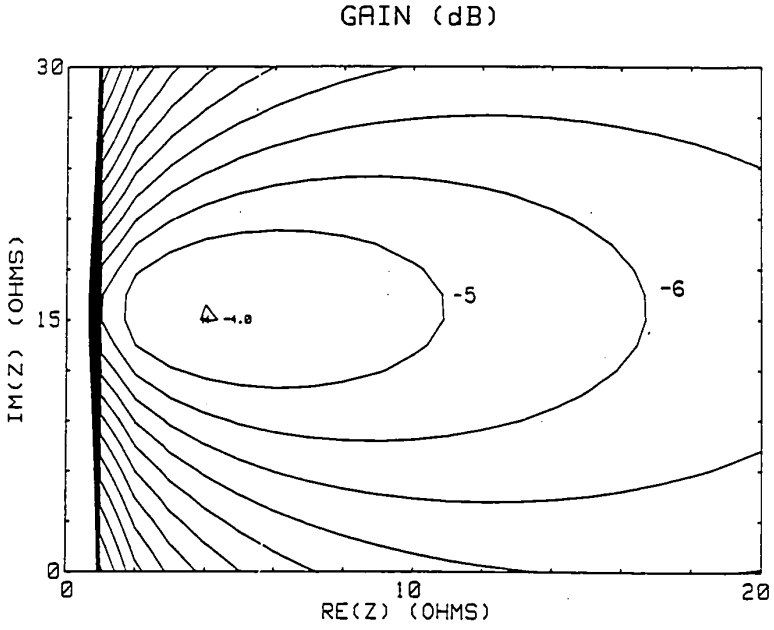

Fig. 7-9 Contour plot of coupled gain vs. Z_S for Nb at 4.2K on the fourth photon step with a 100 Ω IF and a shorted image port. Comparing this plot with Fig. 7-8a reveals a very small IF mismatch which is consistent with the experimental observation.

100 Ω IF load impedance and a shorted image. This plot is nearly equivalent to the available gain plot in Fig. 7-8a for the same conditions. IF impedances of 50 Ω and 100 + j100 Ω produce very similar contours. Clearly, the coupled and available gain are both maximized for the same impedances with a relatively small IF mismatch. This result means that if we optimize the mixer based on the coupled gain, as we do in the real experiment, we will also be near a maximum in available gain. This important conclusion is not generally true for mixers that show strong quantum effects as shown in sections 7.2.2 and 7.3.

The dependence of the coupled gain and mixer noise temperature on DC bias voltage V_0 and LO drive voltage V_{LO} has also been examined. These calculations, with a fixed value of Z_S, Z_L, and Z_i, are shown in Fig. 7-10. These calculations closely match the experimental situation when trying to optimize the mixer by adjusting V_0 and V_{LO} for best coupled gain. In the experiment, the best Z_S and Z_i are found first and then V_0 and V_{LO} are adjusted for best coupled gain. This process is repeated several times in order to obtain the best coupled gain. This iterative process is necessary because the parameters Z_S, Z_i, and V_{LO} are very strongly coupled functions of the screw tuner and backshort position in our mixer block. The fixed value of Z_S used in Fig. 7-10 was chosen to produce the best coupled and available gain on the fourth photon step as shown in Figs. 7-8 and 7-9. These calculations demonstrate that the gain does indeed maximize near the center of each photon step as one moves away from the gap. The calculations also show that the maximum gain for each photon step requires a particular range of values in V_{LO}. This V_{LO} increases as one moves away from the sum gap voltage. These trends are all quantitatively consistent with our experimental observations. For example, the Nb experiment at 4.2K requires a V_{LO} of 0.58 mV to match the pumped I-V curve as shown in Fig. 6-4a. This same V_{LO} also predicts the center of a large gain

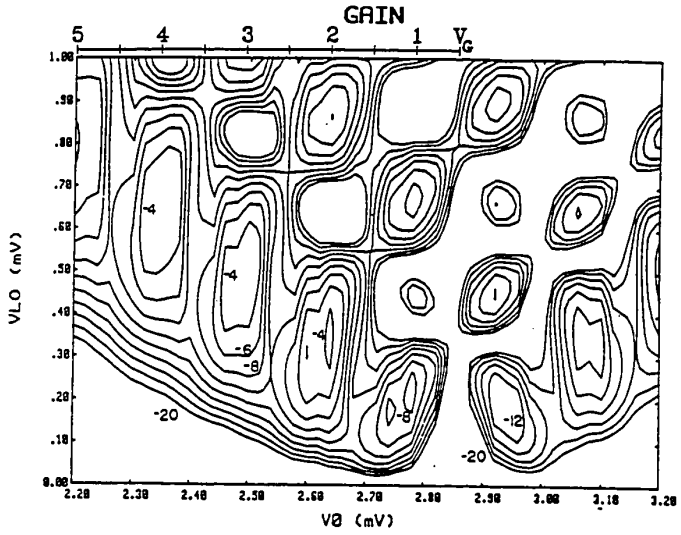

Fig. 7-10a Contour plot (2 dB contour interval) of coupled gain vs. DC bias and V_{LO} for Nb junction at 4.2K with a shorted image, a signal impedance of Z_S = 3 + j 15 Ω (for best gain on the fourth step), and an IF impedance of 100 Ω.

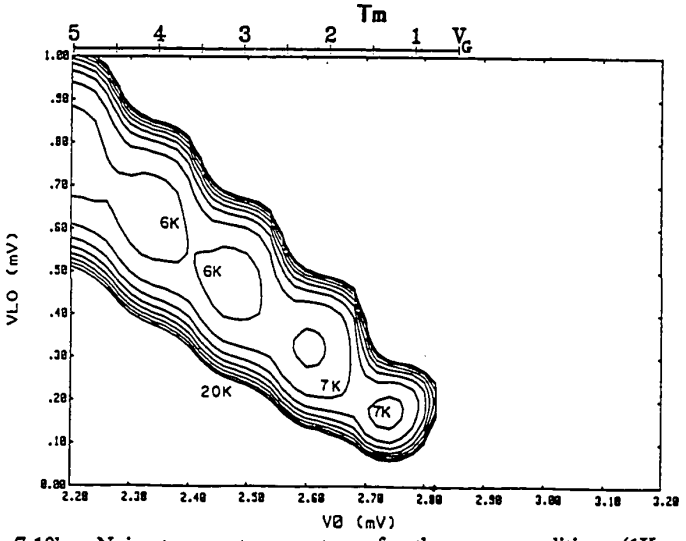

Fig. 7-10b Noise temperature contours for the same conditions (1K contour interval). The gap voltage and the center of each photon step below the gap (2.85 mV) are labeled at the top of each plot.

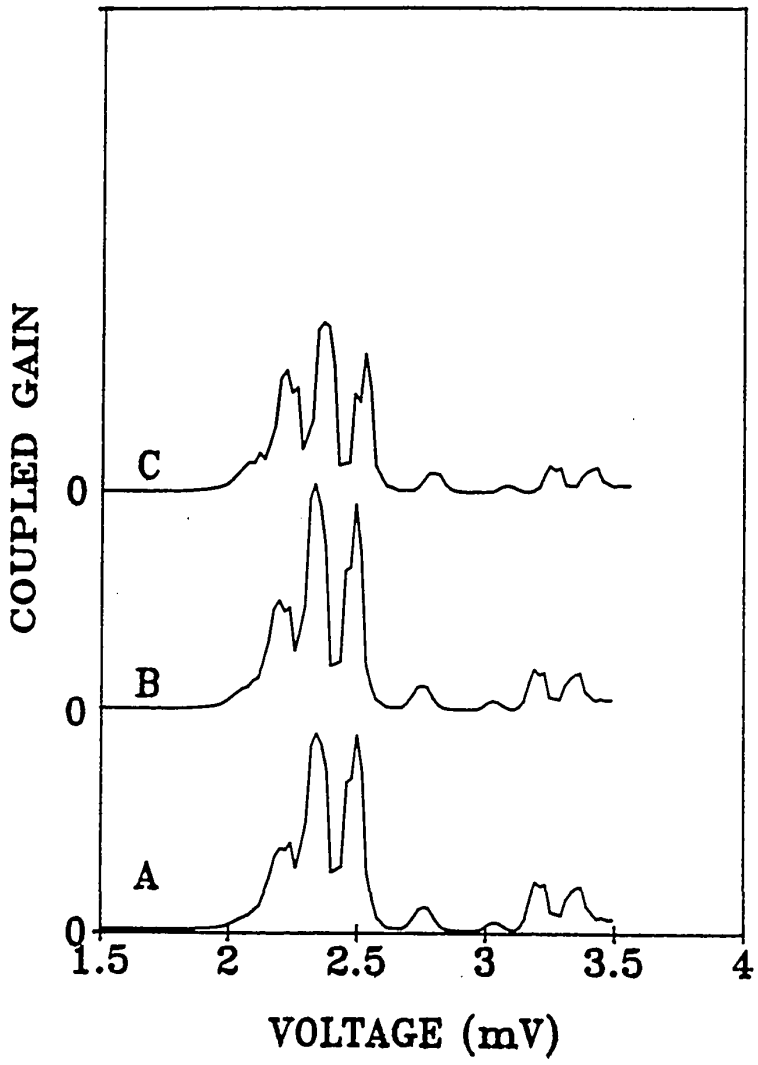

Fig. 7-11 Calculated variation of the coupled gain with DC bias for the Nb junction at 4.2K with a shorted image and an IF impedance of A.) Z_i = 50 Ω B.) 100 Ω C.) 100 + j 100 Ω (Zeros offset for clarity). Compare these curves with the experimental data in Fig. 6-4b.

region on the fourth photon step in Fig. 7-10 which indicates that we have found the best combination of V_{LO}, V_O, and Z_S.

The shorted image calculations discussed above also show that the largest mixer gain is obtained on the fourth photon step. This aspect of the calculations also agrees with the experiment. A calculation of the coupled gain vs V_O plotted in Fig. 7-11 agrees well with the experimental plot in Fig. 6-4b. We note that image terminations other than $Z_i \simeq 0$ do not agree as well with the experimental results. An open circuit image (with C_J in parallel), for example, predicts a large coupled gain (into 50 Ω) of 8 dB on the first photon step and a much smaller coupled gain of -2 dB on the fourth step. Based on all of the modeling performed, it appears that a shorted image three port model qualitatively predicts the experimental data for the Nb junction at 4.2K quite well. Exact comparisons, however, reveal a clear overestimation of the gain and underestimation of the noise.

7.2.2 Modeling of Nb Results at 1.3 K

When the Nb junction is cooled from 4.2 K to 1.3 K, the I-V becomes considerably sharper and has a much lower subgap current as shown in Fig. 6-5a and discussed in chapter 6. The improved I-V and lower physical temperature cause the mixer gain to improve by a factor of two from .27 to .56 and the noise temperature to drop by a factor of almost two from 9.0 K to 5.5 K. This junction now shows much stronger quantum effects as indicated by the sharper steps on the pumped I-V in Fig. 6-5a and the stronger modulation of coupled gain with DC bias voltage in Fig. 6-5b. Clearly, this junction should be a stronger test of the predictions of the quantum mixer theory.

The predicted pumped I-V (voltage driven) is shown in Fig. 6-5a just above the experimental curve. The required V_{LO} of .675 mV can now be

used to generate the Y and H matrices and to predict mixer gain and noise for various Z_S, Z_i, and Z_{IF}. The available gain for Z_i = (0,0) and a range of Z_S is shown in Fig. 7-12a. The mixer noise for the same range of parameters is shown in Fig. 7-12b. The most notable difference from the previous plots in Figs. 7-7 and 7-8 is the appearance of a region of infinite available gain for small values of the real part of Z_S. The imaginary part of Z_S still approximately tunes out the junction capacitance for best (i.e. infinite) available gain. A careful examination of similar contour plots with different image impedances reveals that an open circuited image produces the largest region of infinite gain. A similar conclusion has been reached by D'Addario, (1985). The effect of the image impedance on mixer gain is discussed further in Appendix B. The noise contour plot predicts a mixer noise of ~ 4K which is reasonably close to the experimentally measured value of 5.5 ± 0.8K reported in chapter VI, but still outside of the error limits.

The fact that we did not observe infinite G_A or even $G_A > 1$ in this experiment is somewhat surprising based on the reasonably good agreement between experiment and theory obtained for the same junction at 4.2 K. The results of the modeling at 4.2K indicate that we should easily produce the right range of Z_S to see large gain. Since the experimental values of the screwtuner and backshort position are virtually identical for the experiments at 1.3K and 4.2K, it appears very unlikely that there is an impedance matching problem with Z_S. One possibility is that by optimizing the mixer for best coupled gain we have missed regions of large available gain. This is not usually a problem when the mixer sees the same impedance at the LO, signal and image frequencies because flat steps or negative resistance appear on the pumped I-V to indicate large available gain. When the LO impedance is significantly different from the signal impedance, as it is in our case, the correlation of flat or negative resis-

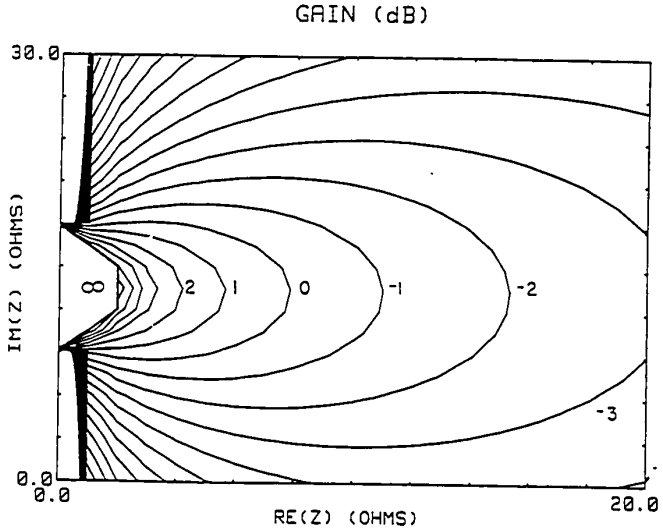

Fig. 7-12a Contour plot of available gain G_A vs. Z_S for Nb at 1.3K on the fourth step using V_{LO} = .675 mV with a shorted image impedance (Z_i = 0.01 + j0.01 Ω); the infinite gain regions are clearly visible. The experimental gain was G_A = -2.5 dB.

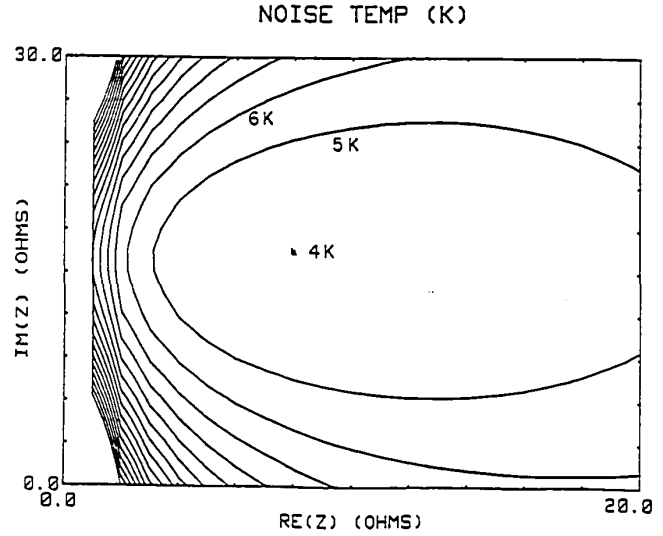

Fig. 7-12b Noise temperature contour plot for the conditions in 7-12a. The experimentally measured noise was T_M = 5.5 ± 0.8K.

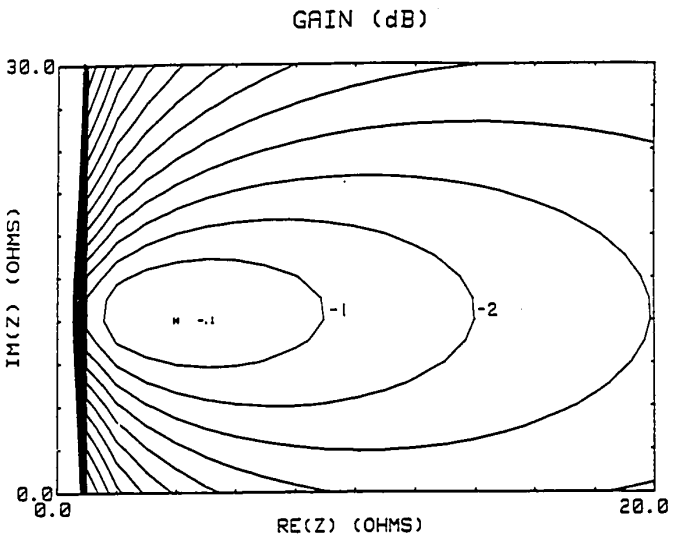

Fig. 7-13 Contour plot of the coupled gain vs. Z_S for Nb at 1.3K on the fourth photon step with an IF impedance of Z_{IF} = 50 Ω.

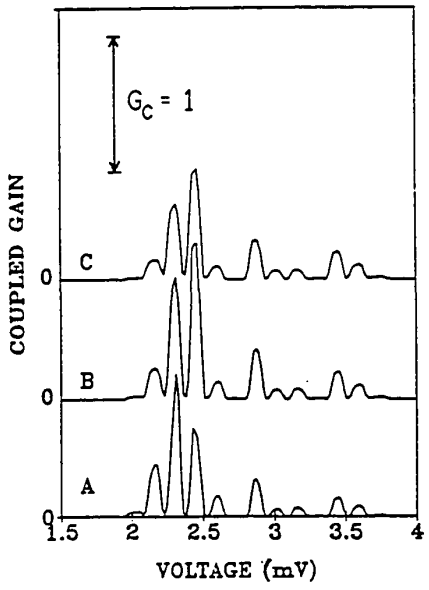

Fig. 7-14 Calculated coupled gain G_C vs. DC bias V_0 for the Nb junction at 1.3K with a shorted image and an IF impedance of Z_{IF} = 50 Ω (Zeros offset for clarity). Compare with the experimental curve in Fig. 6-5b.

tances steps with large available gain no longer exists. In fact, as pointed out in chapter VI, the tuning conditions that produce flat steps on the pumped I-V produce very poor mixer performance. In order to check for the possibility that by maximizing the coupled gain we may not locate regions of large available gain, we have calculated the coupled gain with a 50 Ω IF load impedance for a shorted image and plotted it in Fig. 7-13. The shorted image was chosen because it gave the best fit to the 4.2 K data as discussed in 7.2.1. Recall that for the rounded I-V at 4.2 K the best coupled gain was very close to the best available gain. By comparing Fig. 7-13 and Fig. 7-12a, it is clear that the best available gain does not occur for the best coupled gain on the fourth photon step due to an impedance mismatch at the IF port. Based on Fig. 7-13, it appears that we could have missed large available gain. We should, however, have measured a large reflection coefficient at the IF port which we did not observe. Unfortunately, we have not been able to directly measure the actual IF load impedance in our system, but we know from the experiments at 4.2 K and others with Pb-alloy junctions [McGrath, 1985] that the impedance mismatch is small when the mixer is optimized. This indicates that the IF impedance should not be too different from 50 to 100 ohms or else a large IF mismatch would have been observed in the previous experiments using more rounded I-Vs. This analysis shows that large and infinite available gain should exist for mixing on the fourth photon step but that an IF impedance mismatch may make it difficult to find the large available gain in our experiment.

We have also calculated the dependence of coupled gain on DC bias when the junction is optimized for best performance on the fourth photon step. This plot is shown in Fig. 7-14 for a shorted image and several IF impedances. The similar experimental result for comparison is shown in Fig. 6-5b. The theory in this case accurately predicts the relative variation

of coupled gain. The absolute magnitude, however, is off by a factor of 2 or 3 dB. Other image impedances give a much poorer fit to the experiment.

The theoretical discrepancies for mixing on the fourth step become even worse for mixing on the first photon step. In this case, the theory predicts that the entire range of impedances used for Z_S ($Re(Z_S)$ = 0-20 Ω and $Im(Z_S)$ = 0-30 Ω) produces infinite available gain if the image is open circuited or terminated in the scale model value of $Z_i \simeq 5 - j100$ Ω. The only image impedance that gives a reasonable range of finite gain is a short circuit. The available gain for mixing on the first step with a shorted image is virtually identical to that obtained for Ta on the first step and illustrated in Fig. 7-18. As the image impedance is gradually increased from zero, the size of the infinite gain region increases until it totally fills the range of Z_S space shown. As discussed in Appendix C, choosing $Z_i=0$ is expected to produce the smallest region of Z_S space with infinite available gain. Even under these worst case conditions, the theory still predicts a significant region of accessible signal impedances that should produce large or infinite available gain. This performance was not observed for the Nb junction at 1.3 K on the first step. In order to check that we are not being misled by optimizing for large coupled gain, we have also calculated the coupled gain for the case of a shorted image and a 100 Ω IF load. These calculations clearly show that we should have been able to achieve large coupled gain (G_C > 0 dB) and infinite available gain by optimizing the coupled gain. Even if we did not find the infinite gain region, we should have at least found G_C > 0 dB and a large reflection coefficient at the IF port. This was not observed. Based on this disagreement for the gain on first photon step, we must conclude that the three port quantum mixer theory does not accurately predict the gain of strong quantum mixers near the gap voltage. The noise predictions are also measurably less than the experiment by at least 1K.

7.3 Gain and Noise vs Photon Step for Ta at 1.3 K

As mentioned in chapter VI, the experimental study of gain and noise in these Ta and Nb junctions represents the most accurate study to date for mixers strongly in the quantum regime. This study of gain and noise versus photon step is a strong test of the adequacy of the three port quantum mixer theory and again demonstrates the need for improvements especially near the sum gap.

Because it appears, from the previous sections, that the assumption of a shorted image produces the best fit to our experiments we will concentrate on the shorted image calculations for these Ta experiments although extensive calculations have also been performed with other image impedances. The theoretical voltage driven pumped I-Vs for each bias voltage are shown in Fig. 7-15 and are in reasonable agreement with the actual experimental curves shown in Fig. 6-7. The required values of V_{LO} to produce each curve are given in the figure caption and used for calculating the Y and H matrices to predict mixer gain and noise for each bias voltage. The available mixer gain and noise for a shorted image frequency at each experimentally measured bias voltage are shown in Figs. 7-16 to 7-18 for the same range of Z_S as the Nb junction discussed above. The predicted values of mixer noise temperature are significantly below the experimental values by a factor of 1.5 to 2.

The model calculations for coupled and available gain also disagree strongly with the experiment in that they predict large regions of infinite available gain for values of the signal impedance that should be easily produced by our mixer block. Notice that the size of the infinite gain region increases for photon steps that are closer to the sum gap. This is contrary to our experiment which shows decreasing available gain for photon steps closer to the sum gap. As discussed in Appendix C, these shorted image calculations should produce the smallest regions of infinite

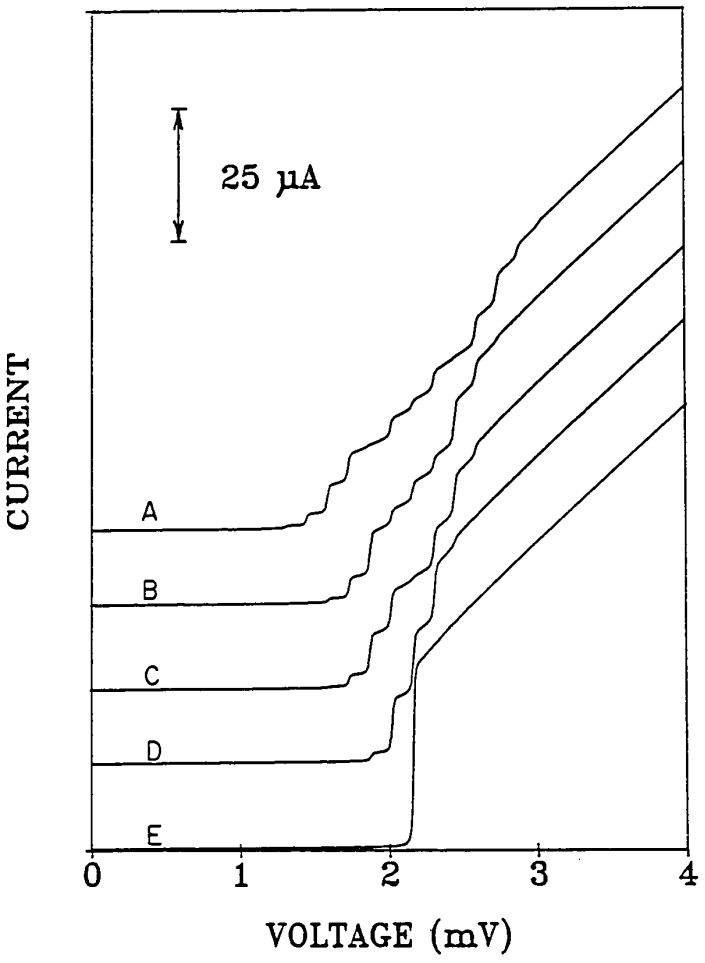

Fig. 7-15 Calculated voltage driven pumped I-Vs for Ta junction with best gain on the A.) fourth photon step (V_{LO} = 0.7 mV) B.) 3rd to 4th photon point (V_{LO} = 0.45 mV) C.) second photon step (V_{LO} = 0.38 mV) D.) first photon step (V_{LO} = 0.2 mV). The curve labeled "E" is the unpumped DC I-V.

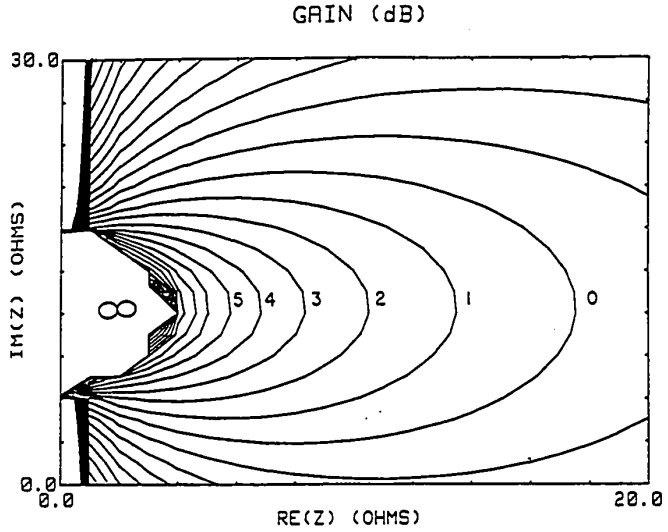

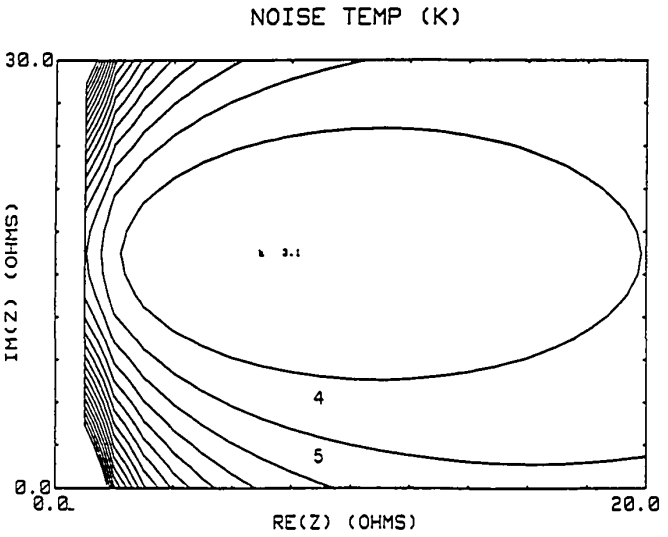

Fig. 7-16 Contour plot of the available gain and noise temperature vs. the signal impedance Z_S for the Ta junction on the fourth photon step with a shorted image port (V_{LO} = 0.7 mV). The experimental gain was G_A = 1.1 (0.4 dB) and the noise temperature was T_M = 5.2±0.5K.

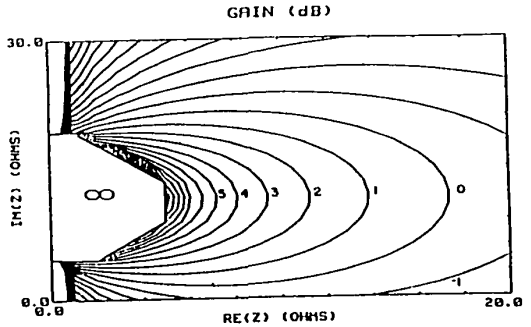

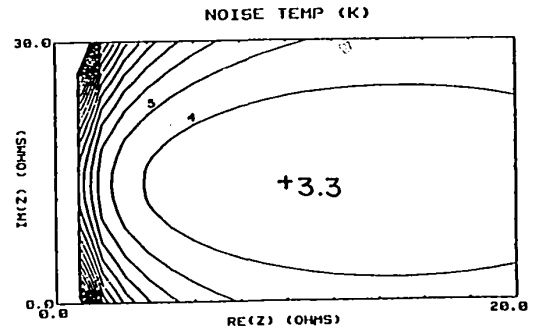

Fig. 7-17 Contour plot G_A and T_M vs. the signal impedance Z_S for the Ta junction on the second photon step with a shorted image port (V_{LO} = 0.38 mV). The experimental results were G_A = 0.58 (-2.4 dB) and T_M = 5.7±0.5K.

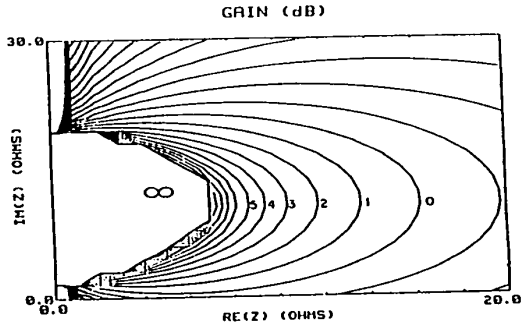

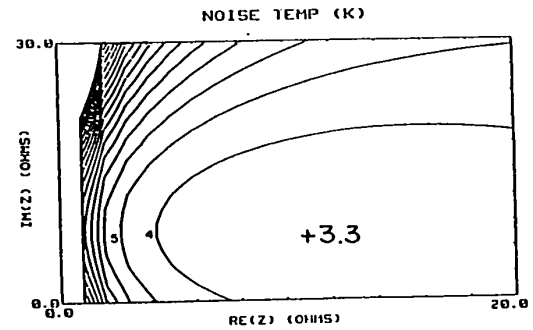

Fig. 7-18 Contour plot G_A and T_M vs. the signal impedance Z_S for the Ta junction on the first photon step with a shorted image port (V_{LO} = 0.20 mV). The experimental results were G_A = 0.4 (-4.0 dB) and T_M = 6.0±0.5K.

available gain so that other image terminations will only make the theoretical disagreement worse. Additional calculations of the coupled gain for several IF impedances (not shown) indicate that it is virtually impossible to miss the regions infinite available gain by optimizing the mixer based on the coupled gain. This implies that we should have measured a large IF mismatch and large available gain for each of our experimental bias voltages which is clearly not the case. The source of this disagreement is currently unknown although several possibilities are discussed in section 7.5.

Despite the disagreement in available gain, we have calculated the variation of coupled gain with DC bias for a fixed signal impedance of 3 + j 15 Ω and a 50 Ω IF impedance. This calculated curve matches the relative variation of the experimentally observed coupled gain with DC bias in Fig. 6-8 reasonably well except for a multiplicative factor of about 5.

7.4 Modeling Ta at 1.3 K and 2.08 K - Noise from Subgap Currents

As discussed in chapter 6, the Ta I-V curve at 1.3 K has a very low subgap conductance which allows us to achieve low values of mixer noise and receiver noise with these junctions. In order to compare the experimental results for the variation of mixer noise due to increased subgap conductance with the theory, we have modeled the mixer noise for the Ta junction at two temperatures (1.3K and 2.08K). As is the case for the Nb junction at 1.3 K and the additional Ta measurements discussed in section 7.3 above, the theoretical mixer gain is still much larger than the measured value for these sharp junctions and the source of this disagreement is currently unresolved. Setting these considerations aside, however, and concentrating on the noise predictions, we have plotted the predicted noise temperature for the actual experimental conditions of operation on the fourth photon step. The theoretical and experimental pumped I-V is virtually identical to that discussed in the previous section for the best

gain on the fourth step and is shown in Fig. 7-15. The predicted variation of the mixer noise temperature with Z_S at the operating temperature of 2.08 K is shown in Fig. 7-19. The noise prediction for 1.3 K operation is shown in Fig. 7-16. Clearly the absolute magnitude of the noise is lower than the experiment by approximately 2 K, but the relative increase in noise of 0.4K due to the different operating temperature and increased subgap current agrees well with the experiment. The inclusion of higher harmonics should increase the theoretical noise prediction somewhat due to mixed down thermal noise but the magnitude of this effect is not known at this time and would surely depend on the embedding impedances at the harmonic frequencies.

7.5 Comparison with Other Work

A number of authors have compared experiment and theory for SIS mixers and these efforts have recently been reviewed by Tucker and Feldman, (1985). Feldman et al. (1983), for instance found excellent agreement between their experimentally measured gain and the gain predicted by the three port theory. These authors used embedding impedances from a scale model and found that the gain varied as predicted for changes in the backshort position. The junctions modeled in this work, however, were slightly rounded on the voltage scale of $\hbar\omega/e$ and did not produce large gain (G_C = -10 dB). An extensive series of measurements was compared with the gain predictions of the three port theory by Feldman and Rudner, (1983). These authors found reasonable agreement for low gain mixers with an $\omega R_N C_J$ product of less than ~ 4 (see also section 2.3.7 in chapter II for additional discussion). These authors also observed depressed mixer performance on the first photon step and attributed the effect to the influence of harmonic frequencies. Shen and Richards, (1981), also found depressed performance on the first step which was attributed to

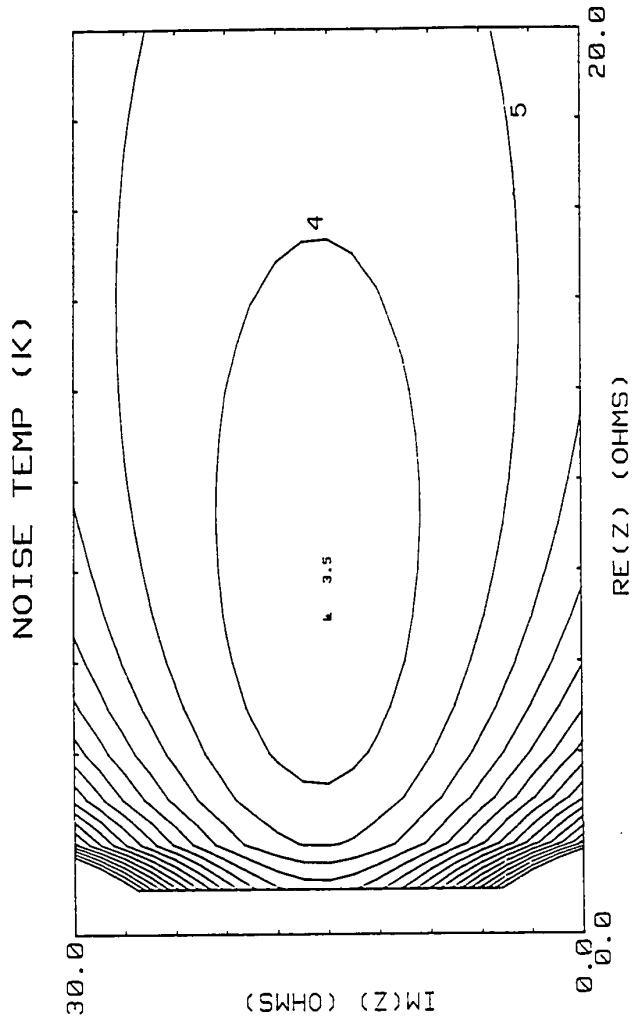

Fig. 7-19 Mixer noise temperature for Ta on the fourth photon step at 2.08K showing an increase in noise of ~ 0.4K compared to otherwise the same conditions in Fig. 7-16.

TABLE 7-1 Summary of the theoretical predictions for mixer performance compared to the appropriate experiment discussed in chapter VI. The theoretical input noise power θ_M is shown in units of $\hbar\omega_B$. These noise powers can be converted to noise temperatures as discussed in Ch. II with the Planck radiation law. The theoretical gains are close to the experimental values only for low gain mixers.

Junction $R_N(\Omega)$	Photon step	G_A(SSB) Exp.	G_A(SSB) Theory	$\theta_M(\hbar\omega_B)$ Exp.	$\theta_M(\hbar\omega_B)$ Theory
72 (Nb)	4	0.56	∞	2.8	1.9 - 2.5
	4	0.27[a]	0.4	4.9	2.7 - 3.1
44 (Ta)	4	1.1	∞	2.7	1.4 - 1.9
	4	1.1[b]	∞	2.9	1.7 - 2.2
	3-4	0.064	0.080	4.1	1.6 - 2.2
	2	0.58	∞	3.0	1.5 - 1.9
	1	0.39	∞	3.1	1.5 - 1.9

a) measured at a bath temperature of 4.2K.
b) measured at a bath temperature of 2.08K.

harmonic effects. These authors also performed a five port calculation to qualitatively confirm this effect. Recent work by D'Addario has modeled the performance of moderate gain mixers ($G_A \approx 0$ dB) with some success and also shown the importance of the image impedance. All of the comparisons discussed above are concerned only with the gain predictions of the quantum theory. Our work is new in that it also compares with the noise predictions of the theory.

7.6 Summary and Conclusions

The work discussed in this chapter has modeled a number of different aspects of the mixer experiments discussed in chapter VI. A summary comparison of the results of these calculations with the experiments is provided in Table 7-1. The main conclusion is that the three port quantum mixer theory underestimates the noise power of our mixers by a factor of 1.5 to 2.0. This is equivalent to an excess noise temperature of 1K to 3K. This is true for sharp as well as rounded I-V curves. The gain predictions of the three port theory are larger than the experiment by ~ 2 dB for mixers that do not show strong quantum effects. The detailed nature of the theoretical discrepancy and its dependance on photon step and embedding impedance has also been illustrated. The cause of the theoretical discrepancy for mixers showing strong quantum effects is thought to be related to harmonic effects but this has not been confirmed.

VIII. SUMMARY AND CONCLUSIONS

The work described in this thesis has addressed a number of important issues related to the fabrication and measurement of SIS quasiparticle mixers. A new deposition technique, ion-beam deposition, was developed and shown to produce high quality refractory superconducting films of Nb and Ta. This technique works well with room temperature substrates and photoresist processing. The use of a thin Nb underlayer was also found to be important in controlling the crystal structure of Ta films. A new step defined junction fabrication technique was developed and found to be very useful in producing high quality Ta junctions for the SIS mixer experiments. These Ta junctions have a very sharp current rise at the sum gap and very low subgap leakage currents. The sharp I-V characteristics show strong quantum mixing effects at 36 GHz. In particular, an input noise power within a factor of two of the quantum limit and large mixer gain (G_A and $G_C > 1$) were measured. The large gain and low noise of these mixers has allowed us to achieve a receiver noise temperature as low as 24±1K which is the lowest reported to date for a heterodyne receiver. Additional experiments with a low IF of 25 MHz demonstrate the importance of equal signal and image terminations for achieving large mixer gain. Comparison of the mixer results with the three port quantum mixer theory shows that the experimentally measured mixer noise power is consistently less than that predicted by the theory by a factor of 1.5 to 2. The experimentally measured gain is considerably less than the theoretical predictions for mixers that show strong quantum effects. Although harmonic effects may be important, the cause of this discrepancy has not been resolved. Nonetheless, the junction and mixer results obtained in this thesis work represent a significant advance in the fabrication, measurement, and understanding of SIS mixers.

APPENDIX A

Standard Step Defined Junction Process Steps

I) Si Wafer Cleaning

a) Ultrasonic (US) cleaning in Alconox solution and scrub with Scotch Brite scouring pad for 3 min.

b) DI water rinse and US in DI for 60 sec.

c) US in acetone for 3 min followed by US in isopropanol for 3 min.

d) Blow dry with dry N_2

e) Dip in 20% HF/H_2O etch for 30 sec then DI water rinse 1 min

f) US in isopropanol for 1 min then blow dry with N_2

g) Preclean the RIE system with O_2 for 10 min or until a green color discharge has been maintained for at least 5 min.

h) Reactive Ion Etch for 5 min in pure O_2 - P = 3.5 mTorr, self bias J_s = -430 volts.

II) Chromium line mask patterning for RIE

a) Bake wafers on the hot plate at ~200°C for t > 10 min.

b) Remove and place on the spinner, wait ~20 sec, then flood coat the wafer with AZ1350B resist and spin at 5000 RPM for 60 sec.

c) Bake on the hot plate at 85°C for 20 min.

d) Expose the wafer with the line mask pattern in the mask aligner for ~ 80 sec.

e) Develop in AZ developer 1:1 diluted with DI water for ~60 sec.

f) DI rinse for 60 sec and blow dry with N_2.

g) Load into the evaporator and evaporate ~500 Å of Cr from a rod source at 10-15 Å/sec. P ≈ 1 x 10^{-6} Torr during evaporation.

h) Lift off the Cr by US in acetone for ~ 60 sec followed by US in isopropanol for ~60 sec. If several wafers are being processed be sure to use fresh solvents each time. Blow dry with dry N_2.

III) Reactive Ion Etching (RIE)

a) Preclean the RIE system with O_2 for 10 min or until a green color discharge has been maintained for at least 5 min.

b) Load the wafer into the RIE (do only one at a time to avoid loading the etch gas with reaction products).

c) Clean the wafer by running an O_2 RIE for 90 sec at 3.5 mTorr with the "J" head self bias at $J_s \simeq -400$ V.

d) Etch with 10% O_2 / 90 % CF_3Br for 13 min (etch rate $\simeq$ 500 Å/min) $J_s \simeq 400$ V.

e) Post clean in O_2 for 60 sec with $J_s = -400$ V.

f) Etch off the Cr mask lines in Cr etch (Transene Cr mask etch). This takes 10 to 15 min at 28°C.

g) Rinse off the Cr etch with solution of 20% nitric acid and water.

h) DI rinse for 60 sec and blow dry in N_2.

IV) Two Layer Resist

a) Bake the wafers at T $\simeq$ 200°C for at least 10 min on a hot plate.

b) Put the wafer on the spinner and flood with AZ1350J. Do not use HMDS as an adhesion promoter because it strongly affects the sensitivity of the resist.

c) Spin at 5000 rpm for 60 sec.

d) Bake on the hot plate at 83°C for 20 min

e) Wait at least 10 min and then blanket expose the wafer for 5 min in the mask aligner.

f) Evaporate 500 Å of aluminum at ~ 20 Å/sec with a pressure in the system of ~ 10^{-6} Torr.

g) Flood and spin AZ1370 at 5000 rpm for 60 sec.

h) Wait at least 30 min and then bake at 83°C for 20 min. Some

wrinkling of the Al isolation layer may occur but this does not seriously affect the process.

V) Pattern exposure and development

a) Expose top level of resist with the lead mask for 80 sec in the mask aligner by aligning to the steps in the Si substrate which should be visible as distortions of the resist surface.

b) Develop in AZ 1:1 diluted developer for 30 sec.

c) Scribe into six-junction sections (216 mils wide).

d) Project the small junction section with the Zeiss microscope being careful to align the narrow slot over the step for the junction. See Fig. 4-3b. The lamp was a 50 watt Zeiss Hg vapor lamp. An aperture setting of 1.0 and an exposure time of ~ 7.5 sec was used on the Zeiss with a 40x lens (Epiplan 40/0.85 Pol).

e) Step and repeat and then develop in AZ 1:1 for 45 sec.

f) Rinse in DI water for 30 sec and go to g) without drying

g) Etch the aluminum isolation layer with commercial Al etch with surfactant for 10 sec after the patterned area becomes dark. If the Al etch does not have a surfactant, skip step f) and go straight from the resist developer to the Al etch since the developer does have a surfactant.

h) Rinse in DI water for 60 sec.

i) Develop the bottom layer for the desired undercut by testing a sacrificial piece of the wafer first. A development time of 25 - 35 sec was usually required (and optimal) to clear the bottom layer down to the substrate in the exposed areas. The substrate is now ready for metal deposition and tunnel barrier formation as discussed in chapter IV.

APPENDIX B

Effect of the Image Impedance

As pointed out in chapter II, the image impedance can have a significant effect on the conversion efficiency of SIS mixers. The simplified calculations presented in this appendix show how different image impedances can affect the range of signal impedances that produce large or infinite gain. It will be shown that a shorted image is the worst situation in that it allows the smallest range of signal impedances to produce infinite gain. An open circuited image is the best while an equal signal and image termination (a double sideband mixer) produces intermediate results.

As discussed in chapter II, the output admittance of a Y-mixer is given by

$$Y_{IF} = G_{00} - G_{01} \times \left[\frac{(Y_{10}(Y_{-1-1} + Y_i) - Y_{-10}Y_{1-1} + Y_{-10}(Y_{11} + Y_S) - Y_{-11}Y_{10})}{(Y_{11} + Y_S)(Y_{-1-1} + Y_i) - Y_{-11}Y_{1-1}} \right] \qquad \text{B-1}$$

Where Y_S and Y_i are the signal and image admittances respectively. Since it is known that the output admittance goes to zero when the mixer gain goes to infinity, we can solve the equation $Y_{IF}=0$ to find the admittances that define the boundary between infinite and finite gain. If the real part of Y_{IF} is less than zero, the gain will be infinite. If, on the other hand, the real part of Y_{IF} is positive the gain will be finite. For the purpose of these simplified calculations we will assume that all of the reactive components of the Y matrix and external impedances are zero since they turn out to be unimportant in practice. In this case, the condition for infinite available gain (derived from $Re(Y_{LO}) < 0$) can be shown to be,

$$(G_S - G_o)(G_i - G_o) \leq (G_{01}G_{10}/G_{00} - G_{1\text{-}1})^2 \qquad \text{B-2}$$

where

$$G_o = (G_{01}G_{10}/G_{00} - G_{11}) \qquad \text{B-3}$$

This relationship is shown graphically in Fig. B-1 for a positive value of G_o. From this relation and the figure, it should be clear that a small value for G_i (i.e. an open circuit image) allows the largest range of G_S to satisfy the inequality. A large or infinite value for G_i (i.e. a short circuited image), on the other hand, allows the smallest range of values for G_S to satisfy the inequality and produce infinite gain. The situation where $G_i = G_S$ clearly represents an intermediate case.

The region of the G_S G_i plane that produces infinite gain is clearly dependent on the value of G_0 and we examine several cases below.

1) $\underline{G_o \geq 0}$ In this case, infinite gain will be possible for any image conductance if a small enough G_S is used. Image conductances that are less than G_0 produce infinite gain for any signal conductance.

2) $\underline{G_o < 0}$ In this case, a shorted image will not allow infinite gain for any value of the signal conductance. The largest value of G_i that allows infinite gain to be achieved (for very small G_S) is given by setting $G_S = 0$ in Eq. B-2 and solving for G_i. Eventually, when G_0 becomes sufficiently negative, no values of G_S or G_i will exist that produce infinite gain. Graphically, this corresponds to moving the curve in Fig. B-1 closer and closer to the origin until eventually the entire curve is on the negative side of the G_S and G_i axes. The conditions under which infinite gain is no longer possible (i.e. the curve has totally crossed both conductance axes) can be found from Eq. B-1 by setting $G_S = G_i = 0$. The result is the familiar inequality (see chapter two)

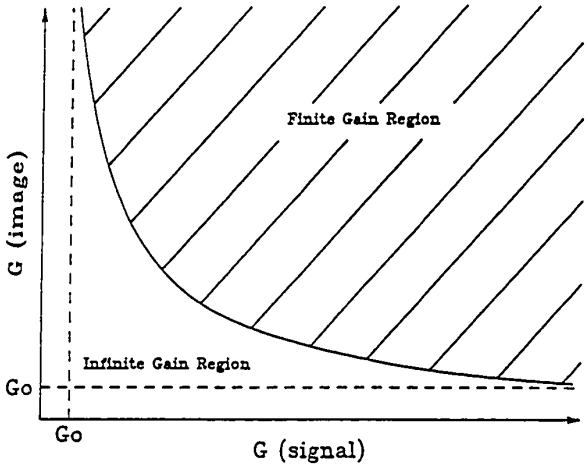

Fig. B-1 Plot showing regions of infinite available gain for different signal and image conductances. Note the large regions of infinite available gain for small image conductances.

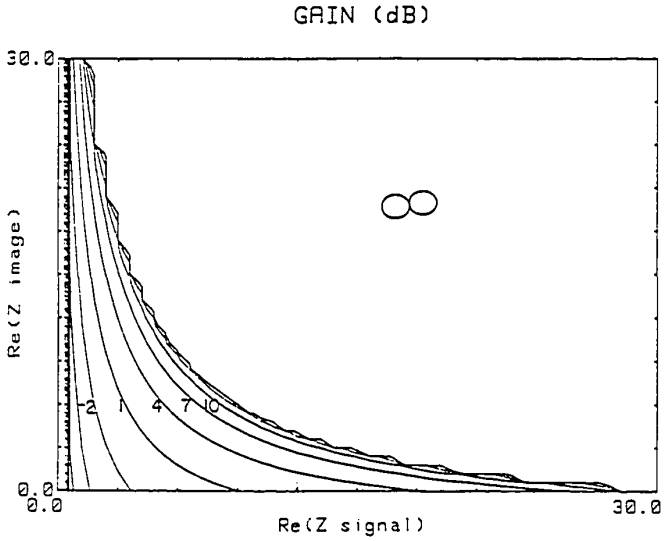

Fig. B-2 Plot of available gain vs. the real part of the signal and image impedance for the Ta junction (44 Ω) optimized on the first photon step. Note the large region of infinite G_A for an open circuit image.

$$\eta = \frac{2G_{01}G_{10}}{G_{00}(G_{11} + G_{1-1})} > 1 \qquad \text{B-4}$$

which must be satisfied to allow infinite gain somewhere in the positive G_s G_i plane. If B-4 is not satisfied, then no values of G_s or G_i will produce infinite gain. It has been shown by several authors [Tucker, 1979 and Torrey and Whitmer, 1948] that η is always less than one for a classical resistive mixer. It is only the quantum theory that allows $\eta > 1$ and infinite gain.

Fig. B-2 shows the calculation of available gain for the sharp Ta junction of chapter 6 optimized on the first photon step. The axes are now impedances so that the finite and infinite gain regions are interchanged from figure B-1. This calculation includes the reactive terms in the Y matrix and demonstrates that ignoring them in Fig B-1 does not change the basic results of the analysis. Fig. B-2 clearly shows that a shorted image allows the smallest range of signal impedances to produce infinite gain. An open circuited image allows the widest choice of signal impedances. In fact, any signal impedance will produce infinite gain under these conditions if the image is open circuited. The fact that an open circuit image is beneficial for SIS mixers has been noticed before by D'Addario [D'Addario, 1985] but this has not been previously demonstrated analytically. As also pointed out by D'Addario, an open circuit image is difficult to achieve experimentally due to the large SIS junction capacitance which must be tuned out. The competing goal of broadband tuning also makes an open circuit image impractical.

APPENDIX C

Accuracy of the Mixer Calculations

A number of steps have been taken to assure the accuracy of the computer calculations presented in this thesis. This is necessary because the calculations are quite involved with a number of series summations, numerical integrations, and matrix inversions. As discussed in chapter II and VII, the Y and H matrix elements require the summation of a large number of Bessel function weighted currents from the I-V curve and the Kramers Kronig transform. In order to verify the accuracy of the Y and H matrix elements, the following tests have been made:

A) The Bessel function routine has been verified to 10 digit accuracy by comparison with the values in Abromowitz and Stegun (1972) for large and small orders as well as large and small arguments. The number of terms in each Bessel function weighted summation is then determined so that the summations are accurate to 8 digits.

B) A simple test has been run to calculate the Y and H matrices for an ideal 50 Ω BCS I-V curve with a sum gap of 2.0 mV. The bias voltage was V_0 = 1.925 mV, the LO voltage amplitude was $V_{LO} = \hbar\omega/e$ = .145 mV so that $\alpha = eV_{LO}/\hbar\omega = 1$ with ν_{LO} = 35 GHz and ν_{IF} = 250 kHz. Under these conditions, the pumped dc current at the bias voltage was 6.84 μA and the complex Y matrix (normalized to 1/50 mhos) was,

$$Y = \begin{vmatrix} (4.5436, -1.0358) & (0.2633, -3.0195) & (-0.5358, 0.1675) \\ (3.8765, 0.0000) & (0.2467, 0.0000) & (3.8765, 0.0000) \\ (-0.5358, -0.1675) & (0.2633, 3.0195) & (4.5436, 1.0357) \end{vmatrix}$$

and the real H matrix (normalized to 1/50 mhos) was,

$$H = \begin{vmatrix} 1.3601 & 0.7352 & 0.3206 \\ 0.7352 & 0.6843 & 0.7352 \\ 0.3206 & 0.7352 & 1.3601 \end{vmatrix}$$

Clearly, these matrices satisfy the required symmetry properties that $Y_{01} = Y^*_{0-1}$, $Y_{00} = G_{00}$, $Y_{01} = Y_{0-1} = G_{01}$ (G is a purely real number), $Y_{-10} = Y^*_{10}$, $Y_{-11} = Y^*_{1-1}$, $Y_{-1-1} = Y^*_{11}$, $H_{10} = H_{01} = H_{-10} = H_{0-1}$, $H_{11} = H_{-1-1}$, $H_{11} = H_{-11}$. The Bessel function weighted sums were taken out to 32 terms for these calculations. A separate program which was independently developed by M.J. Wengler at Caltech produces the same Y and H matrices within 1% accuracy. That program uses fewer terms in the Bessel function sums and so is less accurate.

C) The non-linearity parameter η discussed in chapter II and appendix B has been evaluated under a large number of V_0 and V_{LO} conditions and is always seen to approach a value of 2 for ideal BCS junctions and sharp Ta junctions as required by the theory [Feldman, 1982]. The rounded I-V junctions such as Pb-alloy at 1.3K and Nb at 4.2K give values of η which are always < 1. When η is < 1 the calculated gain is always < 0 dB as required by the theory.

D) The calculated SSB noise temperature also approaches the quantum limit $\hbar\omega/k\ln 2 \simeq 2.5$K under the optimum conditions with a BCS I-V. The Ta junctions produce calculated noise temperatures as low as 2.7K.

E) The calculated gain on the first photon step discussed in chapter VII always minimizes for values of $\alpha \simeq 2.4$ ($V_{LO} \simeq 0.34$ mV). This agrees with the theoretical prediction of Smith and Richards (1982) where $\alpha \simeq 2.4$ is the first root of the equation

$$\sum_{n=1}^{\infty} \frac{\partial J_n^2(\alpha)}{\partial \alpha} - \frac{\partial J_0^2(\alpha)}{\partial \alpha} = 0 \qquad \text{C-1}$$

REFERENCES

Abramowitz, M. and I.A. Stegun, Editors, Handbook of Mathematical Functions, (Dover, New York, 1972).

Alessandrini, E.I., R.B. Laibowitz, and J.M. Viggiano, J. Vac. Sci. Technol. 18, 318 (1981).

Ambegaokar, V. and A. Baratoff, Phys. Rev. Lett. 10, 486 (1963).

Anderson, P.W., J. Phys. Chem. Solids 11, 26 (1959).

Arnold, G.B., J. Low Temp. Phys. 59, 143 (1985).

Arnold, G B., Phys. Rev. B18, 1076 (1978).

Atkinson, A., Rev. Mod. Phys. 57, 437 (1985).

Bardeen, J. and J.R. Schrieffer, Progress in Low Temperature Physics, Vol. 3, North Holland, Amsterdam, p. 231 (1961).

Bardeen, J., L. Cooper, and J.R. Schrieffer, Phys. Rev. 108, 1175 (1957).

Barner, J.B. and S.T. Ruggiero, IEEE Trans. Magn. MAG-23, to be published (1987).

Barone, A. and G. Paterno, Physics and Applications of the Josephson Effect, Wiley, New York (1982).

Beasley, M.R., IEEE Trans. Electron Dev., ED-27, 2009 (1980).

Bending, S.J. and M.R. Beasley, Phys. Rev. Lett. 55, 324 (1985).

Bispinick, H., Applied Physics, 113 (1979).

Blaney, T.G., in Infrared and Millimeter Waves, K.J. Button Ed., pg. 62 (Academic, New York, 1980).

Blonder, G.E., M. Tinkham, and T.M. Klapwijk, Phys. Rev. B25, 4515 (1982).

Bostock, J.L. and M.L.A. MacVicar, in Anisotropy Effects in Superconductors, H.W. Weber, Editor, Plenum, New York, (1977).

Bouchier, D., G. Gautherin, B. Agius, and S. Rigo, J. Appl. Phys. 49, 5896 (1978).

Braginski, A.I., J.R. Gavaler, M.A. Janocko, and J. Talvacchio, Proceedings of the International Cryogenic Materials Conference, 1986 (to be published).

Brinkman, W.F., R.C. Dynes, and J.M. Rowell, J. Appl. Phys. 41, 1915, (1970).

Broom, R.F., S.I. Raider, A. Oosenbrug, R.E. Drake, and W. Walter, IEEE Trans. Electron Dev. ED-27, 1998 (1980).

Campbell, C.K., R.C. Dynes, and D.G. Walmsley, Can. J. Phys. 44, 2601 (1966).

Caves, C.M., Phys. Rev. D 26, 1817 (1982).

Celashi, S., T.H. Geballe, and W.P. Lowe, Appl. Phys. Lett. 43, 794 (1983).

Chapman, B., Glow Discharge Processes, Wiley, New York (1980).

Child, C.D., Phys. Rev. 32, 492 (1911).

Cohen, M.H., L.M. Falicov, and J.C. Phillips, Phys. Rev. Lett. 8, 316 (1962).

Cuomo, J.J., J.M.E. Harper, C.R. Guarnieri, D.S. Lee, L.J. Attanasio, J. Angilello, and C.T. Wu, J. Vac. Sci Technol. 20, 349 (1982).

D'Addario, L.R., Int. J. Infrared and Millimeter Waves 5, 1419 (1984).

Dalrymple, B.J., Ph.D. Thesis, Yale University (1983).

Dayem, A.H. and R.J. Martin, Phys. Rev. Lett. 8, 246 (1962).

Deutscher, G. and P.G. de Gennes, in Superconductivity, edited by R.D. Parks, Marcel Decker, New York, (1969).

Devyatov, I.A., L.S. Kuzmin, K.K. Likharev, V.V. Migulin, and A.B. Zorin, J. Appl. Phys. 60, 1808 (1986).

Dolan, G.J., Appl. Phys. Lett. 31, 337 (1977).

Dunkelberger, L.N., J. Vac Sci Technol. 15, 88 (1978).

Durbin, S.M., D.S. Buchanan, and J.E. Cunningham, and D.M. Ginsberg, Phys. Rev. B28, 6277 (1983).

Dynes, R.C., V. Narayanamurti, and J.P. Garno, Phys. Rev. Lett. 41, 1509 (1978).

Dynes, R.C. and J.M. Rowell, Phys. Rev. B11, 1884 (1975).

Ediss, G.A., N.J. Keen, and P. Zimmerman, IEEE Trans. Microwave Theory Tech., MTT-30, 2012 (1982).

Eliashberg, G.M., Soviet Phys. JETP 11, 696 (1960).

Face, D.W., D.E. Prober, W.R. McGrath and P.L. Richards, Appl. Phys. Lett. 48, 1098 (1986).

Faris, S.M., S.I. Raider, W.J. Gallagher, and R.E. Drake, IEEE Trans. Magn. MAG-19, 1293 (1983).

Feinstein, L.G. and D. Huttemann, Thin Solid Films 16, 129 (1973).

Feldman, M.J., presented at the 1986 Applied Superconductivity Conference in Baltimore, Oct. 1986 - to be published in IEEE Trans. Magn. MAG-23, 1987.

Feldman, M.J. and S. Rudner, 1983, in Reviews of Infrared and Millimeter Waves, Vol 1, edited by K.J. Button (Plenum, New York), p. 47.

Feldman, M.J., S.-K. Pan, A.R. Kerr, and A. Davidson, IEEE Trans. Magn. MAG-19, 494 (1983).

Feldman, M.J. ,J. Appl. Phys. 53, 584 (1982).

Fetter, A.L. and J.D. Walecka, Quantum Theory of Many-Particle Systems, McGraw Hill, New York, 1971.

Feuer, M.D., Ph.D. Thesis, Yale (1980).

Gallagher, W.J., S.I. Raider, and R.E. Drake, IEEE Trans. Magn. MAG-19, 807 (1983).

Giaever, I., Phys. Rev. Lett. 5, 147 (1960), and Phys. Rev. Lett. 5, 464 (1960).

Griener, J.H., J. Appl. Phys. 42, 5151 (1971).

Gundlach, K.H., S. Takada, M. Zahn, and H.J. Hartfusse, Appl. Phys. Lett. 41, 294 (1982).

Gurvitch, M. and J. Kwo, in Adv. Cryo. Eng. (A.F. Clark and R.P. Reed, eds.) 30, 509 (1984).

Gurvitch, M., J.M. Rowell, H.A. Huggins, M.A. Washington, and T.A. Fulton, IEDM Digest, 115 (1981).

Halbritter, J., IEEE Trans. Magn. MAG-21, 858 (1985).

Harper, J.M.E., J.J. Cuomo, and H.R. Kaufman, J. Vac. Sci. Technol. 21, 737 (1982).

Harris, R.E., Phys. Rev. B10, 84 (1974).

Hasselberg, L.-E., M.T. Levinsen, and M.R. Samuelsen, Phys. Rev. B9, 3753 (1974).

Heim, G. and E. Kay, J. Appl. Phys. 46, 4006, 1975.

Held, D.N. and A.R. Kerr, IEEE Trans. Microwave Theory and Tech. MTT-26, 49 (1978).

Hicks, R.G., M.J. Feldman, and A.R. Kerr, IEEE Trans. Magn. MAG-21, 208 (1985).

Hieber, K. and N.M. Mayer, Thin Solid Films 90, 43 (1982).

Himpsel, F.J., J.F. Morar, F.R. McFeely, R.A. Pollak, and G. Hollinger, Phys. Rev. B30, 7236 (1984).

Hu, P., R.C. Dynes, V. Narayanamurti, H. Smith, and W.F. Brinkman, Phys. Rev. Lett. 38, 361 (1977).

Huang, H-C.W., S. Basavaiah, C.J. Kircher, E.P. Harris, M. Murakami, S.P. Klepner, and J.H. Griener, IEEE Trans. Electron Dev. ED-27, 1979 (1980).

Huggins, H.A. and M. Gurvitch, J. Vac. Sci. Technol. A1, 77 (1983).

Huggins, H.A. and M. Gurvitch, J. Appl. Phys. 57, 2103 (1985).

Josephson, B.D., Phys. Lett 1, 251 (1962).

Kane, S.M. and K.Y. Ahn, J. Vac. Sci. Technol. 16, 171 (1979).

Kaplan, S.B., C.C. Chi, D.N. Langenberg, J.J. Chang, S. Jafarey, and D.J. Scalapino, Phys. Rev. B14, 4854 (1976).

Kaufman, H.R., J.J. Cuomo, and J.M.E. Harper, J. Vac. Sci. Technol. 21, 725 (1982).

Keith, V. and J.D. Leslie, Phys. Rev. B18, 4739 (1978).

Kerchner, H.R., C.K. Christen, and S.T. Sekula, Phys. Rev. B24, 1200 (1981).

Kerr, A.R., IEEE Trans. Microwave Theory and Tech. MTT-23, 828, (1975).

Kerr, A.R., S.-K. Pan, M.J. Feldman, and A. Davidson, Physica 108B, 1369 (1981).

Klapwijk, T.M., G.E. Blonder, and M. Tinkham, Physica 109+110B, 1157 (1982).

Kleinsasser, A.W., J.M.E. Harper, J.J. Cuomo and M. Heiblum, Thin Solid Films, 333 (1982).

Kleinsasser, A.W., B.D. Hunt, A.C. Callegari, C. Rogers, R. Tiberio, and R.A. Buhrman, IEEE Trans. Magn. MAG-17, 307 (1981).

Kleinsasser, A.W. and R.A. Buhrman, Appl. Phys. Lett. 37, 841 (1980).

Koch, C.C., J.O. Scarbrough, and D.M. Kroeger, Phys. Reb. B9, 888 (1974).

Koch, R.H., D.J. Van Harlingen, and J. Clarke, Phys. Rev. B26, 74 (1982).

Kuan, T.S., S.I. Raider, and R.E. Drake, J. Appl. Phys. 53, 7464 (1982).

Kwo, J., G.K. Wertheim, M. Gurvitch, D.N.E. Buchanan, IEEE Trans. Magn. MAG-19, 795 (1983).

Laegreid, N. and G.K. Wehner, J. Appl. Phys. 32, 365 (1961).

Lahiri, S.K., S. Basavaiah, and C.J. Kircher, Appl. Phys. Lett. 36, 334 (1980).

Markowitz, D. and L.P. Kadanoff, Phys. Rev. 131, 563 (1963).

Matsuo, S, Appl. Phys. Lett. 36, 768 (1980).

McMillan, W.L. and J.M. Rowell, Phys. Rev. Lett. 14, 108 (1965).

McMillan, W.L. and J.M. Rowell, in Superconductivity, R.D. Parks Editor, Marcel Dekker, New York, (1969).

McMillan, W.L. and J.M. Rowell, Phys. Rev. Lett. 14, 108 (1965).

McGrath, W.R., A.V. Raisanen, and P.L. Richards, IEEE Trans. Magn. MAG-21, 212 (1985); and Int. J. Infrared and Millimeter Waves 7, 543 (1986).

McGrath, W.R., Ph.D. Thesis, UC Berkeley (1985).

McGrath, W.R., P.L. Richards, A.D. Smith, H. VanKempen, R.A. Batchelor, D.E. Prober and P.Santhanam, Appl. Phys, Lett. 39, 655 (1981).

McWhan, D.B., M. Gurvitch, J.M. Rowell, and L.R. Walker, J. Appl. Phys. 54, 3886 (1983).

Meservey, R., P.M. Tedrow, and J.S. Brooks, J. Appl. Phys. 53, 1563 (1982).

Metals Handbook, 8th Edition, American Society of Metals, Metals Park, Ohio 44073 (1973).

Moodera, R., R. Meservey, and P.M. Tedrow, Appl. Phys. Lett. 41, 488 (1982).

Moore, C.R. and R.C. Clauss, IEEE Trans. Microwave Theory and Tech. MTT-27, 249 (1979).

Moore, C.R. and D. Neff, IEEE Trans. Microwave Theory and Tech. MTT-30, 2013 (1982).

Morohashi, S., H.Shinya, and T. Yamaoka, Appl. Phys. Lett. 48, 1179 (1985).

Moseley, P.T. and C.J. Seabrook, Acta Cryst. B29, 1170 (1973).

Mukhopadhyay, P., J. Phys. F: Metal Physics 9, 903 (1979).

Murakami, M., H.-C.W. Huang, J. Angilello, and B.L. Gilbert, J. Appl. Phys. 54, 738 (1983).

Neal, W.E.J. and R.M. Aguado Bombin, Thin Solid Films 44, 169 (1977).

Ohtsuka, T., in Anisotropy Effects in Superconductors, H.W. Weber, Editor, Plenum, New York, (1977).

Pei, S.S. and R.B. van Dover, Appl. Phys. Lett. 44, 703 (1984).

Phillips, T.G. and G.J. Dolan, Physica 109 and 110B, 2010, 1982.

Pollak, R.A., H.J. Stolz, S.I.Raider, and R.F. Marks, Oxidation of Metals 20, 185 (1983).

Raider, S.I., IEEE Trans. Magn., MAG-21, 110 (1985).

Rainer, D. and G. Bergmann, J. Low Temp. Phys. 14, 501 (1974).

Raisanen, A.V., W.R. McGrath, D.G. Crete, and P.L. Richards, Int. J. Infrared and Millimeter Waves 6, 1169 (1985).

Reed, T.B., Free Energy of Formation of Binary Compounds, MIT Press, Cambridge, 1971.

Read, M.H. and C. Altman, Appl. Phys. Lett. 7, 51 (1965).

Read, M.H. and D.H. Hensler, Thin Solid Films 10, 123 (1972).

Richards, P.L., IEEE Trans. Magn. MAG-23, (1987) to be published.

Richards, P.L. and T.-M. Shen, IEEE Trans. Electron Devices ED-27, 1909 (1980).

Richards, P.L., T.-M. Shen, R.E. Harris and F.L. Lloyd, Appl. Phys. Lett. 34, 345 (1979).

Rickayzen, G., Green's Functions and Condensed Matter, Academic, New York, 1984.

Rickayzen, G., in Superconductivity Volume 1, R.D. Parks Editor, Marcel Dekker, New York, (1969).

Rochlin, G.I., Phys. Rev. 153, 513 (1967).

Rogers, C.T. and R.A. Buhrman, Phys. Rev. Lett. 55, 859 (1985).

Rogovin, D. and D.J. Scalapino, 1974, Ann. Phys. (N.Y.) 86, 1 (1974).

Rosenberg, D. and G.K. Wehner, J. Appl. Phys. 33, 1842 (1962).

Rosenberg, H.M., Phil. Trans. Roy. Soc. (London) A247, 441-497 (1955).

Rudman, D.A. and M.R. Beasley, Appl. Phys. Lett. 36, 1010 (1980).

Ruggiero, S.T., T.W. Barbee, and M.R. Beasley, Phys. Rev. B26, 4894 (1982).

Ruggiero, S.T., E.K. Track, D.E. Prober, G.B. Arnold and M.J. DeWeert, Phys. Rev. B34, 217 (1986a).

Ruggiero, S.T., S. Schwarzbek, R.E. Howard, and E. Track, Rev. Sci. Instrum. 57, 1444 (1986b).

Saleh, A.A.M., Theory of Resistive Mixers, Res. Monograph 64, Cambridge, MA, MIT Press, 1971.

Samsonov, G.V., Editor, The Oxide Handbook, Plenum, New York, 1982.

Sasaki, K. and T. Umezawa, Thin Solid Films 74, 83 (1980).

Scalapino, D.J., in Superconductivity, R.D. Parks Editor, Marcel Dekker, (1969).

Schmidt, P.H., J. Vac. Sci. Technol. 10, 611 (1973).

Schmidt, P.H., R.N Castellano, and E.G. Spencer, Solid State Technol. 15, 27 (1972).

Schrieffer, J.R. and J.W. Wilkins, Phys Rev. Lett. 10, 17 (1963).

Seki, S., T. Unagami, and B. Tsujiyama, J. Vac. Sci and Technol. A1, 1825 (1983).

Shen, L.Y.L., in Superconductivity in d- and f-Band Metals, edited by D.H. Douglass, Plenum, New York (1972).

Shen, T.-M. and P.L. Richards, IEEE Trans. Magn. MAG-17, 677 (1981).

Shen, T.-M., IEEE J. Quantum Electron. QE-17, 1151 (1981).

Shen, T.-M, P.L. Richards, R.E. Harris, and F.L. Lloyd, Appl. Phys. Lett. 36, 377 (1980).

Shoji, A., M. Aoyagi, S. Kosaka, and F. Shinoki, IEEE Trans. Magn. MAG-23, to be published (1987).

Siegel, P.H. and A.R. Kerr, IEEE Trans. Microwave Theory and Tech. MTT-32, 1579 (1984).

Smith, A.D., W.R. McGrath, P.L. Richards, H. van Kempen, D. Prober and P. Santhanam, Physica B+C 108, 1367 (1981).

Smith, A.D. and P.L. Richards, J. Appl. Phys. 53, 3806 (1982).

Smith, L.N., H. Kroger, and D.W. Jillie, IEEE Trans. Magn. MAG-19, 793 (1983).

Smith, L.N., J.B. Thaxter, E.W. Jillie and H. Kroger, IEEE Trans. Magn. MAG-19, 1571 (1983).

Thomas III, J.H., J. Appl. Phys. 45, 5349 (1974).

Tien, P.K. and J.P. Gordon, Phys. Rev. 129, 647 (1963).

Tinkham, M., Introduction to Superconductivity, McGraw Hill, New York, (1975).

Torrey, H.C. and C.A. Whitmer, Crystal Rectifiers, New York: McGraw Hill, MIT Radiation Laboratory Series vol. 15, 1948.

Tucker, J.R. and M.J. Feldman, Rev. Mod. Phys. 57, 1055 (1985).

Tucker, J.R., Appl. Phys. Lett. 36, 477 (1980).

Tucker, J.R., IEEE J. Quantum Electron. QE-15, 1234 (1979).

van der Pauw, L.G., Phillips Res. Rep. 13, 1 (1958).

Van Duzer, T. and C.W. Turner, Principles of Superconductive Devices and Circuits, Elsevier, New York (1981).

Varma, C., in Superconductivity in d- and f- Band Metals, W. Buckel and W. Weber Ed., Kernforschungszentrum, Karlsruhe GmbH, p. 603 (1982).

Vidberg, H.J. and J.W. Serene, J. Low Temp. Phys. 29, 179 (1977).

Weber, H.W., Editor, Anisotropy Effects in Superconductors, Plenum, New York, (1977).

Weinreb, S., "Noise Parameters of NRAO 1.5 GHz GaAs FET Amplifiers", NRAO Internal Report No. 231, December 1982. Also, D.R. Williams, W. Lum, and S. Weinreb, Microwave Journal, Oct. 1980.

Wengler, M.J. and D.P. Woody, submitted to IEEE J. Quantum Electron. (1986).

Werthamer, N.R., Phys. Rev. 147, 255 (1966).

Westwood, W.D., N. Waterhouse, and P.S. Wilcox, Tantalum Thin Films, Academic, London 1975.

White, G.K., Experimental Techniques in Low Temperature Physics, 3rd Edition, Oxford Press, (1979).

Wilkins, J.W., Tunneling Phenomena in Solids, edited by E. Burnstein and D. Lundquist (Plenum, New York, 1969).

Winkler, D. and T. Claeson, Physica Scripta 32, 317 (1985).

Wisnieff, R.L., Ph.D. Thesis, Yale 1986.

Wolf, E.L., Principles of Electron Tunneling Spectroscopy, Oxford Press, New York, 1985.

Wolf, S.A., J.M. Kennedy, and M Nisenoff, J. Vac. Sci Technol. 13, 145 (1976).

Wu, C.T., Thin Solid Films, 64, 103 (1979)

Yeh, J.T.C. and D.N. Langenberg, Phys Rev. B17, 4303 (1978).

Zorin, A.B., IEEE Trans. Magn. MAG-21, 939 (1985).